SiGe Receiver Front Ends and Flip-Chip Integrated Wideband Antennas for Millimeter-Wave Passive Imaging

by

Johnna Dawn Powell

Submitted to the Department of Electrical Engineering and Computer Science
in partial fulfillment of the requirements for the degree of

Doctor of Philosophy in Electrical Engineering and Computer Science

at the

MASSACHUSETTS INSTITUTE OF TECHNOLOGY

February 2009

Author .....
Department of Electrical Engineering and Computer Science
January 22, 2009

Certified by .....
Charles G. Sodini
LeBel Professor of Electrical Engineering
Thesis Supervisor

Accepted by .....
Terry P. Orlando
Chairman, Department Committee on Graduate Students

SiGe Receiver Front Ends and Flip-Chip Integrated Wideband Antennas for Millimeter-Wave Passive Imaging

by

Johnna Dawn Powell

Submitted to the Department of Electrical Engineering and Computer Science
on January 22, 2009, in partial fulfillment of the
requirements for the degree of
Doctor of Philosophy in Electrical Engineering and Computer Science

Abstract

SiGe wideband 77-GHz and 94-GHz front end receivers with integrated antennas for passive imaging have been designed and characterized. These front end systems exhibit wideband performance with the highest gain and lowest noise figures reported thus far for silicon-based systems in the 77-GHz and 94-GHz frequency regimes, to the best of the author's knowledge. These systems each comprise a fully differential integrated antenna, LNA, and a double-balanced mixer. A separate 77-GHz front end also features an on-chip 72-GHz cross-coupled VCO. The 77-GHz front end receiver achieves 46 dB max conversion gain, 6.5-10 dB noise figure (NF), output-referred 1dB compression point of +2 dBm and DC power dissipation (P_{DC}) of 122 mW. The 94-GHz receiver achieves 47 dB max conversion gain, 7-12.5 dB NF, and P_{DC} of 120 mW. The antenna performance yields gains of 10-13 dB over 70-100 GHz, with greater than 90% efficiency. The integrated antenna exhibits a typical loss of 0.5-1 dB, or 80-90% efficiency, and a worst-case radiation loss of $\approx$ -2 dB (efficiency = 63%). These reported results exceed published on-chip antenna performance, which typically achieve $<$ 10% efficiency. Antenna loss degrades receiver noise figure and gain, yielding a less viable receiver. The individual design, co-design and integration of each element making up the RF front end collectively contribute to the overall high performance of these front end receivers.

The 77-GHz LNA achieves 4.9-6.0 dB NF, 18-26 dB gain, and S11, S22 of -13.0 and -12.8 dB, respectively. The mixer achieves 12-14 dB NF, 20-26 dB conversion gain and -26dBm IP1dB (input-referred). The VCO achieves output power from -2 to 0 dBm with phase noise of -93 dBc/Hz at 72 GHz. The 94-GHz LNA achieves 22-dB max gain, 7.0 dB NF, -25 dB and -10 dB S11 and S22, respectively. This LNA also exhibits very wideband performance, achieving >10 dB gain from 40-100 GHz.

Thesis Supervisor: Charles G. Sodini
Title: LeBel Professor of Electrical Engineering

Acknowledgments

Without the love and support of family, friends and colleagues, a Ph.D. thesis is near impossible.

First and foremost, I'd like to thank my Ph.D. advisor, Charlie Sodini, for his advice, encouragement and support, and for the opportunity to work on this project. I'd also like to thank Helen Kim for her support and encouragement, and for providing valuable collaborative input, advice, and access to state-of-the-art test facilities. I'd also like to thank Joel Dawson and David Staelin for explicating my thesis and contributing to its overall improvement and clarity.

I'd also like to thank the past and present members of the Sodini-Lee group for their help, support and wonderful company, including Mariana Markova, Khoa Nguyen, Ke Lu, Jack Chu, Anthony Accardi, Ivan Nausieda, Albert Chow, Mark Spaeth, Kevin Ryu, David He, John Fiorenza, Farinaz Edelat, and Jit Ken Tan and Suzanne Piccarini.

Several of the members of the MTL and Lincoln Lab staff went above and beyond the call of duty in order to help me, including Kurt Broderick, Dennis Ward, Bob Devine, Karen Parrillo, Richard Slattery, Rick Drangmeister and Peter Murphy. A sincere thank you to all.

Amazing friends are some of life's most precious gifts. I have been fortunate and blessed to have been surrounded by some of the most wonderful people in the world. Words cannot describe my gratitude to these amazing people in my life for all they have done and all they have been: Lucie Fisher, Ali Motamedi, Mariana Markova, Ahmad Minkara, Dee Symonds, Tanguy Chau, Vasileios Dendroulakis, Lynne Waldman, Jay Fucetola, Corrie Hulten, Corey Fucetola, Sa'ed Atshan, Chip Vaughan, Tufool Al-Nuaimi, Shawn Staker and Susan Brown.

Most importantly, thank you to my family, which has provided me with unconditional love and support throughout my entire life: My mom, dad, my sister, and also Dan and Betty. I cannot express how much it means to have had them throughout my life.

Contents

1 Introduction **15**

1.1 Motivation 16

1.2 Challenges 17

1.3 Related Work 18

2 SiGe Front End Integrated Receivers **19**

2.1 System Design 20

2.2 77-GHz Front End 22

2.2.1 Overview: Highlights and Chip Layout 22

2.2.2 Characterization 24

2.3 94-GHz Front End 32

2.3.1 Characterization 33

2.4 Antenna Flip-Chip Packaging and Test 35

3 Wideband Millimeter-Wave Antenna **46**

3.1 Fundamental Antenna Characteristics 47

3.1.1 Impedance Bandwidth 47

3.1.2 Radiation Pattern 49

3.1.3 Half-Power Beamwidth 52

3.1.4 Directivity 54

3.1.5 Efficiency 56

3.1.6 Gain 56

3.2 Considerations for Millimeter-Wave Antenna Design 57

3.2.1 Silicon Losses . . . 57
3.2.2 On-Chip vs. Off-Chip Antennas . . . 59
3.3 Antenna Simulation and Design . . . 61
3.3.1 Design . . . 64
3.3.2 Simulation . . . 67
3.4 Antenna Fabrication . . . 67
3.4.1 Chrome Mask . . . 70
3.4.2 Copper Processing . . . 71
3.4.3 Wet Etch . . . 74
3.4.4 Sputtering . . . 76
3.4.5 Copper Polishing . . . 79
3.5 Antenna Testing and Characterization . . . 81
3.6 Antenna Results . . . 85

4 Differential Low Noise Amplifier. 95
4.0.1 Noise Factor Derivation . . . 96
4.1 Design . . . 97
4.1.1 LNA Topology . . . 97
4.1.2 Design for Simultaneous Minimum NF and Impedance Match 101
4.1.3 Output Match . . . 108
4.2 Measured Results . . . 108
4.3 94 GHz LNA . . . 114
4.4 LNA Summary and Conclusions . . . 115

5 Double-Balanced Mixer 116
5.1 Fundamental Mixer Characteristics . . . 116
5.2 Mixer Topologies . . . 118
5.3 77-GHz Double-Balanced Downconversion Mixer . . . 120
5.3.1 Design . . . 120
5.3.2 Measured Results . . . 123
5.4 Mixer Summary and Conclusions . . . 126

6 Cross-Coupled Voltage-Controlled Oscillator **128**

6.1 VCO Fundamental Theory 129

6.1.1 Negative Resistance and Positive Feedback 129

6.1.2 Phase Noise 134

6.1.3 LO Phase Noise and its effect on Receiver Performance 137

6.2 Design and Characterization 138

6.2.1 Topology- VCO Core 138

6.2.2 Topology- VCO Buffers 144

6.2.3 Layout 144

6.2.4 Testing Methodology 145

6.3 VCO Summary and Conclusions 147

7 Conclusions **153**

7.1 Overall Impact 153

7.2 Thesis Summary 153

7.3 Future Work 156

A **159**

A.1 Antenna Gain vs. Angle: Azimuth Plane 159

B **165**

B.1 Antenna Gain vs. Angle: Elevation Plane 165

C **171**

C.1 Antenna Gain vs. Frequency 171

List of Figures

1-1 *Millimeter-Wave Applications.* 16

1-2 *Electromagnetic Wave Spectrum. Courtesy Isaiah Blankson [1].* . . . 17

2-1 *System Block Diagram.* 22

2-2 *77-GHz Front End Passive Imager, on-chip LO.* 23

2-3 *77-GHz Front End Passive Imager, off-chip LO.* 23

2-4 *77-GHz Front End Passive Imager Conversion Gain Measurement, on-chip LO.* 24

2-5 *77-GHz Front End Passive Imager, Conversion Gain and NF Measurement vs. Simulation, off-chip LO.* 25

2-6 *77-GHz Front End Passive Imager IP1dB, off-chip LO.* 25

2-7 *77-GHz Simulated/Measured Conversion gain and Noise Figure for On-Chip and Off-chip LO.* 27

2-8 *77-GHz Conversion Gain Comparison: Introducing impedance mismatch between the LNA and Mixer ports results in /approx10-dB loss in gain.* 28

2-9 *77-GHz Front End Noise Figure Measurement.* 28

2-10 *Coupled-wire Chebychev Filter design with Ansoft Designer SV.* . . . 29

2-11 *Image-Reject Filter Inserted between LNA and Mixer.* 30

2-12 *NF simulated results indicating NF improvement with Chebychev Bandpass Image-Reject Filters.* 30

2-13 *Noise Figure measurement.* 32

2-14 *94-GHz Chip Photo.* 33

2-15 *94 GHz Front End Conversion Gain and Noise Figure (Simulated vs. Measured).* 34
2-16 *Coining process enables smooth, consistent surface. Right: Original Solder Bump. Left: Coined Solder Bump.* 35
2-17 *Illustration of Gold Stud Bumps enabling flip-chip bonding with silver epoxy.* 36
2-18 *Close-up Chip Photo with Antenna securely connected via gold solder bumps.* 37
2-19 *Chip Photo with Antenna securely connected via gold solder bumps.* . 37
2-20 *LNA Measured Gain.* 39
2-21 *Measured Integrated Antenna Gain and Unpackaged Antenna Gain vs. Frequency for 91-99 GHz.* 42
2-22 *Measured Integrated Antenna Gain and Unpackaged Antenna Gain vs. Frequency for 73-81 GHz.* 44

3-1 *Transmission Line Model.* 47
3-2 *Dipole Radiation Model, simulated in CST Microwave Studio.* 51
3-3 *Two-Dimensional Radiation Pattern for half-wave dipole: Varying θ, $\phi = 0°$ (left) and varying $\phi, \theta = 0°$ (right)* 51
3-4 *CST Microwave Studio model of horn antenna and simulated 3D radiation pattern* 53
3-5 *CST Microwave Studio simulated radiation pattern. Varying θ, $\phi = 0°$ (left). Varying $\phi, \theta = 0°$ (right)* 53
3-6 *Radiation Quality Factor and Copper Loss Quality Factor vs. Antenna Height from Substrate.* 62
3-7 *Theoretical antenna loss vs. height (h/lambda) from ground plane.* . . 63
3-8 *Truncation of Antenna Ellipses at y-radius.* 65
3-9 *Truncation of Antenna Ellipses at x-radius* 65
3-10 *Addition of curvature for smoother radiation pattern.* 66
3-11 *Antenna Simulated S11* 68

3-12 *Simulated 3D radiation pattern at 90 GHz.* 68
3-13 *Simulated 3D radiation pattern at 100 GHz.* 69
3-14 *Orientation of the antenna as it achieves the simulated 3-dimensional radiation patterns illustrated in Figures 3-12 and 3-13.* 69
3-15 *Chrome Mask Fabricated on MIT's Heidelburg Tool.* 71
3-16 *Copper Disc on Photoresist Coater.* 72
3-17 *Copper Disc Spinning on Photoresist Coater.* 72
3-18 *Copper Disc Pre-Exposure Bake.* 73
3-19 *MJB3 Broadband Exposer.* 74
3-20 *Copper Disc After Broadband Exposure and Photoresist Development.* 75
3-21 *Antenna post-wet etch with 1/2 oz. copper deposit RO4350B material, illustrating significant undercut from etch.* 76
3-22 *EML Sputter Tool* 77
3-23 *Copper Target for Sputter Tool* 77
3-24 *EML Sputter Tool with Dielectric Discs* 78
3-25 *Copper Discs Post Sputter* 78
3-26 *Antenna after processing with Cu sputter-deposited material.* 79
3-27 *Highly magnified antenna illustrating photoresist layer still intact after wet etch.* 80
3-28 *Final copper antenna with photoresist removed.* 80
3-29 *WinCal calculation of VNA calibration error.* 82
3-30 *Conceptual antenna gain test setup.* 83
3-31 *Antenna Orientation for Azimuth plane measurement* 84
3-32 *Antenna Orientation for Elevation plane measurement* 84
3-33 *Antenna Simulated S11 vs. Measured S11* 86
3-34 *Antenna Simulated Gain vs. Normalized Measured Gain. Frequency = 91 GHz, varying angle Θ (Elevation plane).* 87
3-35 *Antenna Simulated Gain vs. Normalized Measured Gain. Frequency = 91 GHz, varying angle Φ (Azimuth plane).* 88

3-36 *Antenna Simulated Gain vs. Measured Gain. Frequency = 100 GHz, varying angle Θ (Elevation plane).* 88
3-37 *Antenna Simulated Gain vs. Measured Gain. Frequency = 100 GHz, varying angle Φ (Azimuth plane).* 89
3-38 *Measured Antenna Gain vs. Angle: 73 GHz and 75 GHz, Azimuth Plane.* 89
3-39 *Measured Antenna Gain vs. Angle: 80 GHz and 81 GHz, Azimuth Plane.* 90
3-40 *Measured Antenna Gain vs. Angle: 93 GHz and 94 GHz, Azimuth Plane.* 90
3-41 *Measured Antenna Gain vs. Angle: 100 GHz and 105 GHz, Azimuth Plane.* 91
3-42 *Measured Antenna Gain vs. Angle: 73 GHz and 75 GHz, Elevation Plane.* 91
3-43 *Measured Antenna Gain vs. Angle: 80 GHz and 81 GHz, Elevation Plane.* 92
3-44 *Measured Antenna Gain vs. Angle: 93 GHz and 94 GHz, Elevation Plane.* 92
3-45 *Measured Antenna Gain vs. Angle: 100 GHz and 105 GHz, Elevation Plane.* 93
3-46 *Measured Antenna Gain vs. Frequency: Azimuth Plane.* 93
3-47 *Measured Antenna Gain vs. Frequency: Elevation Plane.* 94

4-1 *Noise Figure calculation for cascaded stages.* 97
4-2 *Simple BJT Cascode Schematic.* 98
4-3 *Simplified Small Signal Equivalent Circuit Model for BJT Cascode.* . 98
4-4 *2-Stage Cascode LNA Schematic.* 100
4-5 *2-Port Network for Short Circuit Current Analysis.* 101
4-6 *Common Emitter Transistor with Emitter Degeneration.* 104
4-7 *Noise-Free Y Parameters block. The connection between Base-Emitter represents Port 1, and the connection between Collector-Emitter represents Port 2.* 106
4-8 *2nd Stage of LNA for Output Load Approximation.* 109

4-9 *Approximation of Equivalent Circuit Looking into Collector of the Cascode Transistor.* 109
4-10 *Transmission Line Matching Network (Shunt Stub and Series Transmission Lines).* 110
4-11 *Smith Chart Sweep of Transmission Line Lengths for Optimal Load Impedance Matching.* 110
4-12 *LNA Simulated vs. Measured Results.* 111
4-13 *Illustration of Inductive Parasitic Path Occuring at the Output Stage of the LNA* 112
4-14 *Simulated vs. Measured Results with Parasitic Inductance* 113
4-15 *LNA 91-99 GHz Simulated vs. Measured Results.* 114

5-1 *Single-Balanced Mixer Topology.* 119
5-2 *Double-Balanced Mixer Topology.* 120
5-3 *Common-base configuration.* 121
5-4 *Common-emitter configuration.* 121
5-5 *Double-Balanced Mixer Schematic.* 122
5-6 *77-GHz Mixer Simulated vs. Measured Noise Figure and Conversion Gain.* 124
5-7 *77-GHz Mixer Simulated vs. Measured Input-Referred 1-dB Compression Point.* 125
5-8 *77-GHz Mixer Die Photo.* 127

6-1 *LC Resonator Tank.* 130
6-2 *BJT Cross-Coupled Pair with Frequency-Selective LC Tank.* 131
6-3 *Illustration of $-g_m$ resistance model for active BJT device. [2]* 132
6-4 *Simplified BJT Cross-Coupled Pi Model for calculating input resistance.* 133
6-5 *VCO Core Design Schematic.* 139
6-6 *VCO Core S-parameter response without Capacitive Feedback.* 141
6-7 *VCO Core S-parameter response with Capacitive Feedback.* 141
6-8 *VCO Full Schematic.* 143

6-9 *VCO Core Layout, illustrating the feedback capacitors and symmetry.* 145
6-10 *VCO Breakout Layout.* 146
6-11 *VCO Phase Noise Measurement at 70.1 GHz.* 149
6-12 *VCO Phase Noise Measurement at 75 GHz.* 150
6-13 *VCO Die Photo.* 151

7-1 *State-of-the-Art Graphical Comparison: Noise Figure vs. Gain.* 156

A-1 *Antenna Gain vs. Angle: 70 GHz and 72 GHz, Azimuth Plane.* . . . 159
A-2 *Antenna Gain vs. Angle: 73 GHz and 75 GHz, Azimuth Plane.* . . . 160
A-3 *Antenna Gain vs. Angle: 77 GHz and 79 GHz, Azimuth Plane.* . . . 160
A-4 *Antenna Gain vs. Angle: 80 GHz and 81 GHz, Azimuth Plane.* . . . 161
A-5 *Antenna Gain vs. Angle: 83 GHz and 85 GHz, Azimuth Plane.* . . . 161
A-6 *Antenna Gain vs. Angle: 87 GHz and 89 GHz, Azimuth Plane.* . . . 162
A-7 *Antenna Gain vs. Angle: 90 GHz and 91 GHz, Azimuth Plane.* . . . 162
A-8 *Antenna Gain vs. Angle: 93 GHz and 94 GHz, Azimuth Plane.* . . . 163
A-9 *Antenna Gain vs. Angle: 95 GHz and 97 GHz, Azimuth Plane.* . . . 163
A-10 *Antenna Gain vs. Angle: 98 GHz and 99 GHz, Azimuth Plane.* . . . 164
A-11 *Antenna Gain vs. Angle: 100 GHz and 105 GHz, Azimuth Plane.* . . 164

B-1 *Antenna Gain vs. Angle: 70 GHz and 72 GHz, Elevation Plane.* . . . 165
B-2 *Antenna Gain vs. Angle: 73 GHz and 75 GHz, Elevation Plane.* . . . 166
B-3 *Antenna Gain vs. Angle: 77 GHz and 79 GHz, Elevation Plane.* . . . 166
B-4 *Antenna Gain vs. Angle: 80 GHz and 81 GHz, Elevation Plane.* . . . 167
B-5 *Antenna Gain vs. Angle: 83 GHz and 85 GHz, Elevation Plane.* . . . 167
B-6 *Antenna Gain vs. Angle: 87 GHz and 89 GHz, Elevation Plane.* . . . 168
B-7 *Antenna Gain vs. Angle: 90 GHz and 91 GHz, Elevation Plane.* . . . 168
B-8 *Antenna Gain vs. Angle: 93 GHz and 94 GHz, Elevation Plane.* . . . 169
B-9 *Antenna Gain vs. Angle: 95 GHz and 97 GHz, Elevation Plane.* . . . 169
B-10 *Antenna Gain vs. Angle: 98 GHz and 99 GHz, Elevation Plane.* . . . 170
B-11 *Antenna Gain vs. Angle: 100 GHz and 105 GHz, Elevation Plane.* . . 170

C-1 *Antenna Gain vs. Frequency: Azimuth Plane.* 171
C-2 *Antenna Gain vs. Frequency: Azimuth 21 Degrees.* 172
C-3 *Antenna Gain vs. Frequency: Azimuth 55 degrees.* 172
C-4 *Antenna Gain vs. Frequency: Azimuth 65 degrees.* 173
C-5 *Antenna Gain vs. Frequency: Azimuth 90 degrees.* 173
C-6 *Antenna Gain vs. Frequency: Elevation Plane.* 174
C-7 *Antenna Gain vs. Frequency: Elevation 45 degrees.* 174
C-8 *Antenna Gain vs. Frequency: Elevation 60 degrees.* 175
C-9 *Antenna Gain vs. Frequency: Elevation 80 degrees.* 175
C-10 *Antenna Gain vs. Frequency: Elevation 90 degrees.* 176

List of Tables

2.1 Measured Loss & Gain Parameters in Integrated Antenna Characterization 91-99 GHz 41

2.2 Measured Loss & Gain Parameters in Integrated Antenna Characterization: 73-81 GHz 45

4.1 LNA Performance Parameters Table 115

5.1 Mixer Performance Parameters Summary 126

6.1 VCO Performance Parameters Table 152

7.1 State-of-The-Art Comparisons of Silicon-Based Receivers and/or Receiver Components 155

Chapter 1

Introduction

The area of millimeter-wave (MMW) systems research and design has become increasingly popular in recent years with the advancement of processes which enable quality performance of silicon-based systems. Several exciting applications exist for MMW design, including wireless communications at 60-GHz, collision-avoidance radar at 77-GHz, improvement of navigational aids and air safety in poor visibility conditions at 94-GHz, concealed weapons detection and imaging at 77-GHz, 94-GHz and higher. Figure 1-1 illustrates some of these challenging opportunities. This thesis focuses primarily on the application of passive imaging for concealed weapons detection, which requires very high gain, wide bandwidth and low noise. However, the systems presented in this thesis can extend to several existing applications.

Concealed weapons have become an increasing threat requiring advances in detection. They can be detected via passive or active imaging given that they are composed of materials that possess contrasting emissivity and reflectivity properties than those of the human body. In this thesis, complete integrated passive imager front ends in the frequency ranges from 73-81 and 91-99 GHz are presented, including packaged flip-chip bonded antennas. Compared with current published work, these systems are high gain, wideband front end receivers that are fully differential, achieving comparably low noise. Most notable about this work, however, is the holistic system design aspect, in that the LNA was co-designed for the packaged antenna, to minimize losses and to optimize receiver performance.

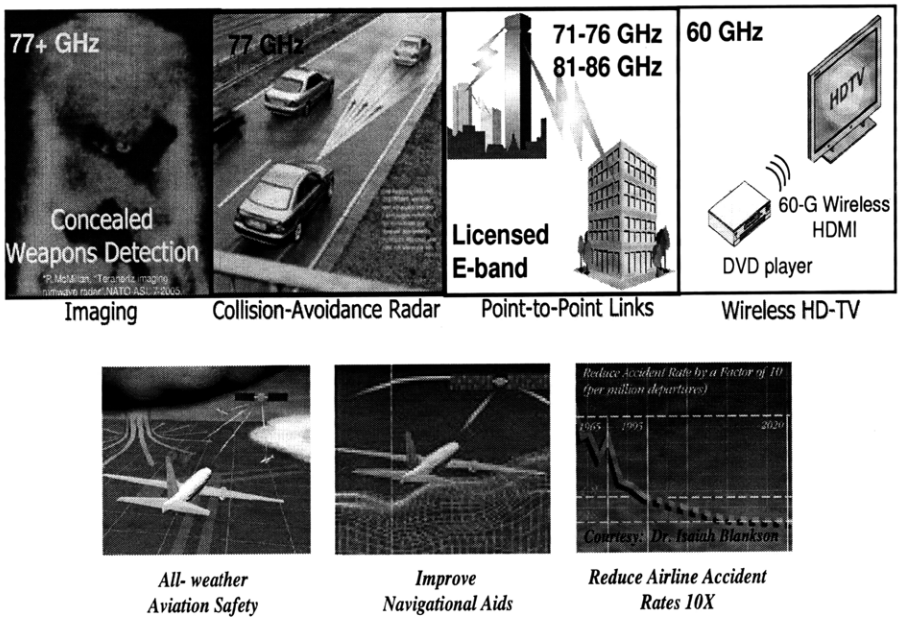

Figure 1-1: *Millimeter-Wave Applications.*

1.1 Motivation

An overview of the electromagnetic spectrum, from AC and radio-frequencies through the visible part of the spectrum and Gamma rays, is shown in Figure 1-2 [1]. Millimeter-waves have several advantages over microwaves, a regime in which a great deal of remote sensing and passive imaging has been done. Given the small wavelength of the millimeter-wave frequency regime, high spatial resolution can be achieved, as well as very small antenna and overall package size. Broad IF bandwidths can be achieved, as well. While 8 GHz represents a very broad IF bandwidth, it only represents a fraction ($\approx$ 10%) of 77-GHz. Thus, it is easier to achieve broad bandwidth at MMW frequencies. Also, MMW systems have low probability of interference, as there are very few systems currently in use at this regime. Another key advantage of millimeter-wave radiation is its ability to penetrate clouds, dust, snow, fog and other various weather impediments with lower attenuation than infrared (as shown in Figure 1-2). This certainly gives millimeter-wave system a significant advantage over infrared and optical wavelengths for passive imaging in adverse weather conditions.

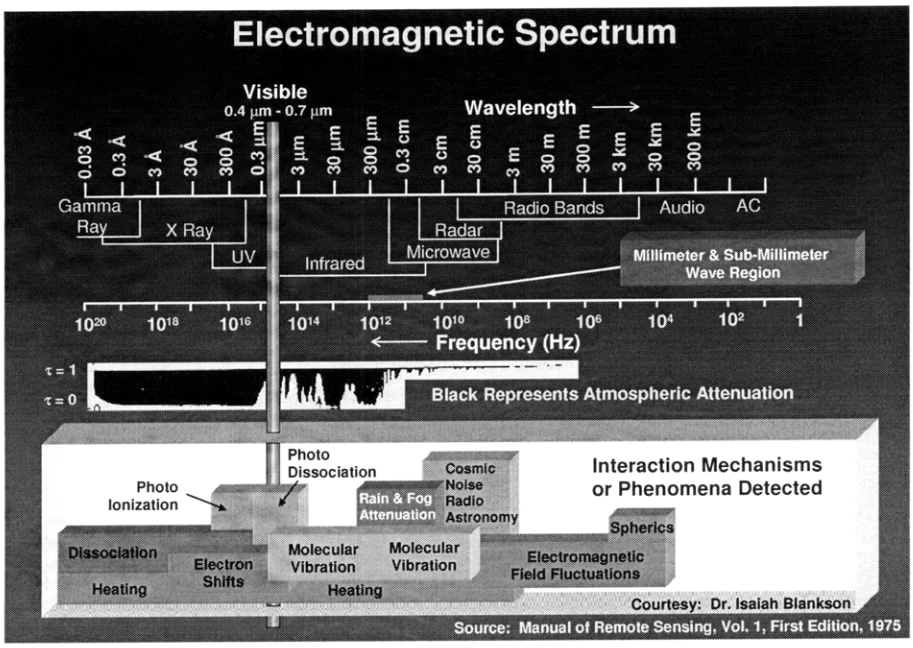

Figure 1-2: *Electromagnetic Wave Spectrum. Courtesy Isaiah Blankson [1].*

1.2 Challenges

Several unique challenges exist when designing, characterizing and troubleshooting in the millimeter-wave regime. In system and circuit design, these challenges include understanding and overcoming discrepancies between simulated and measured results, carefully monitoring critical nodes in parasitic extractions, and relating these discrepancies in a reasonable manner. Often models used in simulation do not behave as ideally expected in practical measurements for several reasons, including limitations in the test equipment, incorrectly modeled parameters, and overestimation or underestimation of extracted parasitic values.

Testing in this regime requires significant experience to troubleshoot, as well as expensive equipment which needs to be consistently checked for proper performance. Perhaps the most important aspect of testing is ensuring that the chip is thoroughly designed for test, thereby providing a means for adjustment and probing of every external parameter possible.

Another key challenge is the fact that silicon-based millimeter-wave design and

reported measurements is still a relatively new arena, leaving a dearth of literature to reference and learn from. Therefore, perhaps the most valuable lessons gained by researching in this area come from practical experience in design and testing. All in all, however, these challenges culminate together to present key opportunities for gaining exceptional insight and expertise in this area.

1.3 Related Work

A great deal of work has been done in passive imaging using III-V technology (such as GaAs/InP HEMT devices), as well as in discrete systems [3–6]. These systems do tend to exhibit better noise performance than silicon-based systems, and for certain applications, they are preferred. However, these technologies also tend to have significantly higher cost than silicon processes. In addition, steady increases in the SiGe HBT cutoff frequencies (f_Ts) have demonstrated equivalent or better performance than their III-V counterpart [7]. SiGe also can withstand high current densities without sustaining lattice damage, thereby exhibiting the advantage of high thermal conductivity. These advantages are not characteristic of III-V compounds. Furthermore, SiGe BiCMOS also features advanced passive elements, which enable highly integrated and complex SoCs. Significant advances have been made recently in these areas using SiGe technology [8–11].

This thesis will first detail the holistic system design with antenna integration for two receiver systems at 77 GHz and 94 GHz. This will include full characterization of flip-chip integrated antennas, detailing the loss incurred at the receiver front end terminals due to the antenna interconnect. This discussion can be found in Chapter 2. The following chapters will detail the design of the individual elements which make up each front end receiver, including the wideband MMW antenna (Chapter 3), the fully differential LNA (Chapter 4), the double-balanced mixer (Chapter 5), and the cross-coupled VCO (Chapter 6). Conclusions and future work can be found in Chapter 7.

Chapter 2

SiGe Front End Integrated Receivers

This section will detail the design and characterization of the wideband 77-GHz and 94-GHz SiGe front end integrated receivers. The 77-GHz passive imager front end comprised an integrated wideband antenna, a fully differential two-stage Low Noise Amplifier (LNA), a double-balanced Gilbert-Cell mixer, and both an off-chip (external) LO and an on-chip LO signal from a fully differential VCO, which will ultimately be an integral part of a full PLL. The 94-GHz passive imager front end comprised the same elements as the 77-GHz system, re-tuned for optimal operation at 94-GHz and with an external LO input. These front end receivers with integrated antennas both comprise, to the author's knowledge, the highest gain and widest bandwidth silicon-based imagers reported at these frequencies. This is achieved by ensuring that each individual element provovides simultaneously minimum noise and high gain, while also making careful considerations in the integration details. Finally, most notable about this work is the co-design and flip-chip assembly of integrated wideband antennas that achieve excellent radiation efficiency, bandwidth and gain. Much work has been done in the area of on-chip antennas, [12–23], but in these designs, much radiation is lost in the substrate, yielding poor efficiency and antenna gain. The majority of research will yield the conclusion that even the worst integrated antenna performs better than the best on-chip antenna.

Some progress has been made in the area of above-chip antenna design, including simulation and design results in [24], which features simulated antenna gains of 1.5 dBi. Also, exceptional work has been done by IBM [25], which reports an external folded dipole antenna with an effective 5 dB of gain (after receiver interconnect losses are considered). Clearly these results are far superior to the lossy on-chip antenna performances reported, which directly reduce the gain and degrade the noise figure of the receivers due to their poor efficiencies on the order of $< 10\%$.

Each individual component making up the SiGe front ends in this thesis will be detailed in the following chapters. This chapter will focus on the holistic approach of the system design, integration and layout, including the integration of the antenna.

2.1 System Design

The system block diagram for the passive imager is shown in Figure 2-1. This thesis focuses on the key features of the RF Front End, namely the Antenna, LNA, Mixer, VCO, and also the full integrated system. The Millimeter-Wave Ultra-Wideband antenna optimally senses radiation within the RF range of 70-100 GHz, such that one antenna can be used for both frequency bands. Passive millimeter-wave radiation for this system is expected to have power levels of approximately -60 dBm. The detector, located at the output of the IF amplifier, requires approximately -10 dBm of signal power for optimal operation. Therefore, the RF front end should ideally provide 50 dB of low-noise gain.

The estimated required receiver sensitivity is $\approx$ 1- 1.5K. This is based on an assumption of 13dB SNR required to discern 20K thermal contrast. [11] The temperature resolution is a performance indicator of a passive imager. ΔT is the minimum detectable change in the imager temperature. It can be estimated by Equation 2.1:

$$\Delta T \approx (T_A + T_N) * \sqrt{\frac{1}{BW\zeta}} \tag{2.1}$$

where T_A is the background temperature, which encompasses the cold sky to the warmer ground. T_A is assumed to be 290K, for simplicity, and assuming the worst-

case scenario. T_N is the receiver noise temperature. T_N is estimated to be ≈1540K for a receiver with 8 dB noise figure. ζ indicates the integration time, which is assumed to be 10ms. This is determined by the frame rate of 10Hz needed to detect a person walking with a factor of 10 margin and also above the 1/f noise frequency. BW indicates the frequency bandwidth of 8GHz. For an ideal imager, ΔT can be as low as 0.27K for the current design. However, sometimes gain fluctation presents a problem in imaging systems. A primary source of gain fluctuation of MMW receivers implemented in III-V technology is 1/f noise. SiGe bipolar device exhibits a lower 1/f corner frequency than GaAs and InP devices [11, 26, 27]. Therefore, the gain fluctuation might present less of a problem for SiGe bipolar circuits. Including the effect of a gain fluctuation, Equation 2.1 can be modified to

$$\Delta T \approx (T_A + T_N) * \sqrt{\frac{1}{BW\zeta} + \left(\frac{\Delta G}{G}\right)^2} \tag{2.2}$$

If ΔG/G is allowed to be $1.88x10^{-}4$, ΔT can increase to 0.4K. It can be inferred from this analysis that a contrast of 8K is feasible if the temperature resolution is 0.4K. This also assumes 13dB of SNR provides a reasonable image. The gain fluctuation can be further mitigated by selecting a shorter integration time than the 1/f corner frequency, and also by selecting an AC coupling frequency above the 1/f corner frequency. For further information on this concept, see references [11]- [28].

The front-end design is a superheterodyne configuration, whereby an incoming millimeter-wave RF signal is downconverted by a local oscillator (LO) signal to an intermediate (operable) frequency range that can be more easily amplified and processed. References [2] and [29] have excellent explanations for these receiver systems, and they also provide a full historical perspective on the origins and motivation for superheterodyne systems in early radio design.

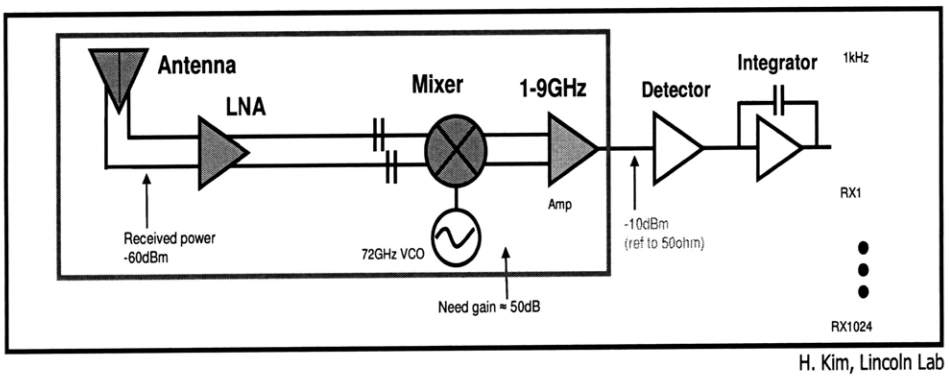

Figure 2-1: *System Block Diagram.*

2.2 77-GHz Front End

2.2.1 Overview: Highlights and Chip Layout

The LNA, VCO and Mixer (which are discussed in full detail in later chapters) were integrated together as part of the 77-GHz passive imager front end with an on-chip LO, as shown in Figure 2-2. Each individual block is highlighted and labelled. The 77-GHz LNA achieved 4.9-6.0 dB NF, 18-26 dB gain, input return loss (S11) of -13.0 dB, and output return loss (S22) of -12.8 dB. The Double-Balanced Mixer achieved 12-14 dB NF, 20-26 dB conversion gain and -26dBm P1dB (input-referred). The VCO achieved output power from -2 to 0 dBm with phase noise of ≈-93 dBc/Hz at 1 MHz offset, at approximately 72 GHz. The alternate version of the front end receiver is shown in Figure 2-3. This configuration incorporated a balun in place of the VCO in order to enable single-ended off-chip LO input. The single-ended input was then converted to a differential signal for the mixer input terminals. The LO signal was purposely placed at the farthest end possible from the RF input and IF output in the layout so as to limit LO feedthrough at the IF through the substrate. Also, the VCO was simulated, laid out and tested with its differential output lines at the exact length required by the Mixer input LO terminals.

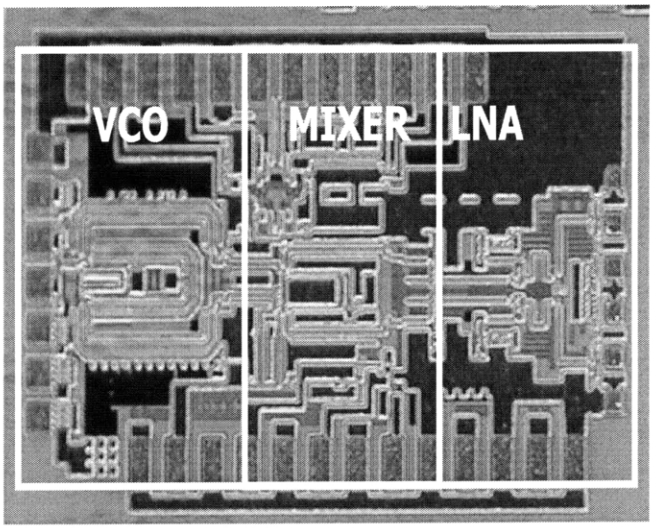

Figure 2-2: *77-GHz Front End Passive Imager, on-chip LO.*

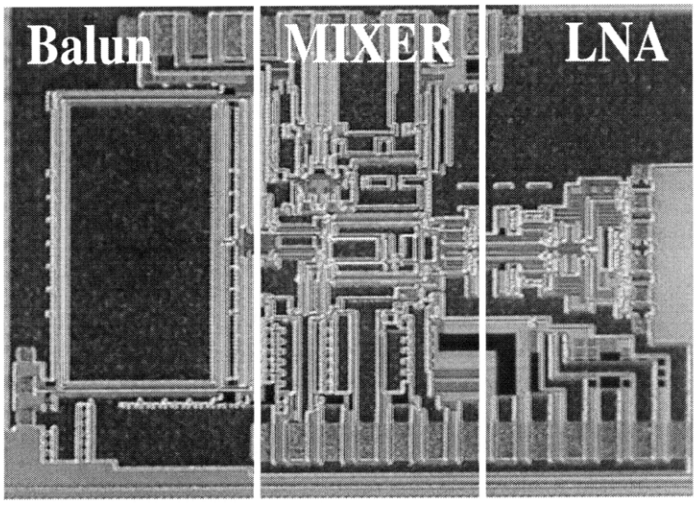

Figure 2-3: *77-GHz Front End Passive Imager, off-chip LO.*

2.2.2 Characterization

Chip Results

The LNA/Mixer system was first measured with an external (or off-chip) LO in order to determine the conversion gain, NF and IP1dB for an "ideal" LO source, provided by a signal generator and external source module. This chip, photographed in Figure 2-3, incorporated an on-chip balun to provide a fully differential LO signal to the mixer. In this case, the LO frequency was held at 75 GHz (this was the minimum cut-off frequency of the source module), 0 dBm power, and the RF signal was swept from 73-81 GHz. Figure 2-5 illustrates the simulated and measured conversion gain and noise figure for the LNA/Mixer with RF frequency sweep at -60 dBm input power. Also illustrated in Figure 2-4 is the measured conversion gain for the on-chip LO. In this case, the VCO operated at approximately 72 GHz. Figure 2-6 illustrates the P1dB measurement.

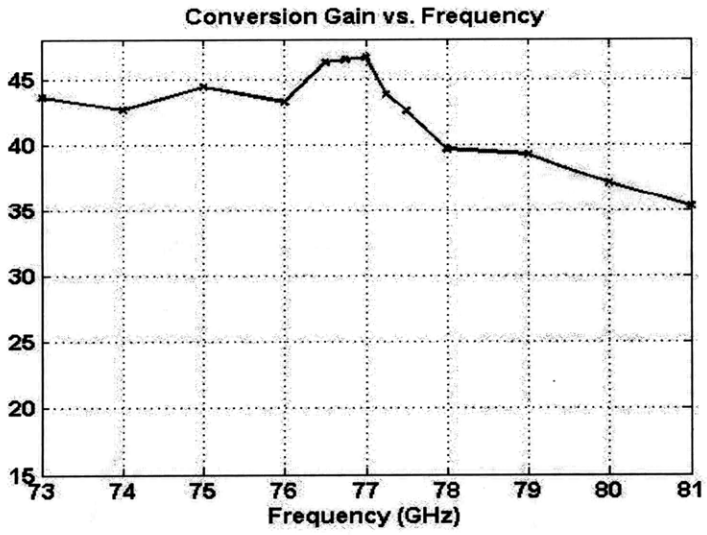

Figure 2-4: *77-GHz Front End Passive Imager Conversion Gain Measurement, on-chip LO.*

The trend seen in the mixer conversion gain (see Mixer chapter) and the receiver

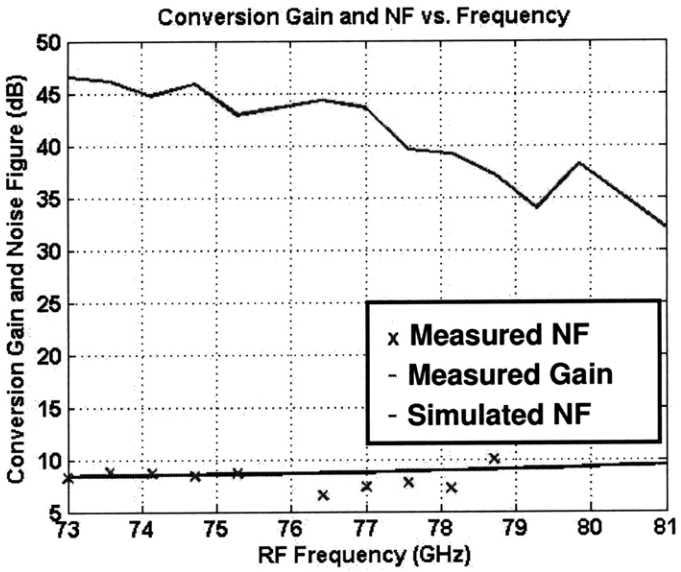

Figure 2-5: *77-GHz Front End Passive Imager, Conversion Gain and NF Measurement vs. Simulation, off-chip LO.*

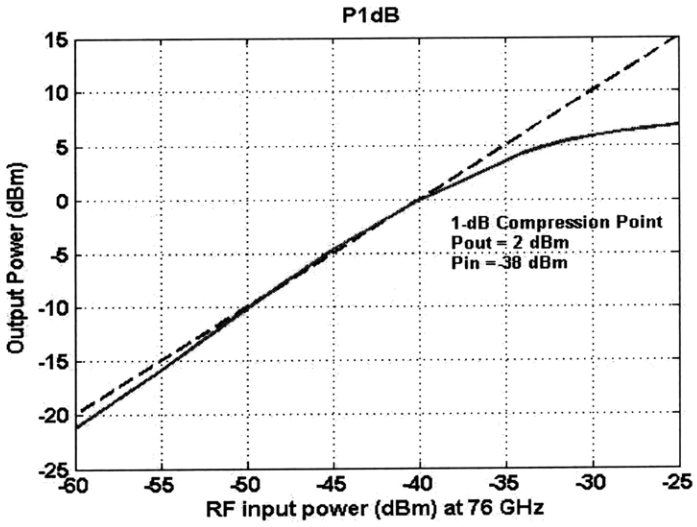

Figure 2-6: *77-GHz Front End Passive Imager IP1dB, off-chip LO.*

conversion gain measurements in Figure 2-7 show general agreement in that the gain is highest within the frequency range of 73-77 GHz, with degradation at higher RF frequencies. However, a discrepancy exists in that the simulated conversion gain is approximately 50-55 dB, while the measured gain is considerably less than expected. A number of reasons could explain the relative loss in expected gain, including losses incurred due to impedance mismatch at the LNA/Mixer interface, and also an overly optimistic modeling of capacitive and resistive parasitics in the simulation extraction tool.

It is certainly likely that some loss was incurred due to the interface between the LNA and mixer, which does not attain the ideal 50 ohm impedance match that each individual block was designed and simulated for. Due to non-ideal RF port S11 and S22 of the mixer and LNA, respectively, intermediate reflections can occur and limit the optimal gain. This effect of loss in conversion gain has been verified in simulation by introducing a resistive mismatch between the output port of the LNA and the input port of the mixer. This effect can also clearly be theoretically and intuitively extrapolated. Approximately 10-dB of conversion loss can be introduced if the impedance mismatch between the mixer and LNA ports is 25-ohms. Figure 2-8 illustrates the simulated results vs. measured results with the introduction of a resistive mismatch between the LNA/Mixer ports.

In general, the conversion gain trends for the off-chip LO and on-chip LO are comparable to each other. The simulated results show a decrease in conversion gain for higher RF frequencies, which is also exhibited in the measured results, albeit more pronounced. This is due to the relative decreases in measured LNA and Mixer gain at these frequencies, where the gain peaked and the input/output impedance matched more closely for lower frequencies, exhibiting a more resonant behavior due to unmodelled parasitic inductance which was not extracted in simulation. These results are explained more thorougly in both the LNA and Mixer sections of this thesis. Despite the discrepancy observed in the measured vs. simulated conversion gain, the receiver still exhibits impressive gain results. To the best of the author's knowledge, this is the highest-gain SiGe imager front-end reported for this frequency

range, simultaneously with the lowest reported noise figure.

The Noise Figure of the front end receiver was measured using a Quinstar noise source and Agilent N8975A Noise Figure Analyzer. The measurement setup will be described in full detail in the following section. Although the NF data is presented in Figure 2-5, a closer view is provided in Figure 2-9.

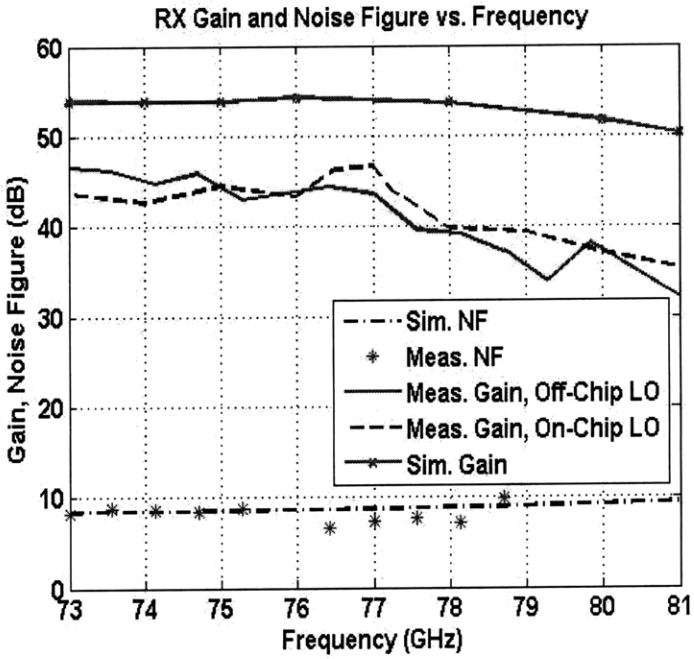

Figure 2-7: *77-GHz Simulated/Measured Conversion gain and Noise Figure for On-Chip and Off-chip LO.*

It should be noted that although the LNA Noise Figure is approximately 4.9-6.0 dB, the Noise Figure of the Front End Receiver is substantially higher (7.0-10 dB) due to noise produced by the LNA in the image band (63-71 GHz). This noise is downconverted by the mixer, which then appears in the IF frequency band. This noise can be mitigated by the use of an image-reject filter, if designed properly, with minimum insertion loss and maximum stopband rejection. For the particular application of imaging, a relatively wideband filter is also required. However, this design task is not trivial, and is susceptible to large discrepancies between simulated and measured impedance values due to inaccurate coupled transmission line models

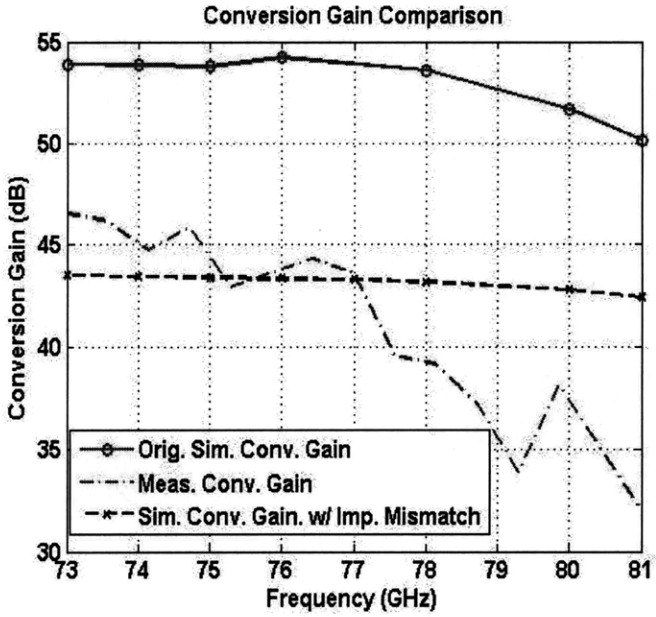

Figure 2-8: *77-GHz Conversion Gain Comparison: Introducing impedance mismatch between the LNA and Mixer ports results in /approx10-dB loss in gain.*

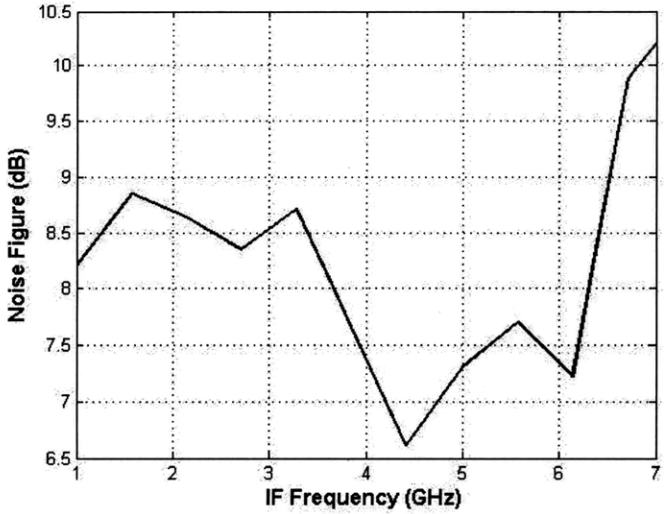

Figure 2-9: *77-GHz Front End Noise Figure Measurement.*

in the design package.

Figure 2-10 illustrates a Chebychev bandpass filter designed in Ansoft Designer SV. This particular design can be implemented in silicon using coupled transmission lines, adjusting transmission line widths for the impedances depicted. Transmission line lengths can then be adjusted for desired frequency operation. This particular configuration was chosen because coupled transmission lines are available in the SiGe design kit, and they perform particularly well for on-chip filter design.

Noise figure improvements can readily be seen via simulation when a low-loss bandpass filter is placed in between the LNA and mixer in the RF Front End design, as shown in Figure 2-11. As depicted, a Noise Figure improvement of 1-3 dB can be achieved, provided that the filter exhibits low insertion loss and bandwidth performance as simulated (Figure 2-12). Recent work presented in [30] also provides low-insertion loss 77-GHz bandpass filters designed in SiGe. Other SiGe and CMOS bandpass filters have been designed and published, as well: [17,31].

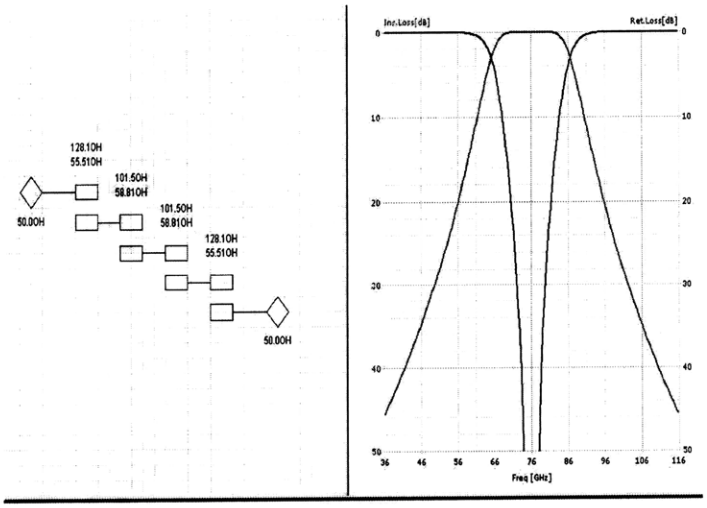

Figure 2-10: *Coupled-wire Chebychev Filter design with Ansoft Designer SV.*

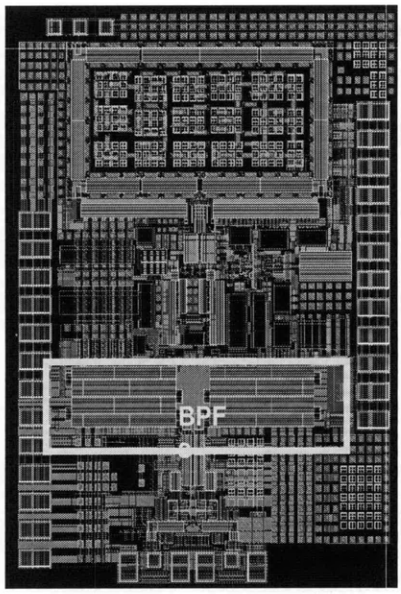

Figure 2-11: *Image-Reject Filter Inserted between LNA and Mixer.*

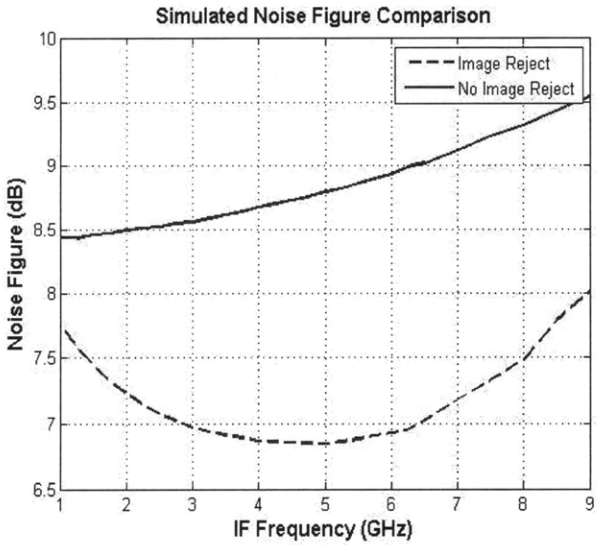

Figure 2-12: *NF simulated results indicating NF improvement with Chebychev Band-pass Image-Reject Filters.*

Measurement setup

The measurement setup and equipment are significantly important when testing at millimeter-wave frequencies approaching 100 GHz. When measuring virtually any parameter, the output must be externally mixed down to an IF frequency that can be read by either a spectrum analyzer, network analyzer, or noise figure analyzer (NFA). Output power can be measured directly, however, using a W-band power sensor. Output power is generally observed on a spectrum analyzer and verified on a W-band power meter. Conversion Gain can be measured on a spectrum analyzer or NFA. However, since the NFA allows for calibration of external components, taking into account virtually all power losses through external components, it provides for a more straightforward measurement that can be verified on a spectrum analyzer. This method simultaneously provides a noise figure measurement, as well. Input-referred 1-dB compression point must be measured on a spectrum analyzer at a given frequency, while checking the output power consistently until the output power reaches a point which is 1 dB lower than it should be for linear operation. The impedance S-parameters are all measured on a vector network analyzer. This measurement setup is fully detailed in the Antenna Chapter.

The spectrum analyzer used in these measurements is the Agilent E4440A 3Hz-26.5 GHz PSA Series Spectrum Analyzer. An external module and mixer enables viewing of signals up to 110 GHz. The network analyzer used in these measurements is the Agilent E8361A Vector Network Analyzer (VNA). The VNA is operable from 10 MHz-67 GHz, but extended frequency operation is enabled with the use of an external source module which mixes the operable frequency up to 110 GHz. The noise figure analyzer (NFA) is the Agilent N8975A, which operates up to 26.5 GHz, but also needs external noise sources to cover V-band (50-75 GHz) and W-band (75-110 GHz) operation. Figure 2-13 illustrates the setup for the noise figure measurement. First, the NFA calibrates the losses and gains from each element without the DUT (Device Under Test) connected, such that the noise figure and gain are zero upon calibration. Next, the device under test is connected so NF and gain data can be recorded. In

this case, the DUT is an amplifier, but in the case of the 77- or 94-GHz receiver test, the RF Front End replaces the external downconverter in the NF test setup. In this case, the IF signal from the RF front end is fed to an external Anaren balun (either 1-2 GHz, 2-4 GHz, or 4-8 GHz, depending on the IF frequency of interest), and then directly into the IF input of the NFA. The 94-GHz receiver system requires different external amplifiers and downconverters, which operate in the range from 90-98 GHz.

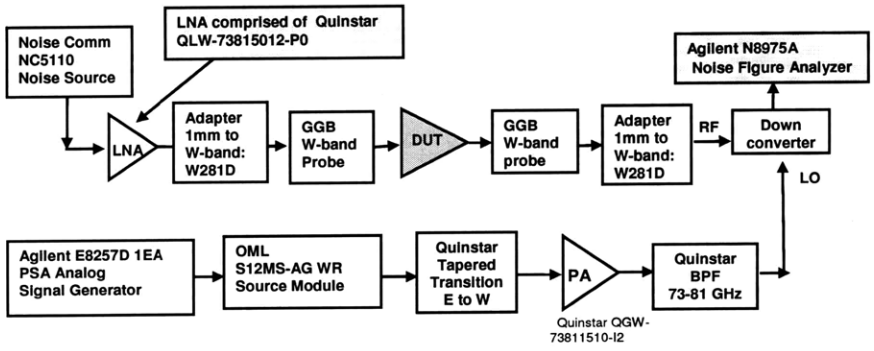

Figure 2-13: *Noise Figure measurement.*

2.3 94-GHz Front End

Due to sensitivity requirements in Passive Imaging Systems, atmospheric attenuation is a substantial concern. Given that atmospheric absorption is significantly minimized at the 94-GHz band, this provides an excellent opportunity for passive imaging applications. [1] As the 77-GHz system is designed for 8GHz of IF bandwidth, operating in the 73-81 GHz band with a 72 GHz LO, the 94-GHz system is also designed for 8 GHz of IF bandwidth. A 90-GHz LO signal is used, and the RF signal is swept from 91-99 GHz.

The topology of this 94-GHz Front End is the same as that of the 77-GHz design, with the input and output matching networks of the LNA re-tuned for optimal performance at 94-GHz, using the same impedance-matching methods described in

the LNA chapter. The mixer input matching is also slightly adjusted in order to achieve a better high frequency impedance match. The majority of the analaysis, layout and measurement issues that applied in the 77-GHz design still apply in the 94-GHz system design. The 94 GHz system provides benefits in the form of higher image resolution, superior atmospheric absorption, and smaller feature sizes. The 94-GHz frequency is the regime at which most millimeter-wave passive imaging is explored. [1] The 94-GHz Front End chip photo is shown in Figure 2-14.

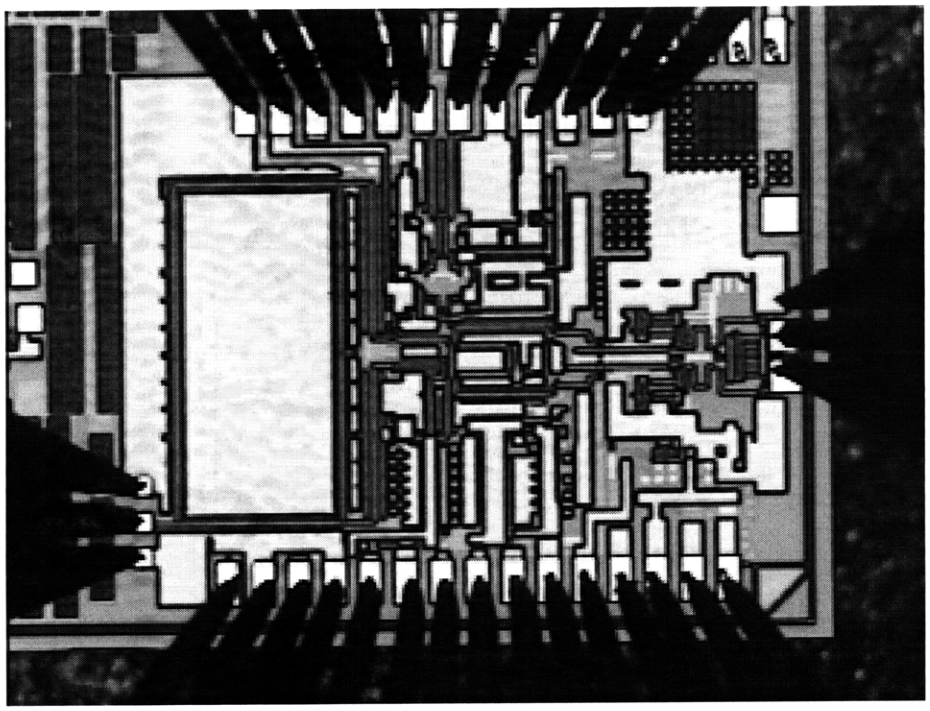

Figure 2-14: *94-GHz Chip Photo.*

2.3.1 Characterization

The 94-GHz Front End is characterized in the same manner as that of the 77-GHz system, albeit the LO signal is external, and the majority of external test components are designed for operation in the 90-98 GHz range. The LNA results are presented in the LNA chapter. At 90 GHz, however, the standalone LNA achieved 22 dB Gain, 7 dB NF, -25 dB input return loss, and an output return loss of -9.5 dB (this still corresponds to $VSWR < 2$). However, it is suspected that since the LNA is integrated

with the mixer, it achieved a higher center frequency because the output bondpads were removed, thereby eliminating a significant amount of parasitic capacitance at the output. The mixer was not characterized in this particular case, since the baluns at the LO and RF port used for test purposes would affect the operating frequency.

Chip Results

The 94-GHz LNA/Mixer/IF Amplifier combination simulated vs. measured NF and conversion gain plot is shown in Figure 2-15. The measurement shows generally good agreement with the simulated results. However, the extracted simulation had to be modified as the input bondpads had double extracted parasitic capacitance, which initially made the noise figure significantly pessimistic. The gain curve shows a more pronounced decline at higher frequencies than that of the simulation. This also is consistent with the measured vs. simulated results of the standalone LNA, which showed more peaking gain at its center frequency than its simulated result, due to additional unmodelled parasitic inductance at the output.

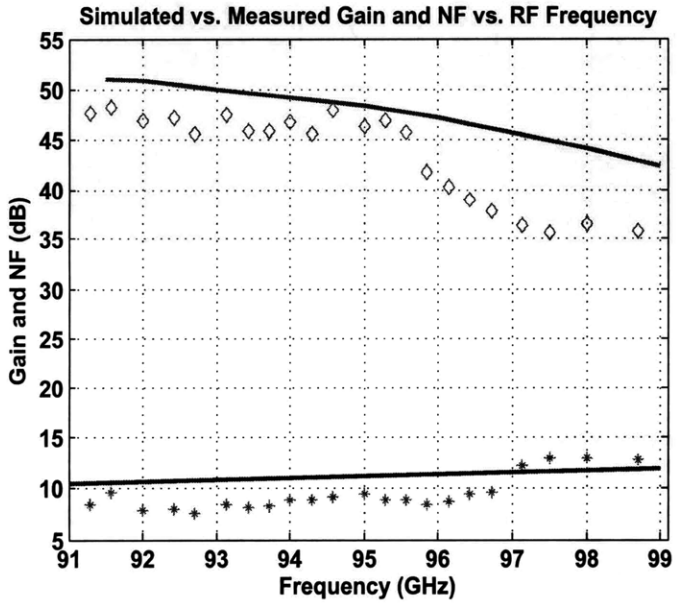

Figure 2-15: *94 GHz Front End Conversion Gain and Noise Figure (Simulated vs. Measured).*

The 94-GHz Front End performs very well in terms of gain and noise figure, with $\approx$ 45 dB of conversion gain from 91-95.5 GHz, and 35-45 dB of gain throughout the 91-99 GHz frequency range. The noise figure results were equally impressive, with values averaging 8 dB up through 96 GHz, making this an exceptional front end receiver for at least 5 GHz of bandwidth, and certainly viable throughout the frequency range of 91-99 GHz.

2.4 Antenna Flip-Chip Packaging and Test

The packaging of the antenna involves a flip-chip bonding method, whereby each side of the antenna input is secured to an input bondpad terminal on the chip. The primary connection to the bondpad is made with a gold wirebond which is truncated to make a stud bump. This is then "coined", or essentially sanded down, for smoothness (as illustrated by Figure 2-16). After the coining process, a conductive silver epoxy is applied to the top of the gold stud bumps. Finally, the antenna is soldered to the gold bumps and connected through the silver epoxy. Non-conductive epoxy was also applied in this process in order to more properly secure the antennas in place. Figure 2-17 illustrates an example of the gold stud-bump processing that is done at Lincoln Laboratory. The antenna packaging work was all done at Lincoln Laboratory, primarily by Karen Parrillo.

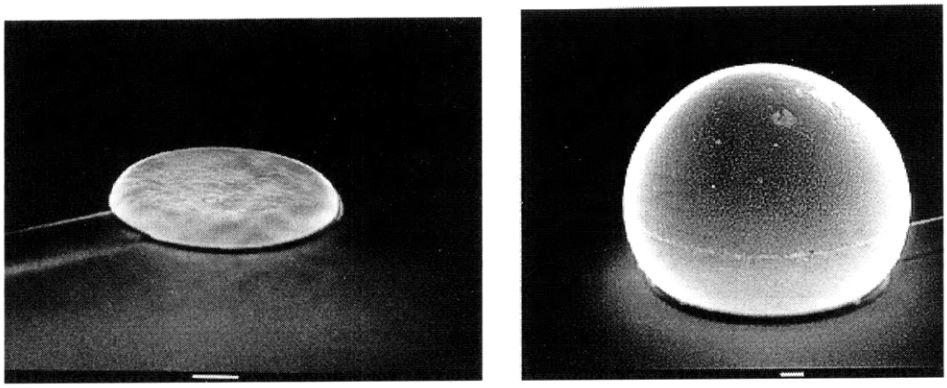

Figure 2-16: *Coining process enables smooth, consistent surface. Right: Original Solder Bump. Left: Coined Solder Bump.*

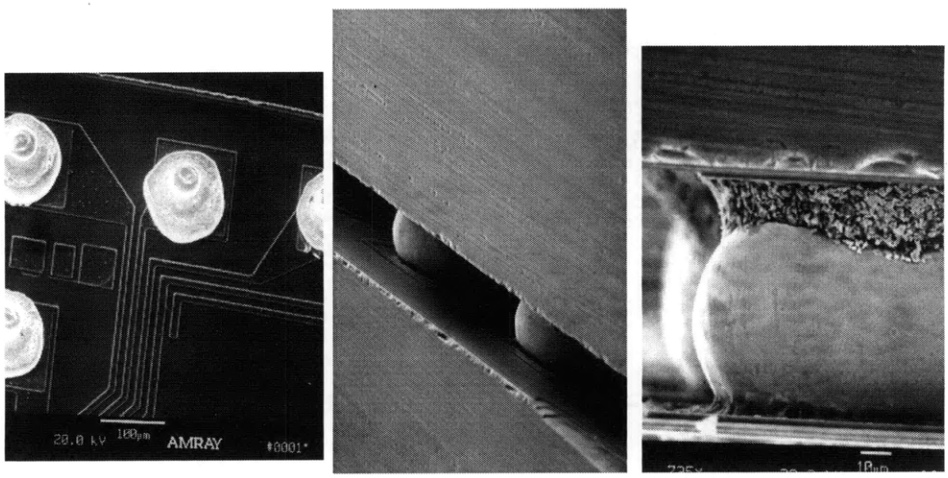

Figure 2-17: *Illustration of Gold Stud Bumps enabling flip-chip bonding with silver epoxy.*

This particular flip-chip method for packaging the millimeter-wave antenna onto the chip is arguably the best method to package a millimeter-wave chip, in that virtually all connective loss is minimized, with the exception of the small amount of loss incurred in the solder bumps. In comparison to all alternative methods for packaging an antenna on chip, including the use of highly inductive wirebonds, lossy transmission line feeds, or (in the lossiest case) on-chip antennas, this is the optimal packaging technology known to date. Another key advantage of the particular method used in this thesis is that the antenna radiates off of the edge of the chip, which further increases its bandwidth and radiation efficiency over more traditional microstrip antennas. More details will follow this argument in the Antenna section of this thesis. Figure 2-18 and 2-19 shows the overall antenna fabrication concept, as the antenna is securely connected to the LNA bondpad terminals.

Transmit/Receive Antenna Verification

The integrated antenna has been verified on the 94-GHz LNA, the 77-GHz Front End receiver and also on an on-chip antenna test structure. In the case of the 94-GHz LNA, the verification setup involved a transmit antenna placed 2.75 cm away from the LNA with the flip-chip integrated antenna. The transmit power was recorded at

Figure 2-18: *Close-up Chip Photo with Antenna securely connected via gold solder bumps.*

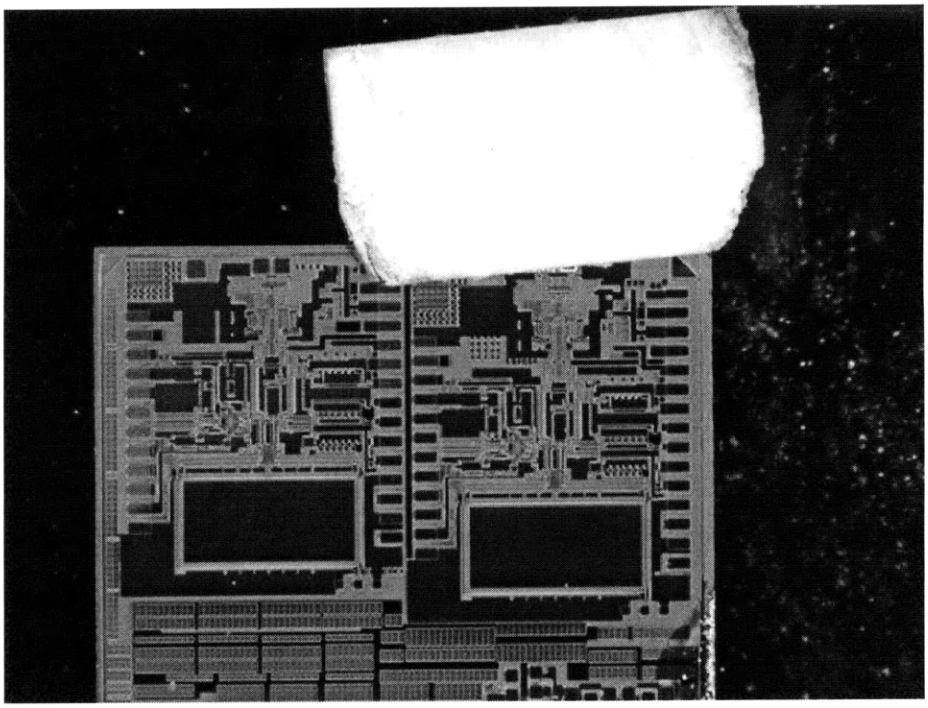

Figure 2-19: *Chip Photo with Antenna securely connected via gold solder bumps.*

the transmit antenna terminals, and the output power of the LNA was recorded on a spectrum analyzer after being amplified and mixed down by an external mixer. All power losses were taken into account as the RF transmit frequency was swept from 91-99 GHz. The external amplifier at the output of the LNA had gains of 30 dB, 31.1 dB, and 29.8 dB at 90, 94 and 98 GHz, respectively. The mixer had conversion losses of 29.63 dB, 31.77 dB, and 29.4 dB at those frequencies, averaging ≈30 dB of conversion loss from 91-99 GHz. The waveguide adapter and Gore brand cable had 6.5 dB attenuation (measured on a power sensor), the IF cables had ≈ 2 dB attenuation (measured on a network analyzer), and the GSG probe had ≈ 1.7 dB attenuation (given by its spec sheet). Another loss to be taken into account was a 3-dB loss due to the fact that this was a single-ended measurement. All of these losses added to 12.2 dB- 13.2 dB from 91-99 GHz, with the mixer conversion loss approximately canceling out the external amplifier gain (although these loss measurements are still taken into account in the calculations).

The main procedure involved in verifying the integrated antenna efficacy was to record the output power, carefully de-embed all of the power losses, including the propagation path loss, and verify that the receive antenna gain was approximately the expected value as determined by the antenna characterization, which is thoroughly detailed in the Antenna chapter of this thesis.

Using the same bias values for the LNA as the values used in its S-parameter characterization, it is assumed that the LNA achieves the same gain as the prior measurement depicts. Specifically, the LNA achieves 22 dB of gain at its very highest point (90 GHz), and falls somewhat constantly from that point with increasing frequency. The LNA was designed for a center frequency of ≈ 94 GHz, but due to extraneous parasitics, the center frequency was shifted down. A plot of the LNA gain measurement is shown, for reference, in Figure 2-20.

The Friis Transmission Equation is used in order to determine the unknown parameter G_r, or receive antenna gain, in the following equation:

$$Friis\ \ Transmission\ \ Formula: \quad \frac{P_r}{P_t} = G_t G_r \left(\frac{\lambda}{4\pi R}\right)^2 \tag{2.3}$$

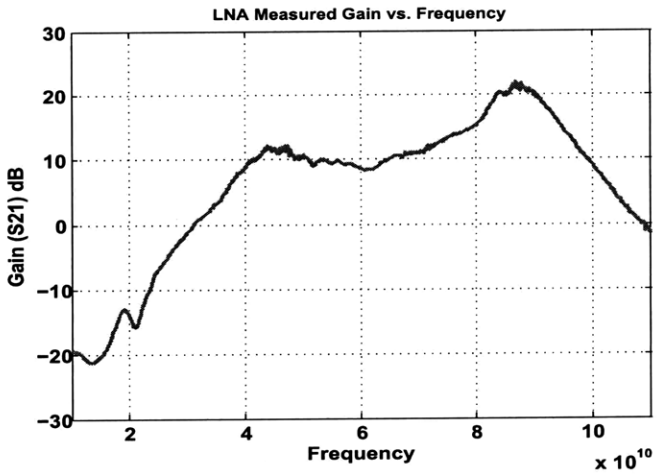

Figure 2-20: *LNA Measured Gain.*

This equation's derivation can be found in several references ([32–34]), and essentially enables calculation of a single unknown parameter within a given transmission link. In this particular case, all parameters are known but the receive antenna gain, as every other parameter is extrapolated from known values, to within a reasonable margin of error. The transmit power, P_t, is recorded at the input of the transmit probe which feeds the transmit antenna (in this case, -2.05 dBm). The transmit gain is extrapolated from known measured values of the characterized antenna, given its frequency, azimuth and elevation angle on the probe station. The transmit antenna was not positioned for maximum gain, as this was not allowable, given the constraints of the probe station and the positioning angles of the probes. As such, the transmit antenna was positioned for a gain of $G_t \approx 8$ dB in the direction of the receiver, corresponding to an elevation angle of 10 degrees, 60 degrees off from its main beamwidth in the azimuth direction (corresponding closely to the plots in Appendix A indicating an azimuth angle of 30 degrees). All of these values can be referenced in the Antenna chapter, or in Appendix A. The propagation path loss, given by $\left(\frac{\lambda}{4\pi R}\right)^2$, is frequency dependent, while the distance R remains constant at 2.75 cm. This path loss ranged

from -40.4 dB to -41.1 dB from 91-99 GHz, respectively. The parameter of received power incident at the receive antenna terminals P_r remains the last parameter which must be extrapolated in order to determine the receive antenna gain G_r. This is calculated by the following equation:

$$P_r + G_{LNA} - Loss_{Mixer} + G_{ExtAmp} - Loss_{total} = P_{out} \tag{2.4}$$

where G_{LNA} is taken from the measured LNA data, $Loss_{Mixer}$ is taken from the measured conversion loss of the external mixer for a given frequency from 91-99 GHz, G_{ExtAmp} is taken from the measurements of the external amplifier for varying frequency, and $Loss_{total}$ is the total loss measurement of the mm-wave cable, adapter, IF cables, and GSG probe. P_{out} is the output power, as measured by the spectrum analyzer. For example, at 91 GHz, $P_r + 19 - 29.63 + 30 - 12.2 = -20.5dBm \rightarrow P_r = -27.67$ dBm.

The Friis Transmission Formula can be modified to be represented in dB to determine G_r:

$$P_r - P_t = G_t + G_r + 20\log\left(\frac{\lambda}{4\pi R}\right) \tag{2.5}$$

Thus, $-27.67 - (-2.05) = G_t + G_r - 40.4 \rightarrow G_t + G_r \approx 14.78$ dB.

Assuming that at 91 GHz $G_t \approx 8$ dB, this yields $G_r \approx 7$ dB. This is a very reasonable result, given that the antenna on-chip is actually placed upside down to contact to the bondpads, and thus radiates through its very thin (.004", or 100 μm) dielectric. Simulation has indicated that this upside-down antenna configuration reduces the antenna gain by 0.5-1 dB. This antenna configuration, as well as the gold stud-bump solder connections, are very likely responsible for the $\approx$1 dB loss in gain. It should also be mentioned that there is a reasonable margin of error in these measurements; ie. the LNA may possibly achieve $\pm$ 1 dB of gain from the referenced measurement, or any loss parameter could have a $\pm$ 1 dB margin of error. It is still a reasonable assumption to conclude that the losses incurred due to the upside-down configuration of the antenna plus the connection through the gold solder bumps

and silver epoxy yields $\approx$ 0.5 - 1.0 dB of loss (with somewhere between 0.2-0.7 dB attributed to the solder connection), yielding a integrated antenna efficiency in the range of $\approx$ 80% to 90%.

This characterization was done throughout the frequency range of 91-99 GHz, with all of the measured losses and gains de-embedded. Although the standalone LNA peaked at 90 GHz, the integrated LNA was directly connected to the mixer without the bondpads at the output. The removal of the capacitive bondpads in the integrated LNA were expected to shift the LNA peak closer to 94 GHz, thus yielding optimal performance in the 91-99 GHz frequency range. All losses and gains are recorded in Table 2.1. Figure 2-21 depicts the measured transmit antenna gain G_t and the extrapolated receive antenna gain G_r. This figure shows the maximum gain discrepancy is 2 dB, while the minimum gain loss is $\approx$ 0.3 dB.

Table 2.1: Measured Loss & Gain Parameters in Integrated Antenna Characterization 91-99 GHz

Freq. - (GHz)	Tx Power (dBm)	Mixer Conv. Loss (dB)	Ext. Amp Gain (dB)	LNA Gain (dB)	Meas. Output Power (dBm)
91	-2.05	29.63	30	19	-20.5
92	-1.43	31.2	$\approx$30	18.1	-21.8
93	3.8	28.88	$\approx$30	17	-22.5
94	-2.5	31.77	31.1	15.8	-24.9
95	2.7	29.27	$\approx$30	15	-24.4
96	-2.88	33.2	$\approx$30	13.6	-24.7
97	0.11	26.8	$\approx$30	12.5	-25.1
98	-3.22	29.4	29.8	11	-27.1
99	-4.0	30.5	$\approx$29	10	-28.7

The 77-GHz integrated antenna was tested and characterized using an on-chip test structure, which allowed GSG probes to contact a short transmission line feed which connected directly to the integrated antenna. This eliminated extraneous circuit elements, in order to mitigate the margins of error involved in extrapolating an integrated antenna gain measurement. Namely, in this case, an integrated LNA gain, external mixer conversion loss and external LNA gain did not need to be inferred in order to extrapolate the integrated receive antenna gain. This test setup was similar

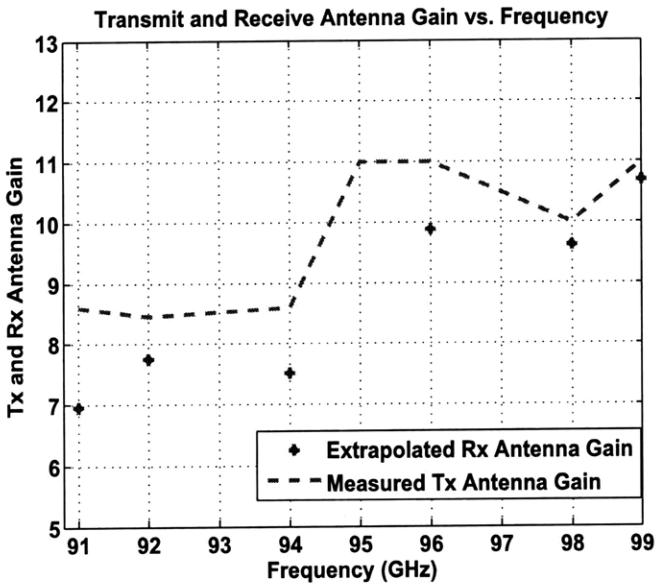

Figure 2-21: *Measured Integrated Antenna Gain and Unpackaged Antenna Gain vs. Frequency for 91-99 GHz.*

to the test setup for the 94-GHz integrated antenna, albeit without integrated circuit elements save for short transmission lines designed to emulate the 77-GHz LNA input match. Also, an external W-band mixer was used with conversion loss data uploaded to the spectrum analyzer, thus eliminating the need to measure and calculate an external mixer conversion loss. Due to the fact that the W-band mixer's conversion loss was calibrated into the spectrum analyzer, no external amplification of the receive signal was necessary.

The transmit antenna was placed in a configuration that allowed contact to the GSG probe, albeit not in a configuration for maximum gain. The integrated receive antenna was placed at an azimuth angle of approximately 30 degrees to the transmit antenna, at an elevation angle of ≈10 degrees (as in the previous case for the 94-GHz test setup). This corresponds to a transmit antenna gain G_t ≈7.5-10 dB, throughout the 73-81 GHz frequency range (See Appendix B for gain measurements). All external losses, including the losses of the probes, cables, and adapters are taken into account from 73-81 GHz. The propagation path loss is calculated based on a distance of R = 1.125", or 2.85cm, and ranged from -38.8 dB to -39.7 dB from 73-81 GHz. Table 2.1 details the calibrated losses, Tx power and Rx power. In addition to these recorded losses, 1.7 dB is taken into account for each GSG probe.

Figure 2-22 illustrates the measured values of the integrated receiver antenna gain and the transmit antenna gain vs. frequency (as characterized in the Antenna chapter). The maximum gain discrepancy is 2.5 dB, while the minimum gain discrepancy is 0 dB; however, for the majority of the measured data vs. frequency, the gain discrepancy is 1 dB. Therefore, while the 2 worst-case measurements of efficiency are ≈ 63% and the best-case measurement is ≈ 100%, generally throughout the 73-81 GHz band, the efficiency of the antenna package ranges from ≈ 80% to 90%.

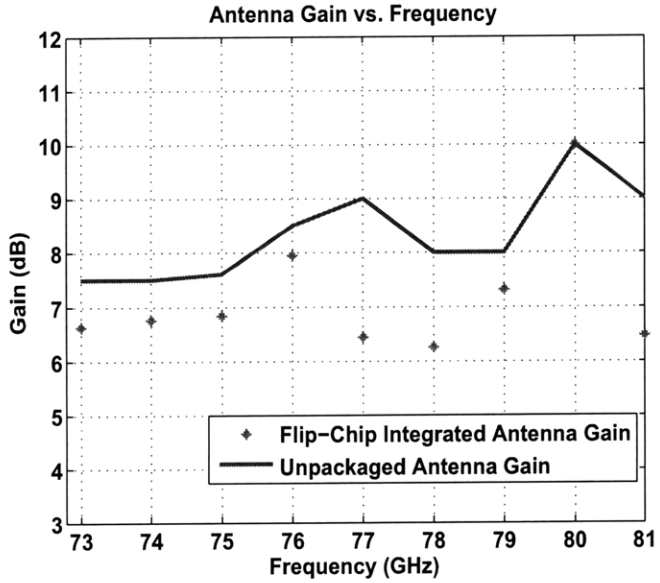

Figure 2-22: *Measured Integrated Antenna Gain and Unpackaged Antenna Gain vs. Frequency for 73-81 GHz.*

Table 2.2: Measured Loss & Gain Parameters in Integrated Antenna Characterization: 73-81 GHz

Freq. (GHz)	Adapter + Cable Losses	Propagation Path Loss	Tx Power (dBm)	Rx Power (dBm)	Tx Ant. Gain (dB)
73	-6.79	-38.8	-7.2	-42.1	7.5
74	-9.81	-38.9	-5.25	-43.15	7.5
75	-6.97	-39.1	-7.0	-42	7.6
76	-7.27	-39.2	-4.59	-38	8.5
77	-7.12	-39.3	-4.94	-39.3	9.0
78	-5.65	-39.4	-5.0	-39.2	8.0
79	-4.89	-39.5	-7.5	-40	8.0
80	-5.37	-39.6	-8.3	-36.7	10.0
81	-4.83	-39.7	-6.5	-39	9.0

Chapter 3

Wideband Millimeter-Wave Antenna

Several requirements are set forth by the passive imaging system design for the antenna. Impedance match, copper and resistive losses must be optimized so as to minimize the amount of loss seen at the antenna terminals, as this translates directly into noise figure. The efficiency measurement of an antenna takes these impedance and radiation losses into account. The antenna bandwidth must be wide, as the system requires 8-GHz of operable bandwidth. Also desirable is high antenna gain and directivity.

In order to understand the challenges that the antenna design introduces, a comprehensive background outlining several characterizing antenna parameters will be presented. Several parameters have been defined in order to characterize antennas and determine optimal applications. One very useful reference is the IEEE Standard Definitions of Terms for Antennas [35].

Several factors are considered in the simulation, design and testing of an antenna, and most of these metrics are described in the following section. These parameters must be discussed and defined before a basic understanding of antenna requirements for a particular application can be achieved.

3.1 Fundamental Antenna Characteristics

The following section provides an introductory tutorial to define basic antenna parameters for readers without a comprehensive background.

3.1.1 Impedance Bandwidth

Impedance bandwidth indicates the bandwidth for which the antenna is sufficiently matched to its input transmission line such that 10% or less of the incident signal is lost due to reflections. Impedance bandwidth measurements include the characterization of the Voltage Standing Wave Ratio (VSWR) and return loss throughout the band of interest. VSWR and return loss are both dependent on the measurement of the reflection coefficient Γ. Γ is defined as ratio of the reflected wave Vo- to the incident wave Vo+ at a transmission line load as shown in Figure 3-1, and can be calculated by equation 3.1

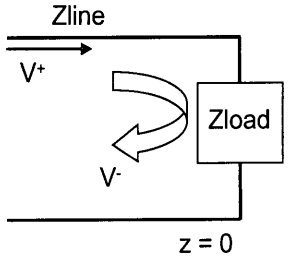

Figure 3-1: *Transmission Line Model.*

$$\Gamma = \frac{V_{o-}}{V_{o+}} = \frac{Z_{line} - Z_{load}}{Z_{line} + Z_{load}} \tag{3.1}$$

Z_{line} and Z_{load} are the transmission line impedance and the load (antenna) impedance, respectively. The voltage and current through the transmission line as a function of the distance from the load, z, are given as follows:

$$V(z) = V_{o+}e^{-j\beta z} + V_{o-}e^{j\beta z} = V_{o+}e^{-j\beta z} + \Gamma e^{j\beta z} \tag{3.2}$$

$$I(z) = \frac{1}{Z_o} V_{o+} e^{-j\beta z} - V_{o-} e^{j\beta z} = \frac{V_{o+}}{Z_o} e^{-j\beta z} - \Gamma e^{j\beta z} \tag{3.3}$$

where $\beta = \frac{2\pi}{\lambda}$.

The reflection coefficient Γ is equivalent to the S11 parameter of the scattering matrix. A perfect impedance match would be indicated by Γ= 0. The worst impedance match is given by Γ= -1 or 1, corresponding to a load impedance of a short or an open.

Power reflected at the terminals of the antenna is the main concern related to impedance matching. Time-average power flow is usually measured along a transmission line to determine the net average power delivered to the load. The average incident power is given by:

$$P^i_{ave} = \frac{|V_{o+}|^2}{2Z_o} \tag{3.4}$$

The reflected power is proportional to the incident power by a multiplicative factor of $|\Gamma|^2$, as follows:

$$P^r_{ave} = -|\Gamma|^2 \frac{|V_{o+}|^2}{2Z_o} \tag{3.5}$$

The net average power delivered to the load, then, is the sum of the average incident and average reflected power:

$$P_{ave} = \frac{|V_{o+}|^2}{2Z_o} \left(1 - |\Gamma|^2\right) \tag{3.6}$$

Since power delivered to the load is proportional to $(1 - |\Gamma|^2)$, an acceptable value of Γ that enables only 10% reflected power can be calculated. This result is Γ= 0.3162.

When a load is not perfectly matched to the transmission line, reflections at the load cause a negative traveling wave to propagate down the transmission line. Ultimately, this creates unwanted standing waves in the transmission line. VSWR measures the ratio of the amplitudes of the maximum standing wave to the minimum

standing wave, and can be calculated by the equation below:

$$VSWR = \frac{V_{max}}{V_{min}} = \frac{1 + |\Gamma|}{1 - |\Gamma|} \tag{3.7}$$

The desired values of VSWR which indicate a good impedance match is 2.0 or less. This corresponds to less than 10% of reflected power due to impedance mismatch. This VSWR limit is derived from the value of Γ calculated above.

Return loss is another measure of impedance match quality, also dependent on the value of Γ, or S11. Antenna return loss is calculated by the following equation:

$$Return \;\; Loss = -10 \log |S_{11}|^2 = -20 \log \Gamma \tag{3.8}$$

A good impedance match is indicated by a return loss greater than 10 dB. A summary of desired antenna impedance parameters include $\Gamma < 0.3162$, $VSWR < 2$, and Return Loss $> 10dB$.

3.1.2 Radiation Pattern

One of the most common descriptors of an antenna is its radiation pattern. Radiation pattern can easily indicate an application for which an antenna will be used. For example, cell phone use would necessitate a nearly omnidirectional antenna, as the user's location is unknown. Therefore, radiation power should be spread out uniformly around the user for optimal reception. However, for satellite applications, a highly directive antenna would be desired such that the majority of radiated power is directed to a specific, known location. According to the IEEE Standard Definitions of Terms for Antennas [35], an antenna radiation pattern (or antenna pattern) is defined as follows:

"a mathematical function or a graphical representation of the radiation properties of the antenna as a function of space coordinates. In most cases, the radiation pattern is determined in the far-field region and is represented as a function of the directional coordinates. Radiation properties include power flux density, radiation intensity, field strength, directivity phase or polarization."

Three dimensional radiation patterns are measured on a spherical coordinate system indicating relative strength of radiation power in the far field sphere surrounding the antenna. On the spherical coordinate system, the x-z plane (θ measurement where ϕ =0°) usually indicates the elevation plane, while the x-y plane (ϕ measurement where θ =90°) indicates the azimuth plane. Typically, the elevation plane will contain the electric-field vector (E-plane) and the direction of maximum radiation, and the azimuth plane will contain the magnetic-field vector (H-Plane) and the direction of maximum radiation. A two-dimensional radiation pattern is plotted on a polar plot with varying θ or ϕ for a fixed value of ϕ or θ , respectively. Figure 3-2 illustrates a half-wave dipole and its three-dimensional radiation pattern. The gain is expressed in dBi, which means that the gain is referred to an isotropic radiator. Figure 3-3 illustrates the two dimensional radiation patterns for varying θ at ϕ =0° , and varying ϕ at θ =90° , respectively. It can be seen quite clearly in Figure 3-2 that the maximum radiation power occurs along the θ =90 plane, or for any varying ϕ in the azimuth plane. The nulls in the radiation pattern occur at the ends of the dipole along the z-axis (or at θ =0° and 180°). By inspection, the two dimensional polar plots clearly show these characteristics, as well. Figure 3-3 shows the radiation pattern of the antenna as the value in the azimuth plane is held constant and the elevation plane (θ) is varied (left), and to the right, it shows the radiation pattern of the antenna as the value in the elevation plane is held constant (in the direction of maximum radiation, =90°) as ϕ varies, and no distinction in the radiation pattern is discernable.

While many two-dimensional radiation patterns are required for a fully complete picture of the three-dimensional radiation pattern, the two most important measurements are the E-plane and H-plane patterns. The E-plane is the plane containing the electric field vector and direction of maximum radiation, and the H-plane is the plane containing the magnetic field vector and direction of maximum radiation. While Figure 3-3 shows simply two "cuts" of the antenna radiation pattern, the three-dimensional pattern can clearly be inferred from these two-dimensional illustrations.

The patterns and model in Figure 3-2 and Figure 3-3 illustrate the radiation

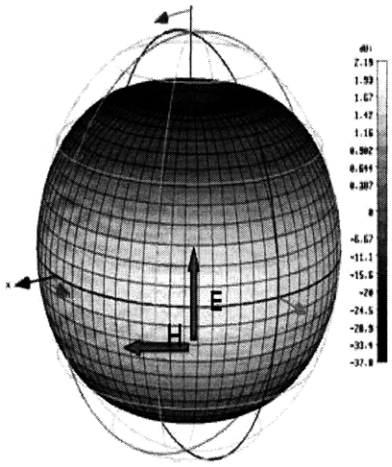

Figure 3-2: *Dipole Radiation Model, simulated in CST Microwave Studio.*

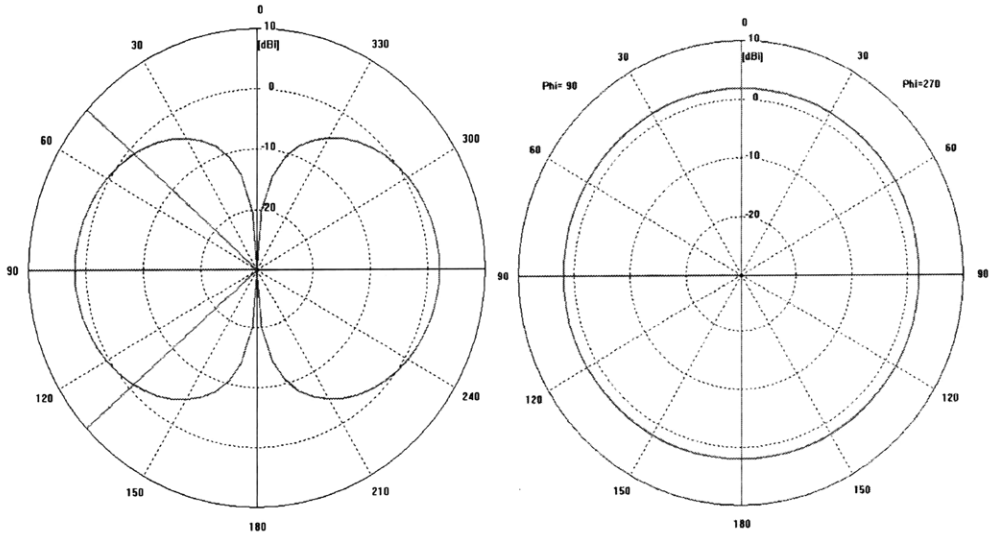

Figure 3-3: *Two-Dimensional Radiation Pattern for half-wave dipole: Varying* θ*,* $\phi = 0°$ *(left) and varying* $\phi, \theta = 0°$ *(right)*

characteristics of a half-wavelength dipole, which is virtually considered an omnidirectional radiator. The only true omnidirectional radiator is that of an isotropic source, which exists only in theory. The IEEE Standard Definitions of Terms for Antennas defines an isotropic radiator as "a hypothetical lossless antenna having equal radiation in all directions." A true omnidirectional source would have no nulls in its radiation pattern, and therefore have a directivity measurement of 0 dBi. However, since no source in nature is truly isotropic, a directive antenna typically refers to an antenna that is more directive than the half-wave dipole of the figures above.

An example of a directive antenna is the Computer Simulation Technology (CST) Microwave Studio Horn antenna illustrated in Figure 3-4, along with its three-dimensional radiation pattern. This shows clearly the direction of maximum radiation that lies along $\theta = 0°$, and no back radiation (or back lobes). Since this radiation pattern is simulated in an ideal environment with an infinite ground plane, no back lobe radiation has been simulated. The only lobes observable are the maximum radiation lobe and the smaller side lobes. However, in a realistic measurement conducted with a finite sized ground plane, back lobe radiation would be observed in which radiation would escape to the back of the ground plane. This simulation model suffices, however, to illustrate the radiation characteristics of a directive antenna versus the virtually omnidirectional half-wave dipole of in Figure 3-2 and Figure 3-3. Figure 3-5 shows the principal E-plane and H-plane measurements of the horn antenna, clearly illustrating the characteristics indicated in the three-dimensional radiation plot. The leftmost illustration of Figure 3-5 holds ϕ constant while varying θ , while the plot on the right holds θ constant while varying ϕ. A pronounced difference in the directivity of maximum radiation is clearly apparent.

3.1.3 Half-Power Beamwidth

Half power beamwidth (HPBW) is defined as the angular distance from the center of the main beam to the point at which the radiation power is reduced by 3 dB. This measurement is taken at two points from the center of the main beam such that this angular distance is centered about the main beam. This measurement is clearly

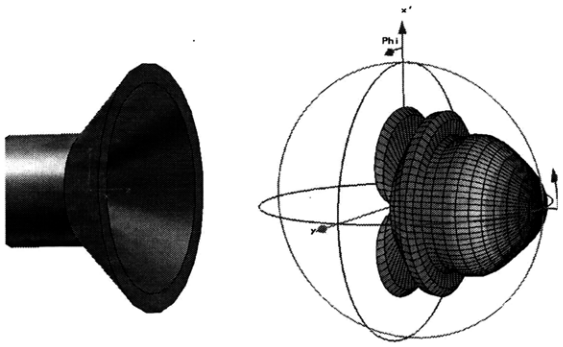

Figure 3-4: *CST Microwave Studio model of horn antenna and simulated 3D radiation pattern*

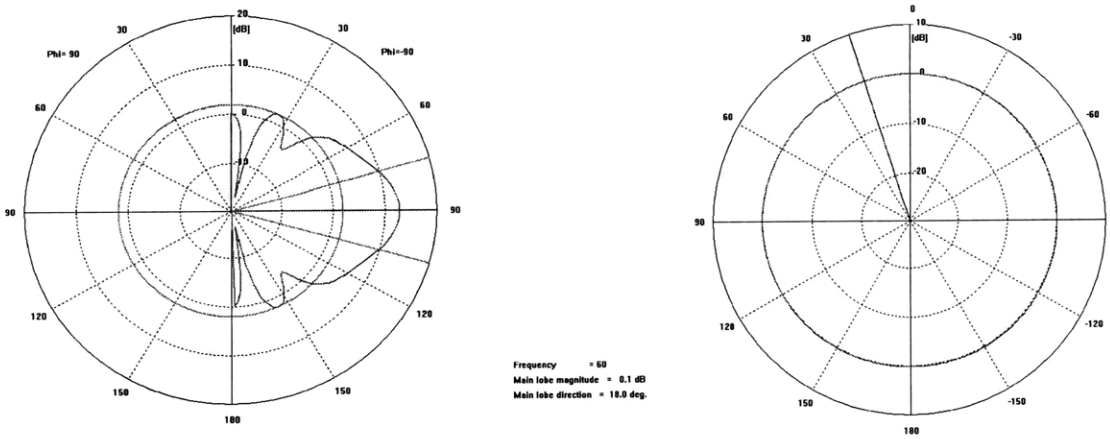

Figure 3-5: *CST Microwave Studio simulated radiation pattern. Varying* θ, $\phi = 0°$ *(left). Varying* $\phi, \theta = 0°$ *(right)*

indicated in the two dimensional plot simulations of Figure 5 and Figure 7, labeled as "Angular width (3dB)". This measurement is useful in order to describe the radiation pattern of an antenna and to indicate how directive it is.

3.1.4 Directivity

According to IEEE Standard Definitions of Terms for Antennas [35], the directivity of an antenna is defined as "the ratio of the radiation intensity in a given direction from the antenna to the radiation intensity averaged over all directions. The average radiation intensity is equal to the total power radiated by the antenna divided by 4." Directivity is more thoroughly understood theoretically when an explanation of radiation power density, radiation intensity and beam solid angle are given. References [32, 33, 36, 37] should be referred to for more thorough explanation.

The average radiation power density is expressed as follows:

$$S_{ave} = \frac{1}{2} Re[\overline{E} x \overline{H} *] \quad \frac{W}{m^2} \tag{3.9}$$

Since S_{ave} is the average power density, the total power intercepted by a closed surface can be obtained by integrating the normal component of the average power density over the entire closed surface. Then, the total radiated power is given by the following expression:

$$P_{rad} = P_{ave} = \frac{1}{2} \iint Re(\overline{E} x \overline{H} *) \bullet ds = \iint S_{rad} \bullet ds \tag{3.10}$$

Radiation intensity is defined by the IEEE Standard Definitions of Terms for Antennas as "the power radiated from an antenna per unit solid angle." The radiation intensity is simply the average radiation density, S_{rad}, scaled by the square product of the distance, r. This is also a far field approximation, and is given by:

$$U = r^2 S_{rad} \tag{3.11}$$

where U = radiation intensity ($\frac{W}{unitsolidangle}$), and S_{rad} = radiation density ($\frac{W}{m^2}$).

The total radiated power, Prad, can be then be found by integrating the radiation intensity over the solid angle of 4 steradians, given as:

$$P_{rad} = \iint_{\Omega} U d\Omega = \int_0^{2\pi} \int_0^{\pi} U sin\Theta d\Theta d\phi \tag{3.12}$$

$$P_{rad} = \iint_{\Omega} U_o d\Omega = U_o \iint_{\Omega} d\Omega = 4\pi U_o \tag{3.13}$$

where dΩ is the element of solid angle of a sphere, measured in steradians. A steradian is defined as "a unit of measure equal to the solid angle subtended at the center of a sphere by an area on the surface of the sphere that is equal to the radius squared." Integration of $d\Omega$ over a spherical area as shown in the equation above yields 4π steradians. Another way to consider the steradian measurement is to consider a radian measurement: The circumference of a circle is $2\pi r$, and there are $(2/r)$ radians in a circle. The area of a sphere is $4\pi r^2$, and there are $4\pi r 2/r^2$ steradians in a sphere.

The beam solid angle is defined as the subtended area through the sphere divided by r^2:

$$d_{\Omega} = \frac{dA}{r^2} = sin\Theta d\Theta d\phi \tag{3.14}$$

Given the above theoretical and mathematical explanations of radiation power density, radiation intensity and beam solid angle, a more complete understanding of antenna directivity can be achieved. Directivity is defined mathematically as:

$$D = \frac{U}{U_o} = \frac{4\pi U}{P_{rad}} \quad (dimensionless) \tag{3.15}$$

Simply stated, antenna directivity is a measure of the ratio of the radiation intensity in a given direction to the radiation intensity that would be output from an isotropic source.

3.1.5 Efficiency

The antenna efficiency takes into consideration the ohmic losses of the antenna through the dielectric material and the reflective losses at the input terminals. Reflection efficiency and radiation efficiency are both taken into account to define total antenna efficiency. Reflection efficiency, or impedance mismatch efficiency, is directly related to the S11 parameter (Γ). Reflection efficiency is indicated by e_r, and is defined mathematically as follows:

$$e_r = (1 - \Gamma^2) = \ reflection\ efficiency \tag{3.16}$$

The radiation efficiency takes into account the conduction efficiency and dielectric efficiency, and is usually determined experimentally with several measurements in an anechoic chamber. Radiation efficiency is determined by the ratio of the radiated power, P_{rad} to the input power at the terminals of the antenna, P_{in}:

$$e_{rad} = \frac{P_{rad}}{P_{in}} = \ radiation\ efficiency \tag{3.17}$$

Total efficiency is simply the product of the radiation efficiency and the reflection efficiency. Reasonable values for total antenna efficiency are within the range of $60\% - 90\%$, although several commercial antennas achieve only about $50 - 60\%$ due to inexpensive, lossy dielectric materials such as FR4.

3.1.6 Gain

The antenna gain measurement is linearly related to the directivity measurement through the antenna radiation efficiency. According to [35], the antenna absolute gain is "the ratio of the intensity, in a given direction, to the radiation intensity that would be obtained if the power accepted by the antenna were radiated isotropically." Antenna gain is defined mathematically as follows:

$$G = e_{rad}D = 4\pi\frac{U(\Theta,\phi)}{P_{in}} \quad (dimensionless) \tag{3.18}$$

Also, if the direction of the gain measurement is not indicated, the direction of maximum gain is assumed. The gain measurement is referred to the power at the input terminals rather than the radiated power, so it tends to be a more thorough measurement, which reflects the losses in the antenna structure.

Gain measurement is typically misunderstood in terms of determining the quality of an antenna. A common misconception is that the higher the gain, the better the antenna. This is only true if the application requires a highly directive antenna. Since gain is linearly proportional to directivity, the gain measurement is a direct indication of how directive the antenna is (provided the antenna has adequate radiation efficiency).

3.2 Considerations for Millimeter-Wave Antenna Design

Millimeter-wave design presents interesting opportunities for antenna design and packaging, in that the antenna sizes for millimeter-wave frequency operation are on the same scale as the total chip size. This opens a window of opportunities for on-chip antenna co-design and off-chip antenna co-design and compact packaging.

3.2.1 Silicon Losses

Several challenges are present in antenna design for silicon integrated circuits. First, the silicon substrate is quite lossy, with a relative dielectric constant of $e_r = 11.7$. This is substantially high when compared to most highly resistive, superior quality antenna substrates, which have dielectric constants of $\approx e_r < 3.5$. The dielectric constant usually varies with frequency, and has complex components which are associated with the lossiness of the material. Lossiness is related to the conductivity, as it contributes to the signal which is lost as it travels through the lossy substrate to ground [32, 33]. The complex permittivity can be more clearly understood by first examining Maxwell's equation for Ampere's law (taking into account Maxwell's

conception of displacement current as a polarization current). From there, the component of permittivity dealing with loss due to conductivity can be derived using the Ampere-Maxwell Equation:

$$\nabla \times \overline{H} = \overline{J} + \frac{d}{dt}\overline{D} \tag{3.19}$$

If we take the Fourier transform of this equation, we replace $\frac{d}{dt}$ with $j\omega$, and the resulting relation becomes:

$$\nabla \times \overline{H} = \overline{J} + j\omega\epsilon\overline{E} \tag{3.20}$$

In a medium with conductivity σ, the current density $\overline{J}$ is related to $\overline{E}$ by $\overline{J} = \sigma\overline{E}$. Then,

$$\nabla \times \overline{H} = \overline{J} + j\omega\epsilon\overline{E} = \sigma\overline{E} + j\omega\epsilon\overline{E} = (\sigma + j\omega\epsilon)\overline{E} = j\omega(\epsilon - j\frac{\sigma}{\omega}) \tag{3.21}$$

From this point, it is more clear to introduce complex permittivity, ϵ_c:

$$\epsilon_c \equiv \epsilon - j\frac{\sigma}{\omega} = \epsilon(1 - \frac{j\sigma}{\omega\epsilon}) \tag{3.22}$$

where $\frac{\sigma}{\omega\epsilon}$ is called the loss tangent of the material, because it relates directly to the ohmic losses generated by the conductivity of the material. This is related to the dissipation, or loss of energy within the material.

The other element of the complex permittivity ϵ_c deals with the energy storage within the material, and is linearly related to capacitance, $C = \frac{\epsilon A}{d}$. A higher dielectric constant corresponds to higher capacity for the material to store electric charge. As such, a high dielectric constant indicates a material's ability to store charge that might otherwise be radiated, thus corresponding to poor radiation efficiency. A high level of conductivity within a substrate material corresponds to dissipative losses, also contributing to degradation of radiation efficiency.

3.2.2 On-Chip vs. Off-Chip Antennas

Several endeavors in the area of on-chip millimeter-wave antenna design have been undertaken [12]- [23]. In fact, small dipoles and other types of antennas have been placed on-chip and have demonstrated reasonable radiation patterns with the use of a lens; however, this requires radiation through the backplane of the chip, where in normal packaging conditions a ground plane would be located. Also, a substantial amount of radiation is lost through the substrate unless it is significantly thinned, an external lens is used, and the antenna radiates from the back end of the chip [38]. In this particular case of on-chip antennas only, substantial gain can be achieved (+8 dBi is reported), albeit with an uneven radiation pattern.

Essentially, the intrinsic silicon losses and the proximity of the backplane render antenna efficiency too low to reasonably justify placing an antenna on-chip, especially if gains $> 10dB$ are desired. The state-of-the-art on-chip silicon antennas still tends to perform with low efficiency and low gain. The highest measured antenna gains reported are no more than 0 dB for conventional on-silicon antennas. Another key issue in hindering antenna performance (especially bandwidth) is its distance from the ground plane, which cannot be effectively maximized if the antenna is placed on silicon. An investigation into antenna quality factors and efficiencies vs. antenna height from the ground plane will further solidify this argument.

Several loss calculations are involved in microstrip resonators such as microstrip antennas or microstrip transmission lines. In the case of on-chip silicon antennas, the antenna is essentially a form of a microstrip, which contains a top-level radiator, a dielectric substrate (in this particular case, silicon), and a backplane. It is helpful for circuit designers to predict the losses that will be incurred at the antenna terminals as a function of known design parameters such as the characteristic impedance Z_o, substrate thickness h, frequency f_o, and relative permittivity ϵ_r. Various loss contributions for a microstrip resonator can be represented by the antenna Q in the

following equation [39], [40] :

$$Q = \frac{2\pi f_o U}{W} \tag{3.23}$$

Here, U is the stored energy, f_o is the resonant frequency, and W is the average power lost for a 1/4 wavelength microstrip resonator. The total Q (Q_t) is given by equation 3.24:

$$\frac{1}{Q_t} = \frac{1}{Q_c} + \frac{1}{Q_d} + \frac{1}{Q_{rad}} \tag{3.24}$$

where

$$Q_c = \frac{h}{\delta_s} \tag{3.25}$$

Q_c corresponds to conductor losses, where $\delta_s = (\pi f \mu \sigma)^{-\frac{1}{2}}$ is the skin depth of the conductor.

$$Q_d = \frac{1}{tan\delta} \tag{3.26}$$

Q_d corresponds to dielectric losses, where $tan\delta$ is the loss tangent of the substrate material, as described in the previous section.

$$Q_{rad} = \frac{2\pi f_o U}{W_r} \tag{3.27}$$

Q_{rad} corresponds to radiation losses, where W_r is the average power lost due to radiation, and U is the stored energy.

After some calculation, the power radiated from the open end of a microstrip radiator becomes, as defined by [41]:

$$W_r = 240\pi^2 (h/\lambda)^2 F(\epsilon_{eff}) \tag{3.28}$$

where

$$F(\epsilon_{eff}) = \frac{\epsilon_{eff}+1}{\epsilon_{eff}} - \frac{(\epsilon_{eff}-1)^2}{2(\epsilon_{eff})^{3/2}} ln \frac{(\epsilon_{eff})^{1/2}+1}{(\epsilon_{eff})^{1/2}-1} \tag{3.29}$$

Q_{rad} then becomes:

$$Q_{rad} = \frac{Z_o}{480\pi(h/\lambda)^2 F(\epsilon_{eff})} \tag{3.30}$$

Q_{rad} and Q_c are plotted in Figure 3-6. It can be inferred here that, due to the degradation of Q_{rad}, the antenna bandwidth increases with increasing distance from the ground plane. This also makes intuitive sense, since the ground plane terminates field lines in close proximity to microstrip elements (this phenomenon is known as fringing). The closer the ground plane, the stronger the fringing field lines. Q_{cu} increases with frequency since it is proportional to the skin depth, which also increases with increasing frequency.

It is important now to evaluate the antenna loss as a function of its distance from the ground plane, so as to determine whether an on-chip antenna is sensible. Antenna designers typically can express the antenna efficiency (power radiated/power incident) in terms of the quality factors as follows: [39]

$$\eta = \frac{Q}{Q_{rad}} \tag{3.31}$$

This can be expressed as antenna loss in decibels by $10log(\frac{1}{\eta})$. For a simple rectangular patch antenna with dielectric constant = 1 (for simplicity), a graph of antenna loss versus substrate thickness is shown in Figure 3-7.

3.3 Antenna Simulation and Design

Given that the antenna loss significantly decreases with distance from the ground plane, a configuration that maximizes distance from the ground plane was desirable. Whereas an on-chip antenna's radiation would suffer not only the losses through the silicon substrate, but also the conductivity (trapping the antenna's radiation

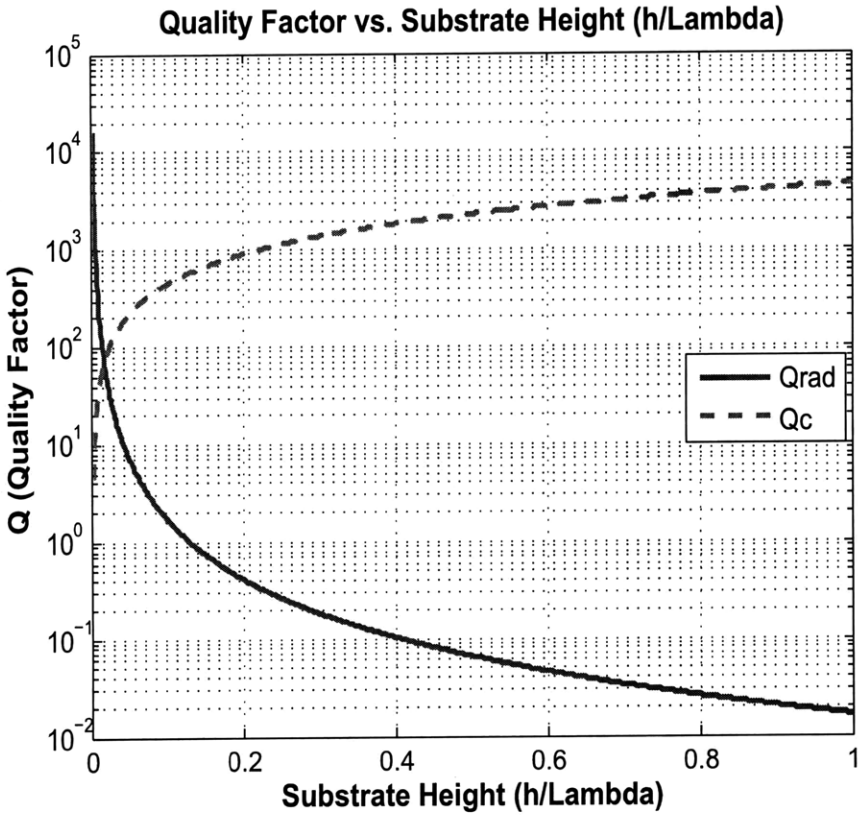

Figure 3-6: *Radiation Quality Factor and Copper Loss Quality Factor vs. Antenna Height from Substrate.*

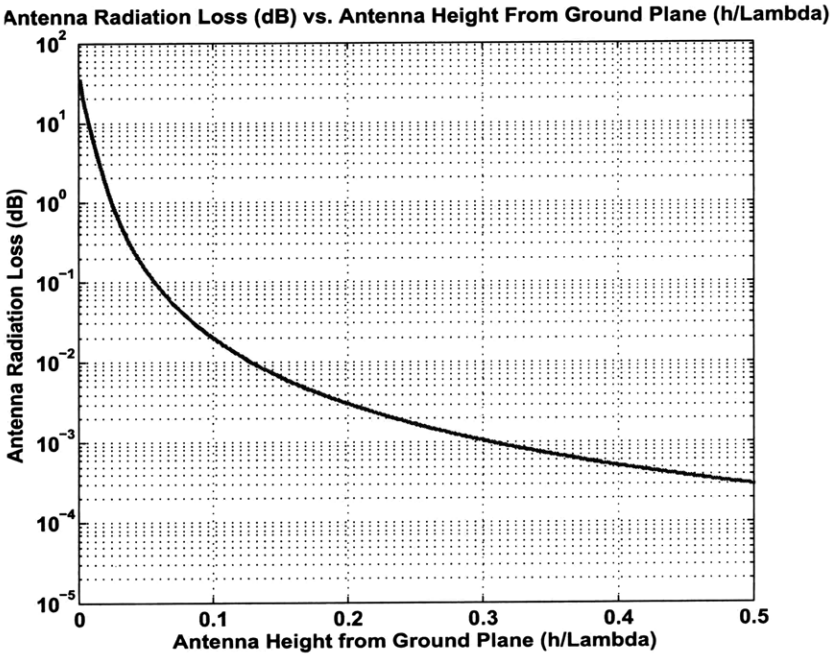

Figure 3-7: *Theoretical antenna loss vs. height (h/lambda) from ground plane.*

within the silicon), the on-chip antenna configuration was not pursued in this thesis. Instead, an antenna was designed to radiate off of the chip edge so as to eliminate on-chip antenna losses and maximize antenna radiation efficiency. Other important requirements were large antenna bandwidth and high directivity.

3.3.1 Design

An antenna configuration enabling the above key features was designed, which was similar to and inspired by an antenna design for 3.1-10.6 GHz Ultra-Wideband [42], a circular dipole, and the Vivaldi Aerial [43]. The antenna was designed for optimal performance within the 77-GHz and 94-GHz frequency regime, while also considering physical packaging constraints such as placement on the edge of a SiGe front end receiver chip. This lead to a Vivaldi-type antenna design that resembled a circular dipole retaining one quadrant of each radiating element. This design enabled direct flip-chip bonding to the input terminals of the front end 77- and 94-GHz imaging receivers.

The Vivaldi Aerial is intuitively well described by Gibson in [43], and the explanation suffices for generally all antennas which incorporate an exponential, elliptical, or circular taper in order to achieve wide bandwidth, such as horn antennas, circular monopoles and circular dipoles. The main mechanism of radiation in these antennas is produced by Hankel Function (or Bessel Function of the 3rd kind) modes produced by travelling waves down the antenna's tapered path. The energy in these travelling waves is tightly bound to the conductors when their spacing is negligible compared to a wavelength. The energy progressively grows weaker as the separation increases, and the energy then becomes coupled to the radiation field. This effect is also noted in [44].

The smallest separation between the two antenna terminals determines the theoretical highest frequency which can propagate, since the waves are tightly bound to the conductors when the separation is very small compared to a wavelength. If the separation is too large, the travelling waves will not be tightly bound to the conductors at the antenna feed, and as such, they will not be guided along the curved edge of

the antenna properly. The maximum separation between the two radiating elements determines the minimum frequency limit of the antenna, because this is the point at which the separation approaches $\lambda/2$ and the travelling waves begin to couple to the radiation field. The antenna must be fed directly at the smallest point of separation so as to properly guide the waves along the curved edge of the antenna. Critical dimensions in this antenna design include both truncation points which define the minimum and maximum separations between the positive and negative terminals of the antenna. The points at which the antenna is truncated are exactly at the x- and y- radii of each ellipse. Figures 3-8, 3-9, and 3-10 should help illustrate this method. This design was carried out in CST Microwave Studio software.

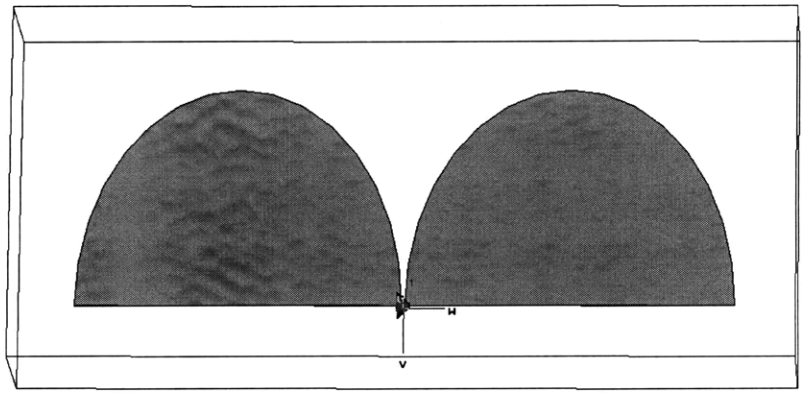

Figure 3-8: *Truncation of Antenna Ellipses at y-radius.*

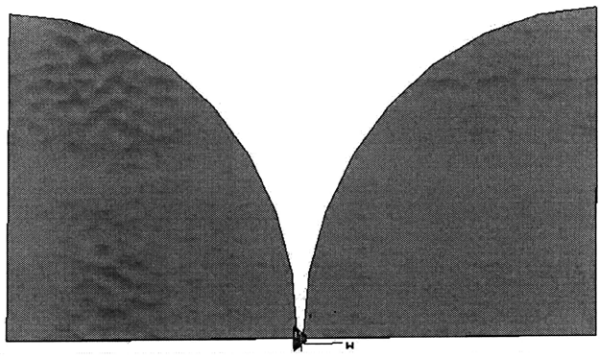

Figure 3-9: *Truncation of Antenna Ellipses at x-radius*

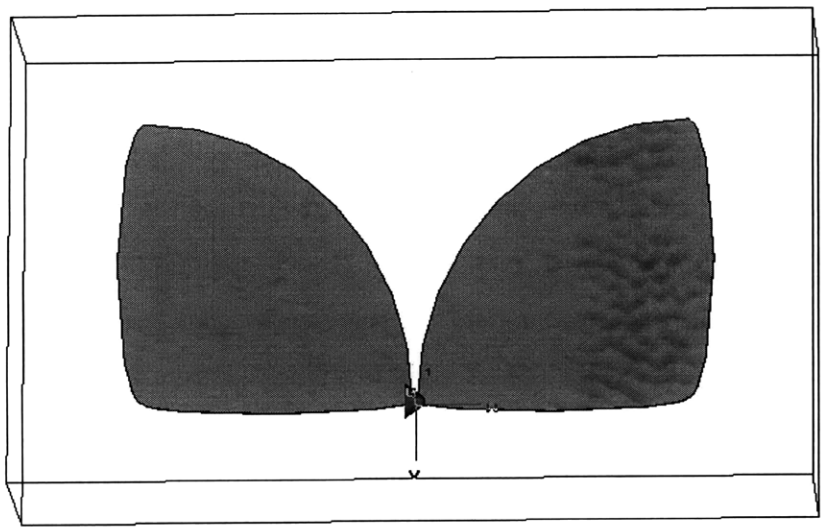

Figure 3-10: *Addition of curvature for smoother radiation pattern.*

The primary mathematical function defining the antenna design in this thesis does not fit to an exponential curve; rather, it is elliptical (as described above), with a semi-major radius of 1200μm and a semi-minor radius of 1000μm. This ellipse is defined mathematically as the following:

$$\frac{(x-h)^2}{a^2} + \frac{(y-k)^2}{b^2} = 1 \tag{3.32}$$

where a and b are the semi-major and semi-minor axes, respectively, and the ellipse is centered at (h, k). The ellipse then can take on the following expression to be plotted mathematically:

$$y = .833 * \sqrt{-x^2 + 2400x} \tag{3.33}$$

The physical values were chosen such that the maximum separation between the two antenna elements was well beyond $\lambda/2$ at 90 GHz, and approximately $\lambda/2$ at 70 GHz. The wavelength at 70 GHz is $\approx 4.2mm$, requiring the maximum separation to be $\approx$2mm. This fixed the x-radius value. The y-radius value was made slightly longer for improved impedance bandwidth, as it provided a slightly smoother wave guidance

along the curves of the conductors. An ultra-thin, low-loss dielectric material was chosen for the antenna backing, and to provide mechanical stability. This material has a relative permittivity of ≈3.5, with $tan\delta \approx .0037$, and is commercially available from Rogers Corporation, RO4350B. The data sheet can be found from [45].

3.3.2 Simulation

The antenna was simulated in CST Microwave Studio software using a dielectric thickness of 0.004", or 100 μm, with the design described above. All loss values for RO4350B material were incorporated in the simulation dielectric model file. The antenna was excited directly at the area of smallest separation, so as to enable initial close coupling to the antenna conductors.

The simulation yielded a center frequency of 95.5 GHz with approximately 9.5-10.5 dBi of gain from 90-100 GHz, respectively, and achieving VSWR < 2 from 83 GHz and beyond, through the simulated limit of 200 GHz. Figures 3-11 - 3-13 illustrate the simulated S11 and the three-dimensional radiation patterns at 90 GHz and 100 GHz. It is clearly important to understand how the antenna is oriented for these particular radiation patterns. For this design, the antenna exhibits maximum radiation at approximately 45 degrees. Figure 3-14 illustrates the precise orientation of the antenna as it achieves the radiation patterns of Figures 3-12 and 3-13, indicating that the maximum radiation occurs in the upper-right quadrant of the 3-dimensional antenna space.

3.4 Antenna Fabrication

The antenna design was fabricated at MIT in the Exploratory Materials Laboratory (EML). Several iterations were required before the process was finalized. This antenna was to be fabricated on .004", or 100 μm, thick Rogers 4350B dielectric material. The first iteration of processing utilized this Rogers material with 1 oz volume of copper deposited on 0.004", or 100 μm, thick dielectric material, single-sided. The thickness of the copper on a 9" x 11" sheet of test material was approximately 37 μm. Since the

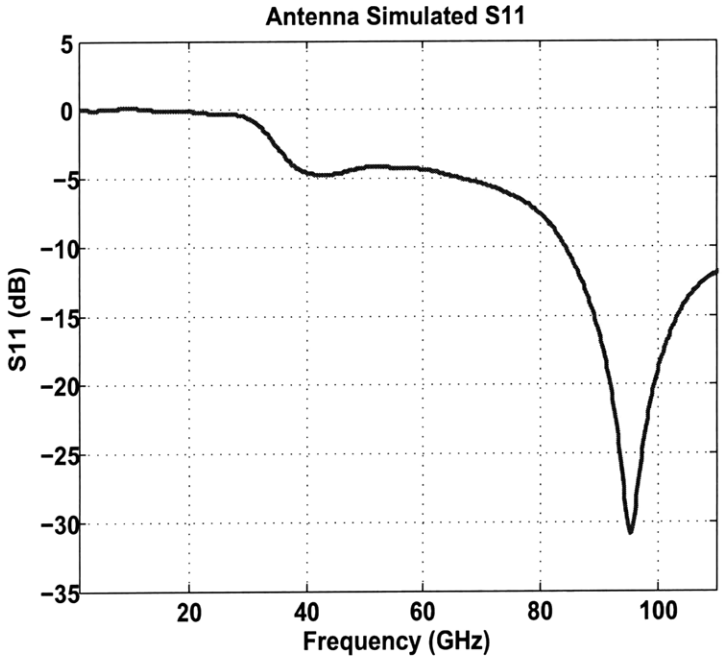

Figure 3-11: *Antenna Simulated S11*

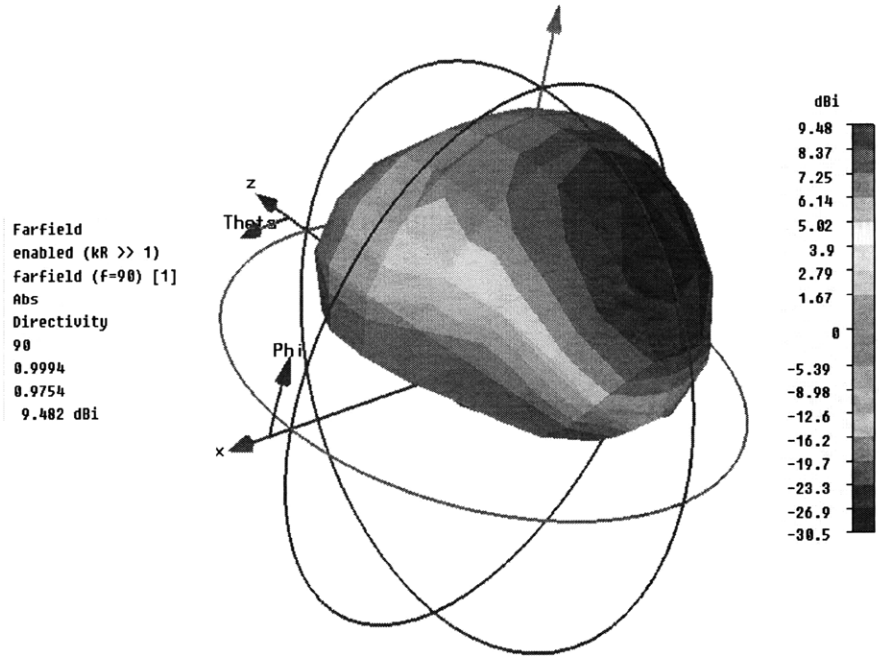

Figure 3-12: *Simulated 3D radiation pattern at 90 GHz.*

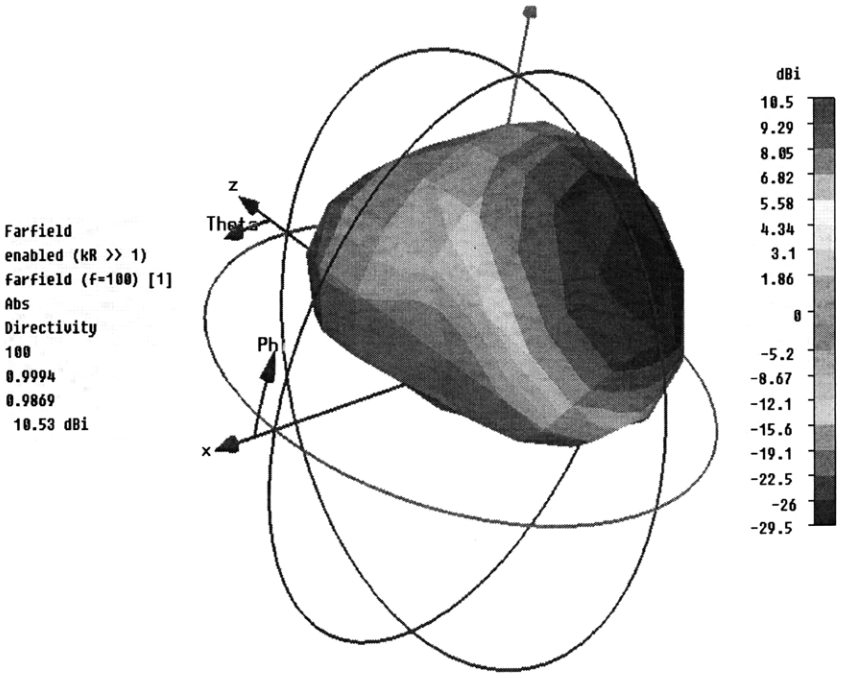

Figure 3-13: *Simulated 3D radiation pattern at 100 GHz.*

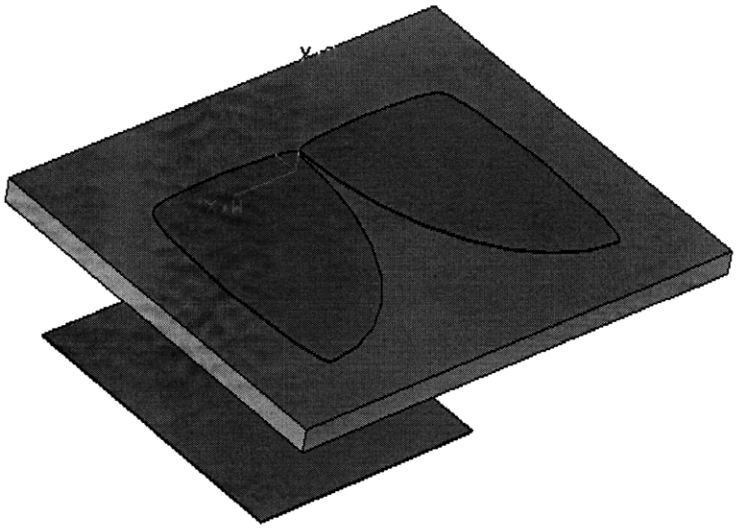

Figure 3-14: *Orientation of the antenna as it achieves the simulated 3-dimensional radiation patterns illustrated in Figures 3-12 and 3-13.*

main feature size was 20 μm, coupled with the fact that wet etch spreads laterally twice as fast as it does vertically, this spawned concern that the copper deposited on the Rogers 4350B test material was possibly too thick to etch reliably. The next reasonable alternative would require sputtering of a much thinner layer of copper onto the Rogers dielectric material. Each step of the antenna fabrication will be detailed in the following sections, including the processing of the chrome mask, the copper processing from lithography to exposure, wet etch and sputter.

3.4.1 Chrome Mask

The first step in the antenna processing was to expose the antenna pattern on a chrome plate using the MTL Heidelburg tool. This tool takes an input .dxf drawing file of the desired design. In this case, the .dxf drawing file was the antenna design exported from the CST Microwave Studio simulator. Next, a plate of glass and chrome with a layer of photoresist was exposed to light, shielded by the .dxf mask (similar to light shielding provided by a negative in photo processing) for a specified amount of time. The chrome plate was then shielded from light and brought to the EML lab. The chrome mask processing on the Heidelberg tool was performed by Dennis Ward.

The chrome mask was processed by developing the photoresist on the chrome on glass plate under longer wavelength light, as shorter $\approx$400nm wavelengths break down the photoresist rendering it soluble in developer. In this case, a water-based organic TMAH product called AZ 917 was used. Once the photoresist was patterned, the chrome was dissolved in an acid called CR-7 in the areas where the resist was removed, until it became transparent.

After processing, only a glass plate was left with the arrayed antenna pattern in chrome. A photo of the chrome mask is shown in Figure 3-15.

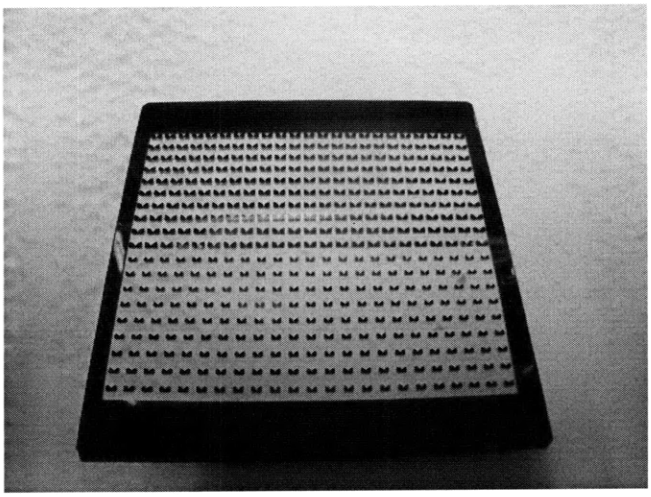

Figure 3-15: *Chrome Mask Fabricated on MIT's Heidelburg Tool.*

3.4.2 Copper Processing

The copper processing involves photolithography, whereby light sensitive photoresist is spun onto copper discs, which are then exposed to broadband light through the chrome mask containing the antenna patterns. The pattern of antennas shaped by the photoresist is created by shielding the desired patterns and exposing the rest of the area to light. (In the case of negative photoresist, the opposite is true.) The photoresist undergoes a chemical reaction when exposed to light which causes it to break down and dissolve away when developed, leaving only the desired pattern.

The processing involved for the antennas in this thesis involved first cutting the Rogers 4350B material into 3.5" discs, cleaning thoroughly with isporopyl alcohol and drying with an air gun, blowing from the center in order to limit standing waves. The discs were then baked 5-10 minutes at 150° C to dry fully.

Afterwards, the discs were taken to a coater machine to spin photoresist onto each disc, as shown in Figures 3-16 and 3-17. AZ 4260 positive photoresist was spun at 3000 rpm for 1 minute for each disc. Each disc was then pre-baked on a hot plate at 105° C with the center held down so as to distribute heat throughout the entire area of the disc, as shown in Figure 3-18. Afterwards, the coater was cleaned with acetone.

The discs were then brought to the MJB3 broadband exposer, shown in Figure

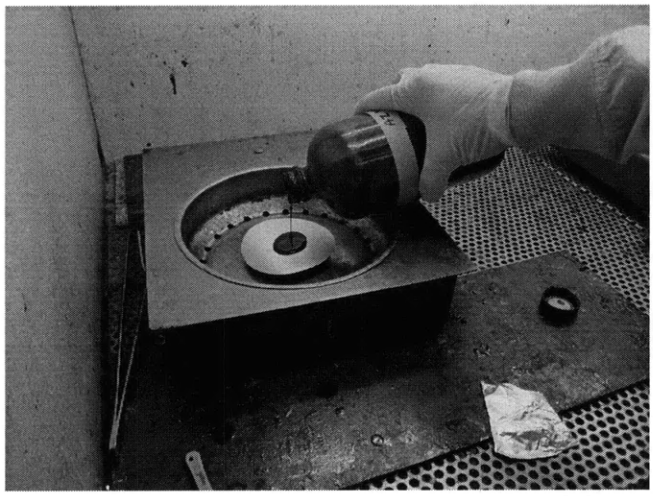

Figure 3-16: *Copper Disc on Photoresist Coater.*

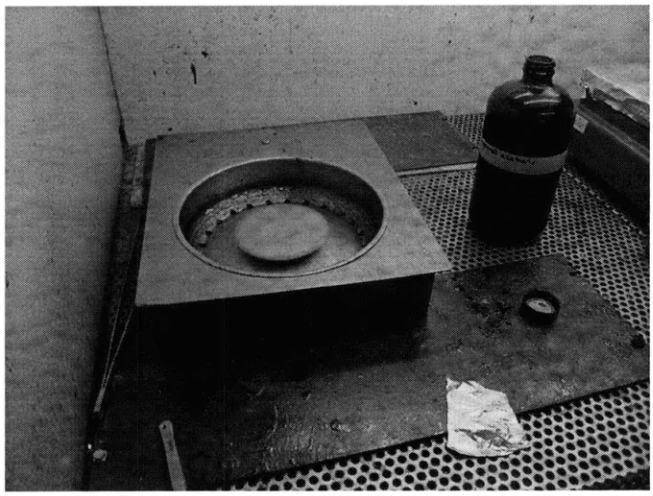

Figure 3-17: *Copper Disc Spinning on Photoresist Coater.*

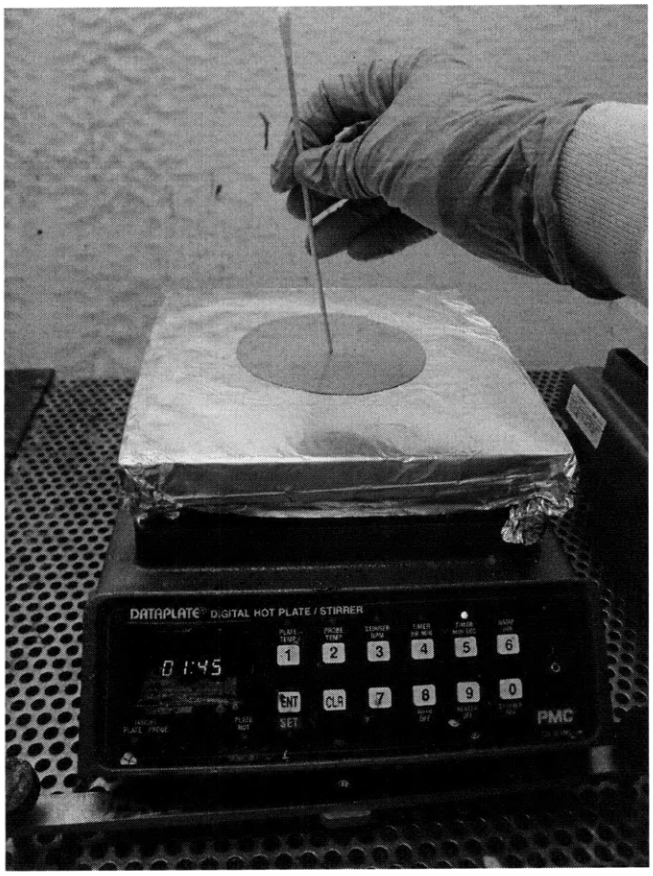

Figure 3-18: *Copper Disc Pre-Exposure Bake.*

3-19, where the chrome mask was attached by vacuum to the top plate and put in direct contact with each disc. The photomask was exposed to uniform light which shone through the it, blocking light in the areas of the antenna shapes and exposing the rest of the area. The discs were exposed by soft contact three times at 20 seconds per exposure, waiting an additional 20 seconds in between exposures for cooling and thermal management.

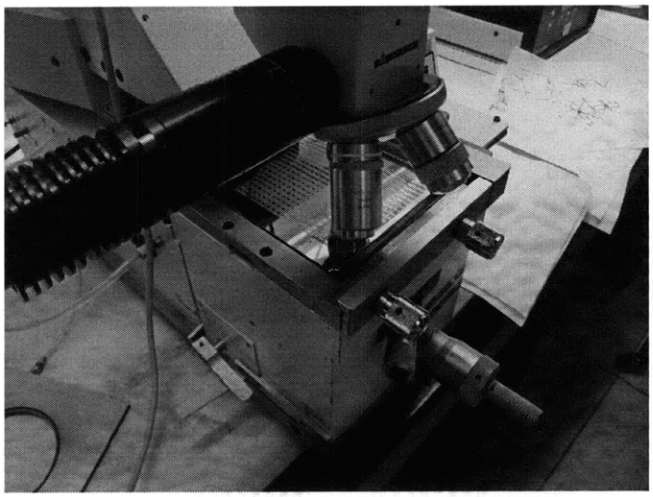

Figure 3-19: *MJB3 Broadband Exposer.*

Following the exposure, the discs were developed with AZ 440 MIF developer until the exposed photoresist was visibly removed. This required approximately two minutes of agitation to fully develop. After developing, the discs were again rinsed with water and dried from the center out, followed by a post-exposure bake of 105° C on the hot plate at 3 minutes each. The final result of the photolithography processing on the copper discs is shown in Figure 3-20, which illustrates the antenna patterns in photoresist surrounded by copper.

3.4.3 Wet Etch

Once the discs had been through photolithography, they were ready for wet etch. This is a process in which the copper is etched off of the discs and the elements shielded by photoresist theoretically remain intact below the photoresist.

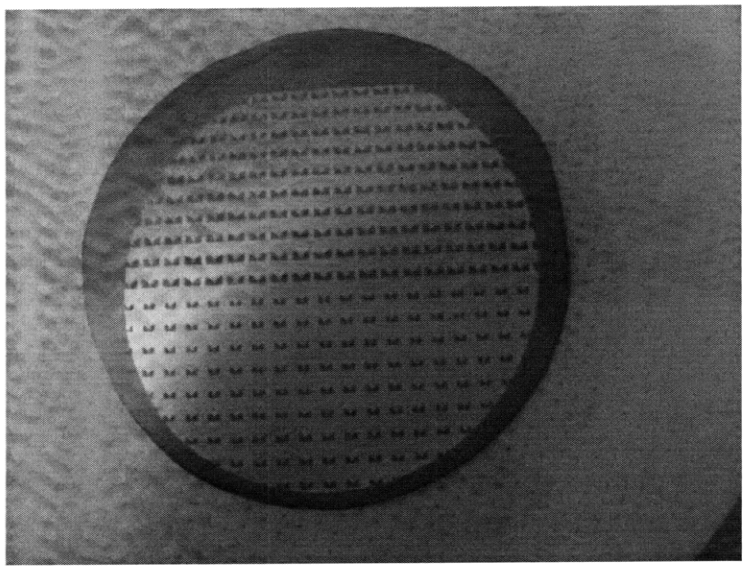

Figure 3-20: *Copper Disc After Broadband Exposure and Photoresist Development.*

The discs were placed in a 5:1 Nitric acid (HNO_3):water solution. After several samples were taken, it was determined that approximately 20 seconds was sufficient to etch a total copper thickness of approximately 37 μm, etching at a rate of approximately 1.5 μm per second (as determined on the high-power microscope post-etch). However, this etch was highly insufficient, as it undercut the copper under the photoresist so much that the spacing between the two antenna elements became substantially large and ineffective.

Next, a thinner sheet of single-sided copper on Rogers 4350B material was ordered from Rogers. $\frac{1}{2}$ oz. copper was deposited (previously 1 oz was deposited), providing $\frac{1}{2}$ the thickness from the prior experiment: $\approx 18\mu$m. The wet etch underwent the same iterative process, yet the copper was still too thick to provide a sufficient etch with thin enough spacing between the two antenna elements. For sufficient impedance matching, the minimum spacing was required to be 20μm. Figure 3-21 shows the improved, albeit still unacceptable etch for the thinner copper material. The upper layer in this photo is the remaining photoresist, which illustrates where the copper should have been. The underlying copper, clearly seen, was etched considerably far away from the photoresist boundary.

Given that Rogers did not provide 4350B material with thinner copper material,

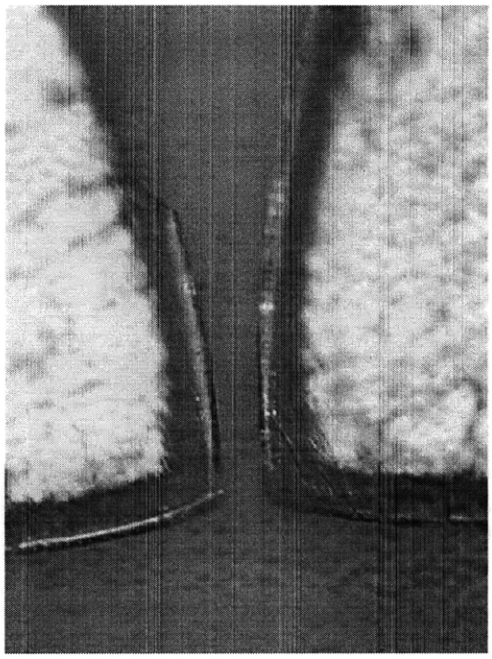

Figure 3-21: *Antenna post-wet etch with 1/2 oz. copper deposit RO4350B material, illustrating significant undercut from etch.*

the only reasonable alternative to obtain a sufficient etch involved copper sputtering onto blank RO4350B dielectric material, which is described in the following section.

3.4.4 Sputtering

Sputtering is a process which involves bombardment of a target material by energized ions, which results in ejected atoms depositing onto thin films. The sputtering tool used at MIT's EML is shown in Figure 3-22. The energized argon particles primarily responsible for the sputtering process are supplied by a very hot plasma. The incoming ions create collisions heavy enough to eject atoms from the target (in this case, copper), which then bind onto the material below the target. The copper target is illustrated in Figure 3-23, and the dielectric discs in the sputtering tool to be deposited on are shown in Figure 3-24.

Sputtering is a relatively linear process; the longer a material is left in the sputtering machine, the more copper is deposited onto the material. For the particular case of this project, no more than .5 μm of copper thickness was necessary. In fact,

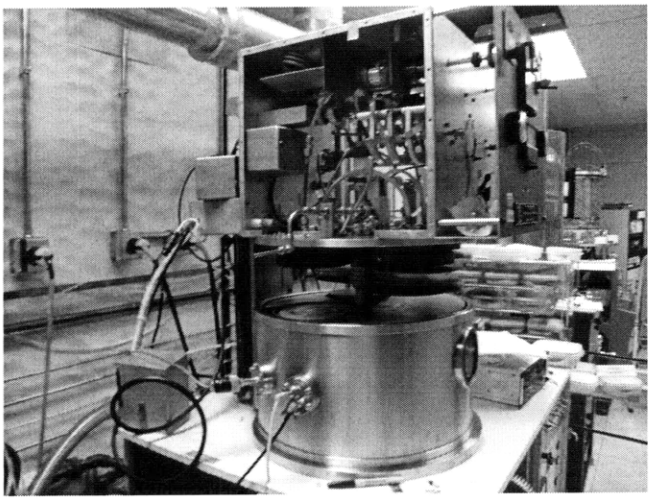

Figure 3-22: *EML Sputter Tool*

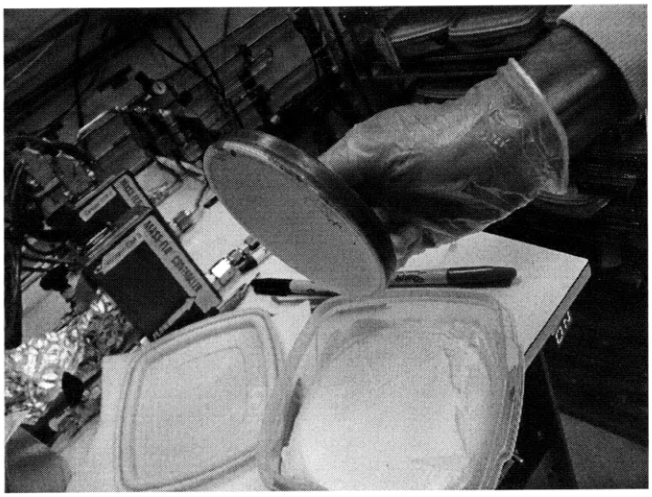

Figure 3-23: *Copper Target for Sputter Tool*

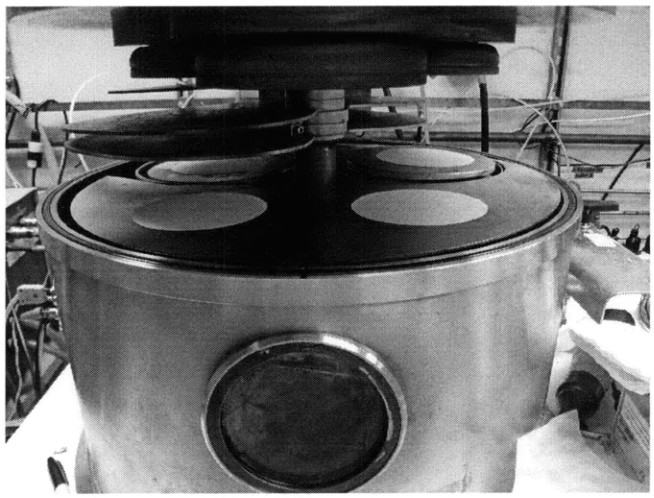

Figure 3-24: *EML Sputter Tool with Dielectric Discs*

the thinner copper ensured a more reliable wet etch. Given the measured sputtering capability of this machine, $\approx$ 18 minutes per disc was necessary for a sufficient amount of Cu sputtering.

Figure 3-25 illustrates the discs after sputtering and lithography processing. Unfortunately they became oxidized and turned mostly black, most likely as a result of insufficient cooling in the sputter machine. However, each disc remained conductive with 0.1Ω of resistance when measured with an Ohmmeter from end to end, rendering them electrically viable.

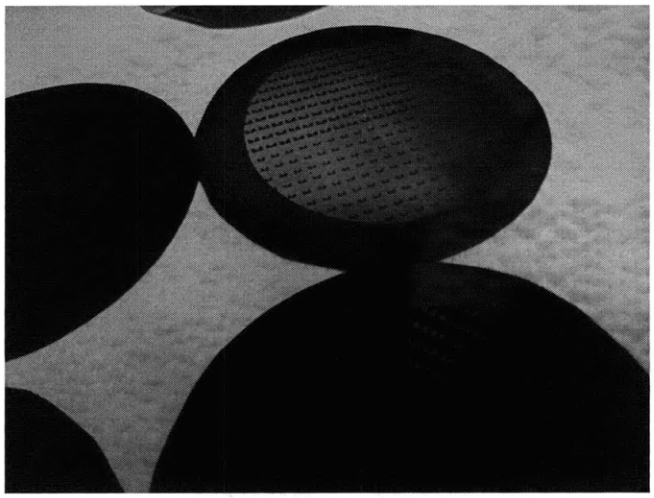

Figure 3-25: *Copper Discs Post Sputter*

The copper processing after sputtering was the same as described above, and the wet etch was significantly more successful. With the same concentration of HNO_3, only ≈2 seconds of etching was required. Figure 3-26 illustrates the results of the wet etch after processing the discs with sputter-deposited Cu.

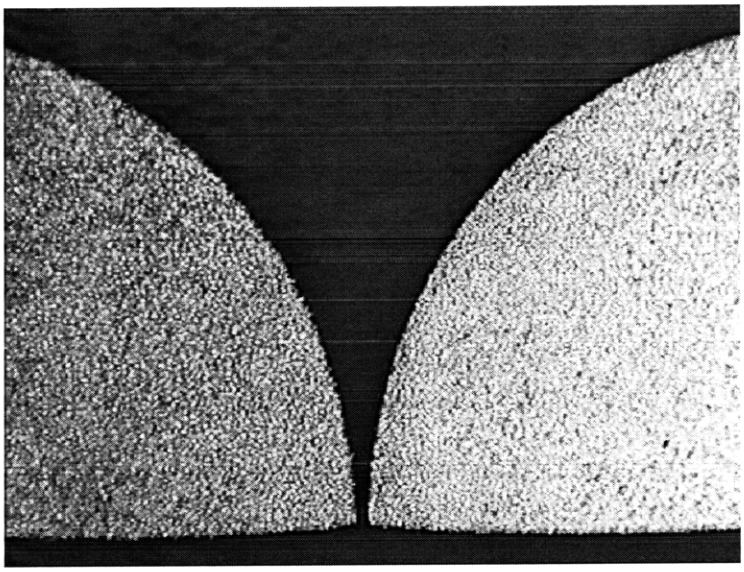

Figure 3-26: *Antenna after processing with Cu sputter-deposited material.*

3.4.5 Copper Polishing

The final step in the antenna fabrication process was the removal of the protective photoresist. Figure 3-27 illustrates quite clearly a highly magnified antenna with the photoresist layer still intact after the Cu wet etch. This is easily removed with acetone, while leaving the underlying copper unharmed. In this case, it was important to use caution in the photoresist stripper choice, because most photoresist strippers do attack Cu. Since the processing of these antennas did not involve a high temperature bake or a high energy plasma, the acetone proved effective at stripping the photoresist. Otherwise, it would not have been strong enough to remove the photoresist and more aggressive photoresist stripping solutions such as NMP or Dimethyl Sulfonate would have been necessary. Figure 3-28 illustrates the final Cu antenna with the photoresist stripped.

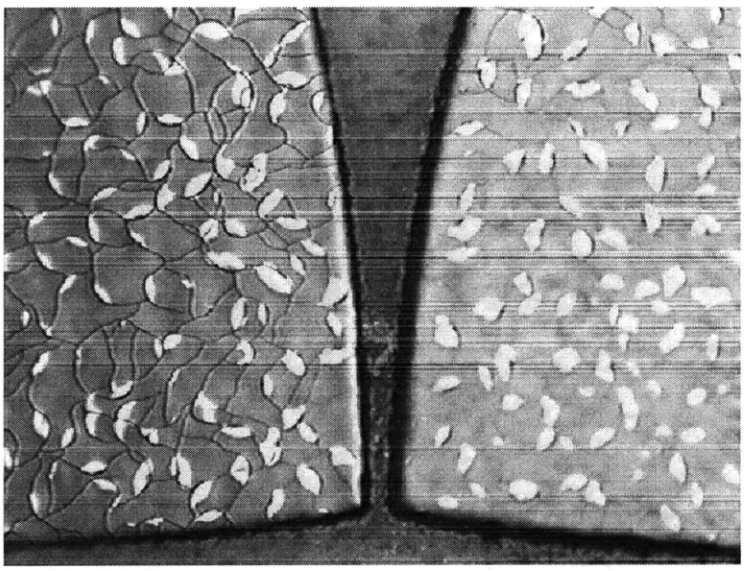

Figure 3-27: *Highly magnified antenna illustrating photoresist layer still intact after wet etch.*

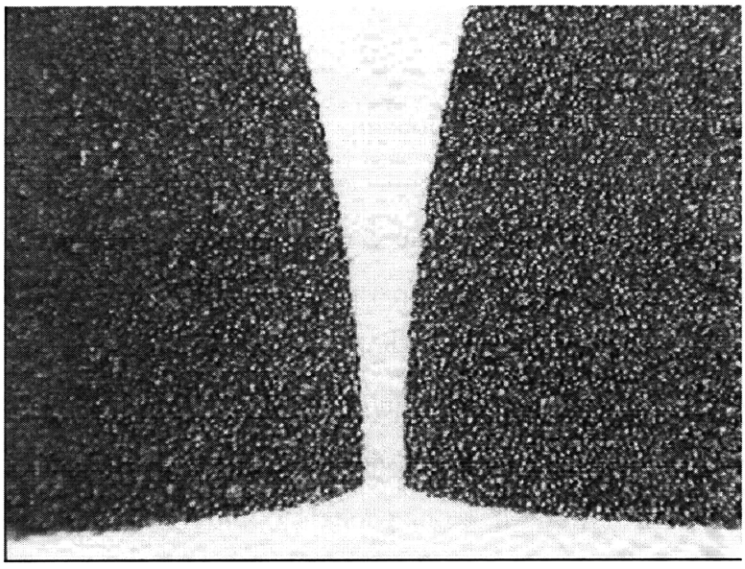

Figure 3-28: *Final copper antenna with photoresist removed.*

3.5 Antenna Testing and Characterization

Antennas are typically characterized in an anechoic chamber with a standard gain horn antenna as a reference. This has typically been done because antennas have to be characterized while operating in the far-field regime, or $\approx 10\lambda$ apart. Traditionally, antennas have operated at much lower frequencies and a large chamber was required to achieve their far-field distance. However, for millimeter-wavelength frequencies, far-field operation occurs only centimeters away. Therefore, millimeter-wave antennas can be characterized more conveniently at a probe station with GSG probes, using identical antennas facing each other at the transmit and receive end.

The Return Loss measurement of each antenna is straightforward, and can be measured by the S_{11} parameter, or reflection coefficient, of the antenna. This, and all other S-parameter measurements, are taken on the Agilent E8361A Vector Network Analyzer (VNA). The VNA is operable from 10MHz-67 GHz, but extended frequency operation is enabled with the use of an external source module which mixes the operable frequency up to 110-GHz. This waveguide transmit/receive source module then connects to GSG probes through 1.0mm test ports.

The gain of each antenna can be extrapolated using the Friis Transmission Formula, provided that the power transmitted P_t and power received P_r are known, because $G_t = G_r$:

$$Friis\ \ Transmission\ \ Formula: \quad \frac{P_r}{P_t} = G_t G_r \left(\frac{\lambda}{4\pi R}\right)^2 \tag{3.34}$$

The ratio $\frac{P_r}{P_t}$ can be measured by the coupling S_{21} between them. Since the gain of both antennas are identical, the gain equation becomes:

$$G^2 = \frac{P_r}{P_t}\left(\frac{4\pi R}{\lambda}\right)^2 \tag{3.35}$$

where R is the distance between the two antennas ($R \approx> 10\lambda$), and λ is the free-space wavelength. Both GSG probes are properly calibrated to account for any loss incurred up to the probe tips. The S_{21} coupling is measured on the Agilent Vector

Network Analyzer. Careful and consistent measurement of the distance enables an accurate measurement of the antenna gain parameter.

Calibration is achieved using Cascade Microtech WinCal software, where the calibration selected is an LRRM Port 1 match. A standard Cascade Microtech W-Band Impedance Standard Substrate is used as a standard for 50-ohm load, short, and thru measurements. It is imperative to acquire an accurate calibration in order to achieve trustworthy results. Ideally, a VNA calibration should not be in error by more than ± 0.5 dB. This error can be computed by the WinCal software, and is an accurate method for determining whether or not a calibration is valid. Figure 3-29 shows the calibration results for the measured antenna results presented in this section.

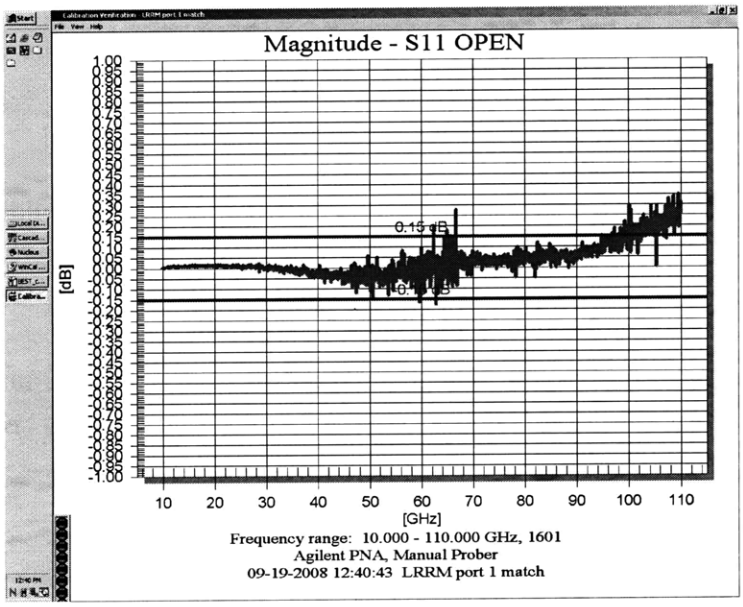

Figure 3-29: *WinCal calculation of VNA calibration error.*

Figure 3-30 shows a conceptual picture of the test setup, illustrating the GSG probes, millimeter-wave cable connectors, and distance R.

Here, the azimuth plane can be measured relatively easily by letting one antenna/probe remain stationary, and rotating the second one. Several limitations exist within the probe station setup, including chuck height and microscope range, but a reasonable and sufficient measurement can be made within these parameters. In this particular case, the stationary antenna was set up in one of two fixed positions

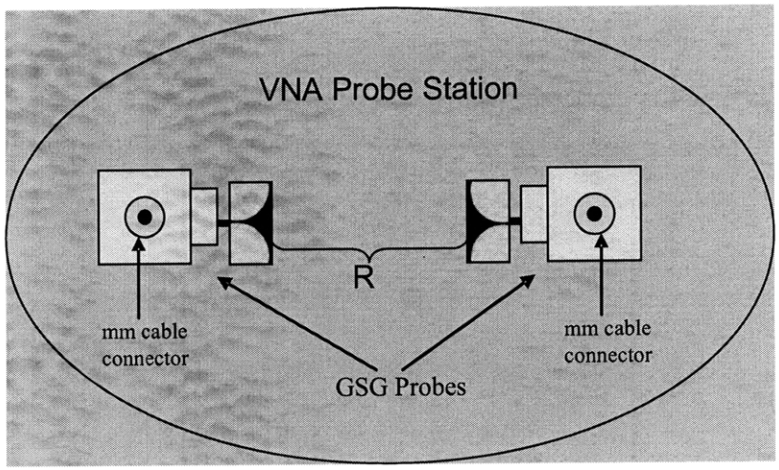

Figure 3-30: *Conceptual antenna gain test setup.*

along a 180° line, while the second antenna was measured at several positions along a parallel line, ultimately making a square, as shown in Figure 3-31. The "stationary" antenna took positions 1 and 2, while the second antenna was moved from positions a-f, which were approximately equidistant. All changes in R were taken into account in the final calculation of antenna gain. The measurement from Antenna 1:Position 1 to Antenna 2:Position f, for example, would correspond to angle $\phi = 90°$. Antenna 1:Position 2 to Antenna 2:Position a would correspond to angle $\phi = 0°$. For all measurements, the antennas maintained the same tilt angle.

The elevation measurement was more difficult to obtain, given the sensitivity of the measurement setup and the necessity to move the receiving antenna position vertically. This was done using small styrofoam blocks stacked in vertical steps, such that by the last step, the receive antenna would be approximately above the transmit antenna (corresponding to $\theta = 0°$. The measurement setup for the elevation radiation pattern is shown in Figure 3-32.

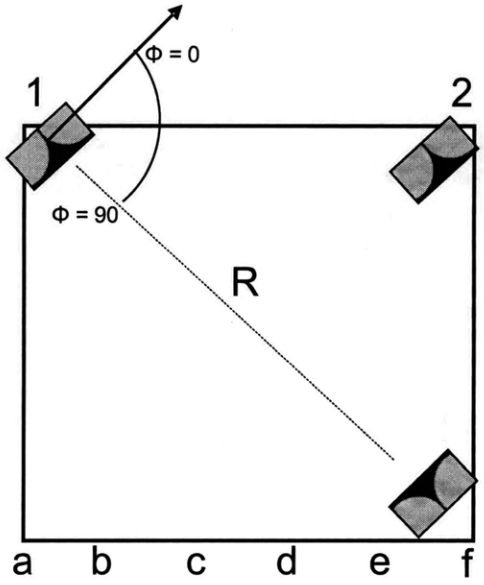

Figure 3-31: *Antenna Orientation for Azimuth plane measurement*

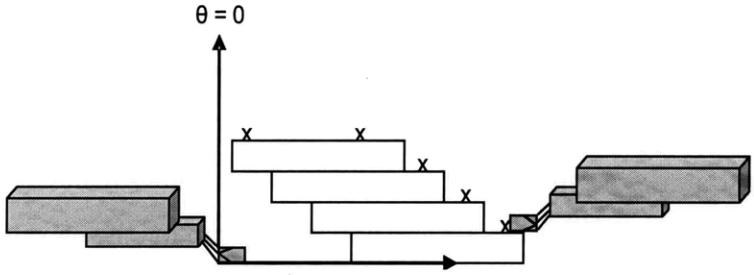

Figure 3-32: *Antenna Orientation for Elevation plane measurement*

3.6 Antenna Results

The measured antenna results were quite close to numerical simulation, albeit approximately 7.5% lower in center frequency. Namely, the simulation yielded a center frequency of 95 GHz, while the measurement yielded a center frequency of 88 GHz. There are several factors that could explain the discrepancy in center frequency, including higher dielectric values in the antenna substrate at MMW frequencies, and anomalies in the fabrication process. However, the antenna retained its simulated wideband characteristic. Namely, the antenna achieved $VSWR < 2$ from $\approx$ 73 GHz-100 GHz when the antenna had sufficient spacing from the ground plane ($\geq$ $0.5mm$). Also, the antenna more clearly exhibited an endfire radiation pattern in the upper quadrant ($\theta = 0-90°$) with increased spacing from the ground plane. As the antenna was placed more closely to the ground plane ($\leq$ $0.1mm$), the impedance bandwidth decreased.

Figure 4-12 illustrates the measured vs. simulated S11. Figures 3-34 - 3-37 illustrate the 2-dimensional radiation pattern polar plots of the antenna for the elevation and azimuth planes at 90 GHz and 100 GHz, with measured vs. simulated results. For the elevation measurements in Figures 3-34 and 3-36, the measurement was only taken in the upper quadrant ($\theta = 0 - 90°$). The radiation pattern was maximum in this particular quadrant, and the measurement setup did not allow for measurement much further beyond the $\theta = 0-90°$ limit due to the limited range of the GSG probes and also the probe locations, which would have impacted the radiation pattern. It can be seen quite clearly that the simulated radiation pattern matches the measured values quite well in the quadrant of interest, with discrepancies at 0° and 90°. The main reason for the discrepancy at $\theta = 90°$ is the simulation setup, which incorporates a perfect electric boundary at $\theta = 90°$, thus theoretically shorting all radiation fields to ground at the boundary. In the measurement setup, there is no theoretical perfect electric boundary. Also, each antenna was placed on a thin layer of styrofoam on top of the metal chuck, which enabled radiation between the transmit/receive antennas at the $\theta = 90°$ boundary. At the $\theta = 0°$ boundary, the observed trend was that

the coupling between the two antennas certainly decreased as they became closer to a vertically parallel orientation. This trend matches that which is indicated in the simulated results. Figures 3-35 and 3-37 indicate good agreement between simulated and measured results, albeit with higher measured gain. (It should be noted that Figure 3-35 illustrates the normalized measured gain on the simulated plot, so as to highlight more clearly the fact that the radiation patterns are in agreement). This discrepancy is sensible, however, given that the simulation indicated a higher center frequency than that which was measured. In this case, slightly higher measured gain would be expected.

Figures 3-38- 3-45 illustrate the antenna gain vs. azimuth and elevation angles for selected frequencies from 73 GHz through 105 GHz. Figures 3-46 and 3-47 illustrate the antenna gain vs. frequency for the Azimuth and Elevation planes, respectively. Full characterization results for gain vs. frequency and gain vs. angle for both the Azimuth plane and the Elevation plane are included in Appendices A-C.

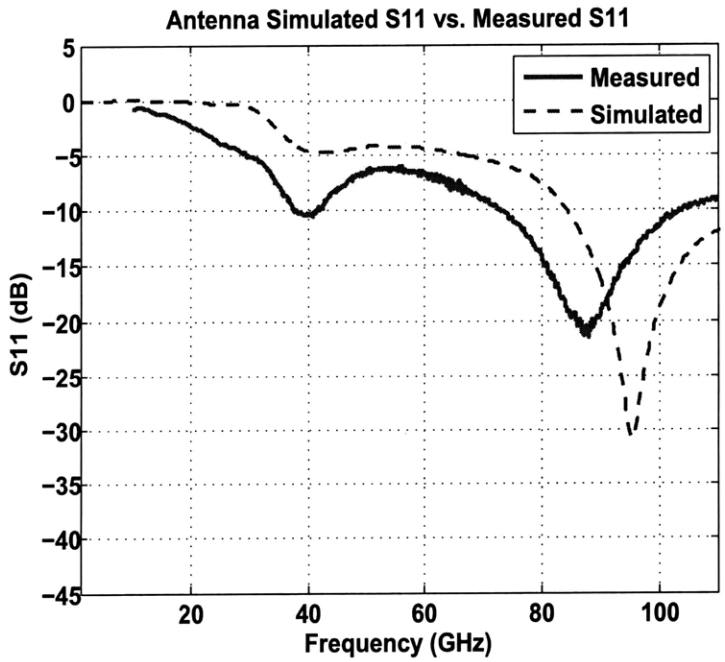

Figure 3-33: *Antenna Simulated S11 vs. Measured S11*

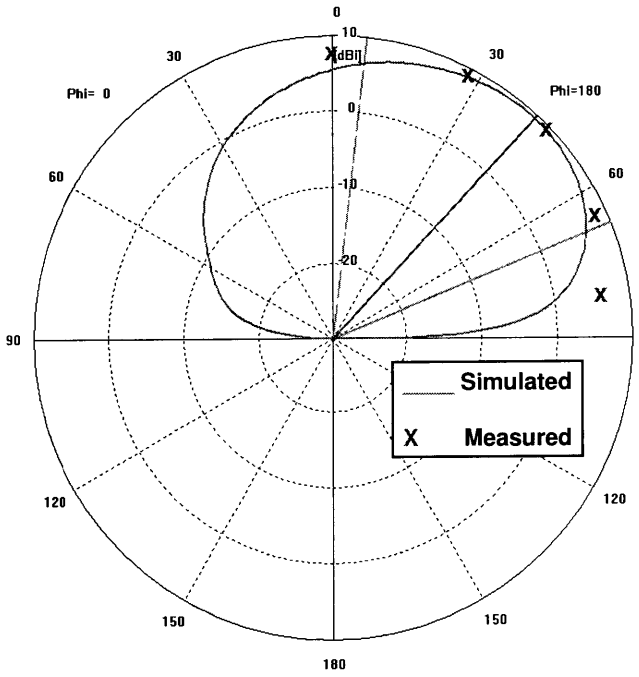

Figure 3-34: *Antenna Simulated Gain vs. Normalized Measured Gain. Frequency = 91 GHz, varying angle* Θ *(Elevation plane).*

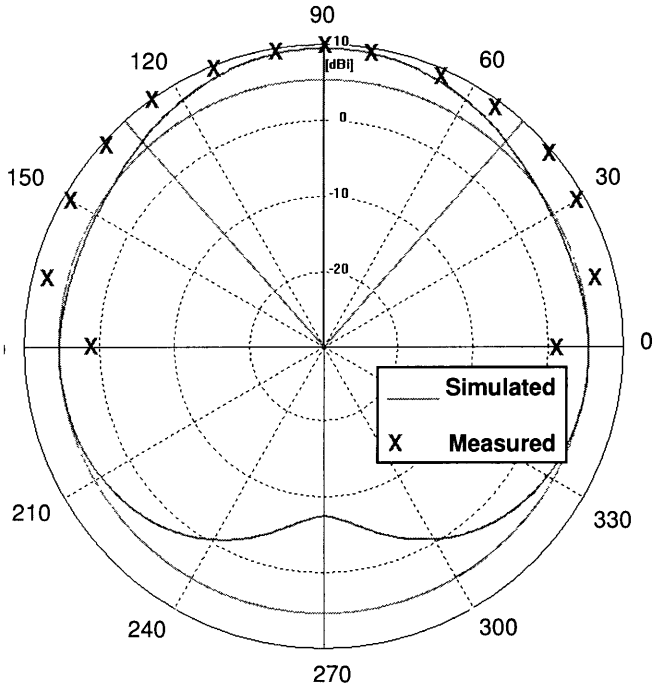

Figure 3-35: *Antenna Simulated Gain vs. Normalized Measured Gain. Frequency = 91 GHz, varying angle* Φ *(Azimuth plane).*

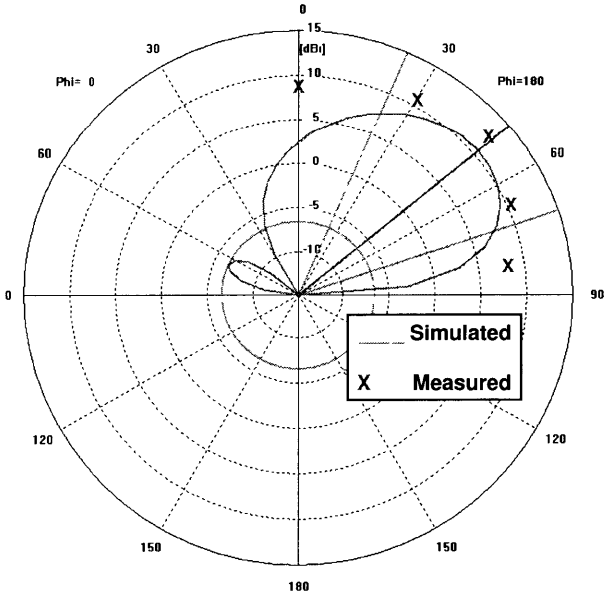

Figure 3-36: *Antenna Simulated Gain vs. Measured Gain. Frequency = 100 GHz, varying angle* Θ *(Elevation plane).*

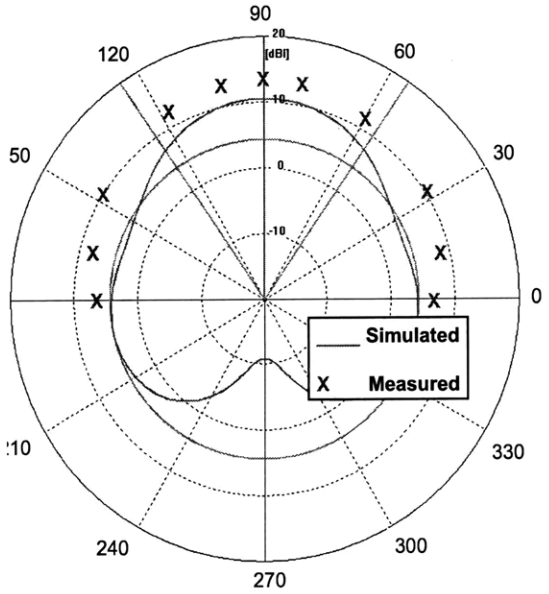

Figure 3-37: *Antenna Simulated Gain vs. Measured Gain. Frequency = 100 GHz, varying angle* Φ *(Azimuth plane).*

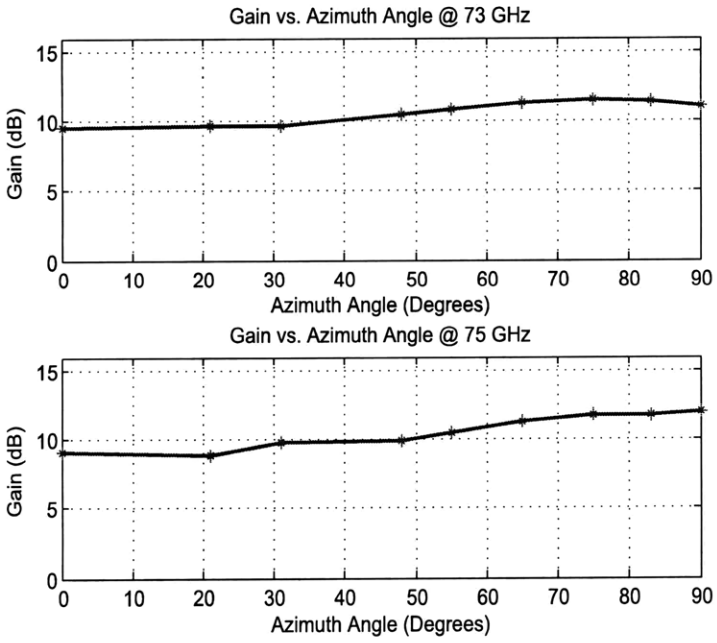

Figure 3-38: *Measured Antenna Gain vs. Angle: 73 GHz and 75 GHz, Azimuth Plane.*

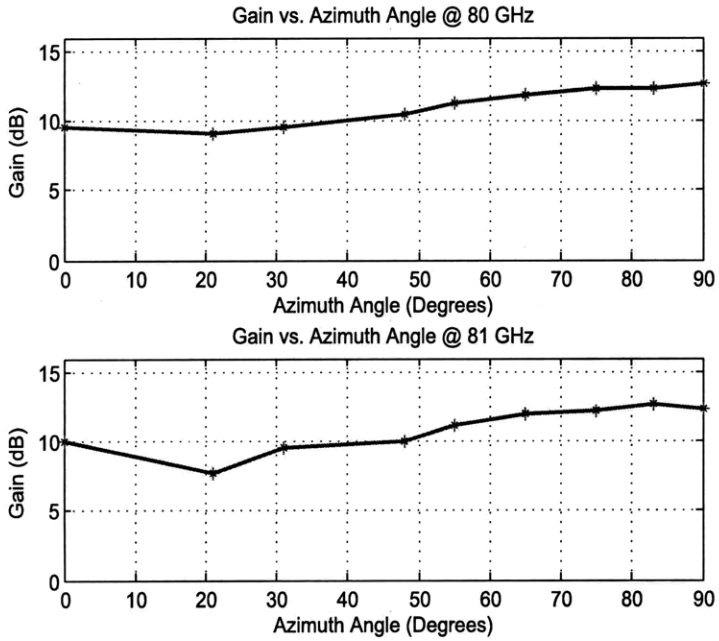

Figure 3-39: *Measured Antenna Gain vs. Angle: 80 GHz and 81 GHz, Azimuth Plane.*

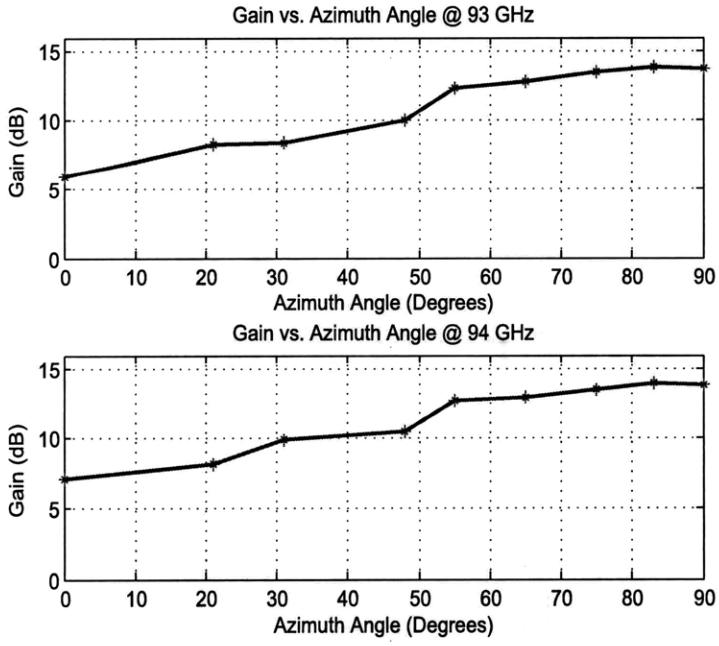

Figure 3-40: *Measured Antenna Gain vs. Angle: 93 GHz and 94 GHz, Azimuth Plane.*

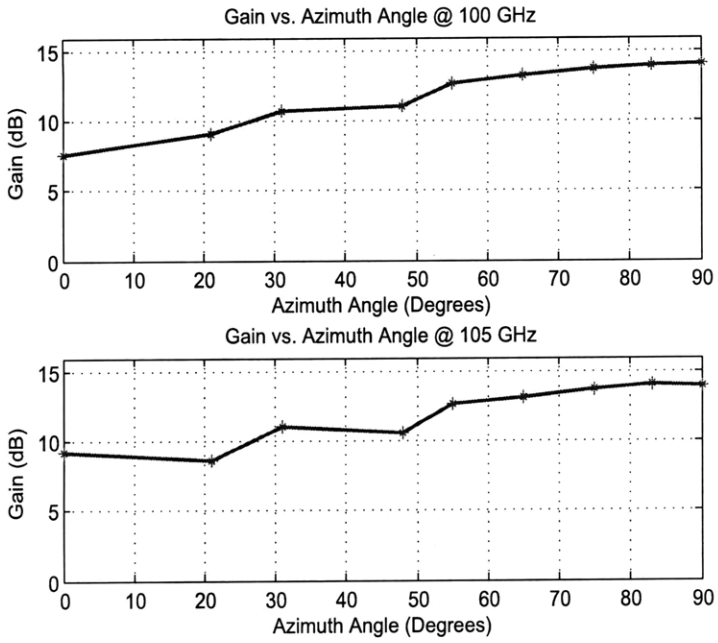

Figure 3-41: *Measured Antenna Gain vs. Angle: 100 GHz and 105 GHz, Azimuth Plane.*

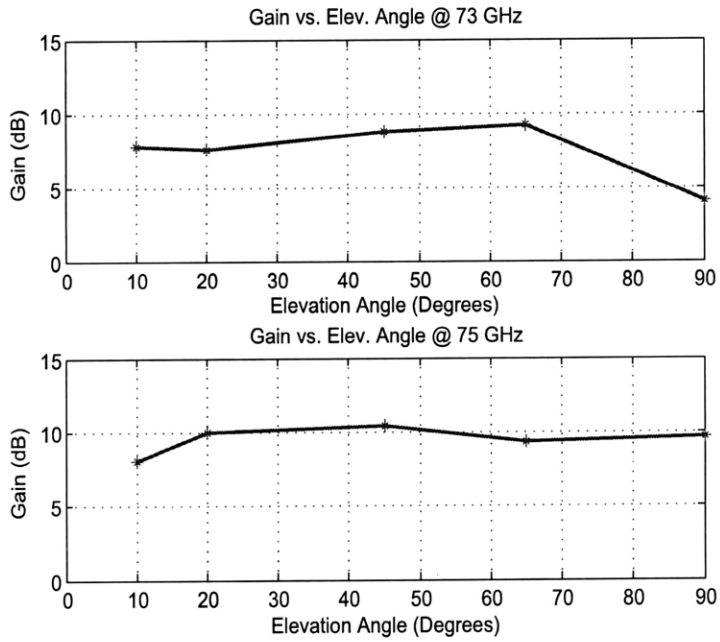

Figure 3-42: *Measured Antenna Gain vs. Angle: 73 GHz and 75 GHz, Elevation Plane.*

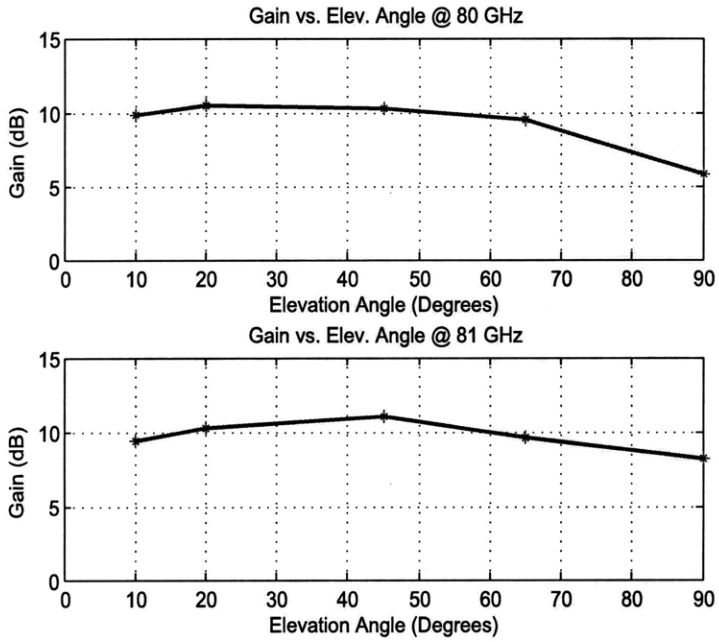

Figure 3-43: *Measured Antenna Gain vs. Angle: 80 GHz and 81 GHz, Elevation Plane.*

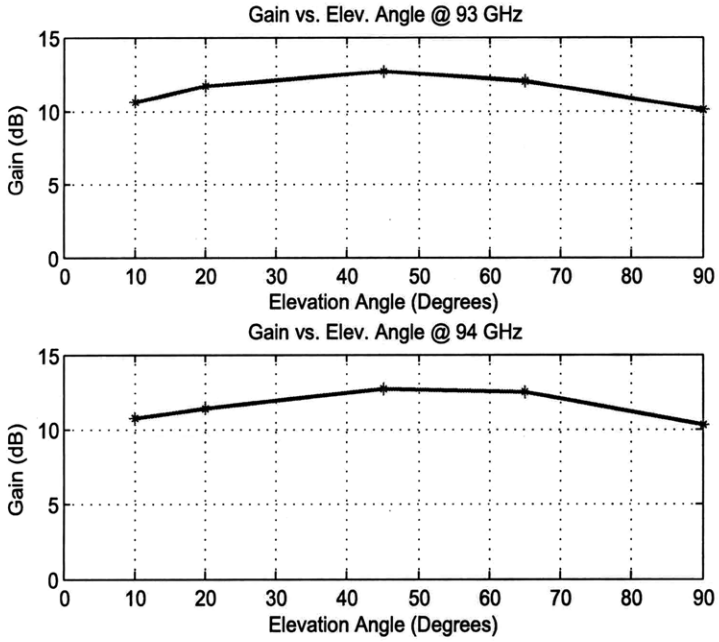

Figure 3-44: *Measured Antenna Gain vs. Angle: 93 GHz and 94 GHz, Elevation Plane.*

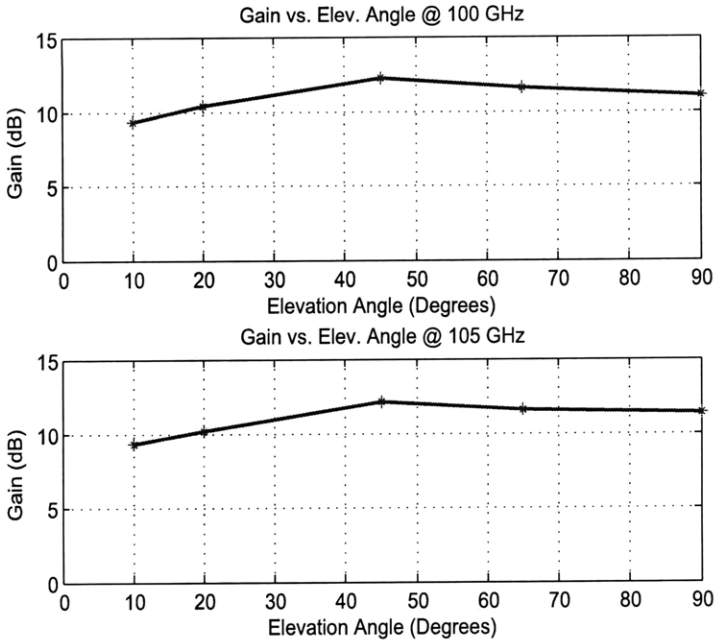

Figure 3-45: *Measured Antenna Gain vs. Angle: 100 GHz and 105 GHz, Elevation Plane.*

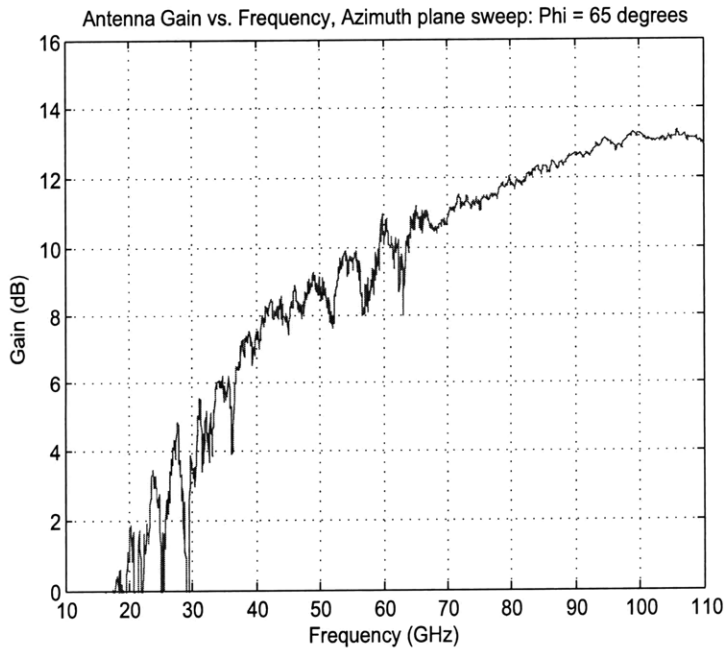

Figure 3-46: *Measured Antenna Gain vs. Frequency: Azimuth Plane.*

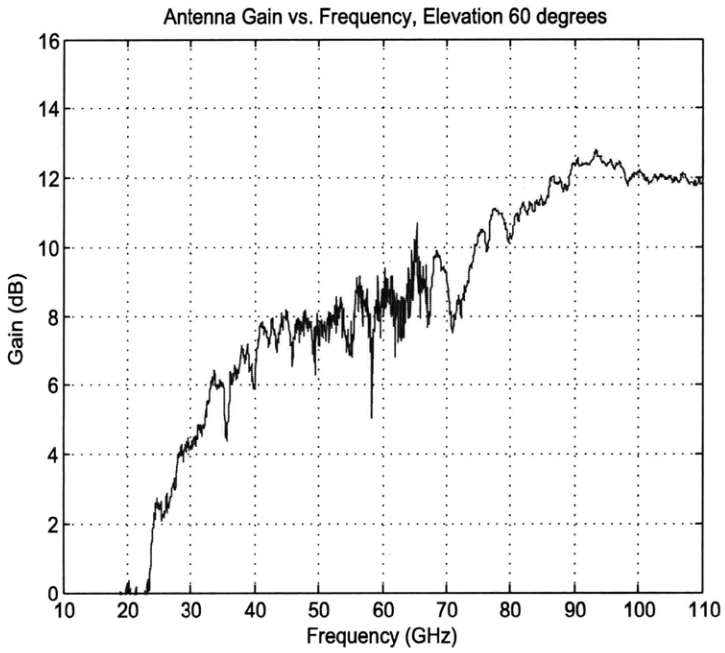

Figure 3-47: *Measured Antenna Gain vs. Frequency: Elevation Plane.*

Chapter 4

Differential Low Noise Amplifier.

The Low Noise Amplifier (LNA) typically precedes all elements in a receiver system, as it is necessary to provide substantial gain while contributing a minimum amount of noise to the system. The gain of the LNA should be high enough to overcome any noise in the subsequent stages of the system, such that the noise figure of the LNA dominates the overall receiver noise figure. The LNA also is required to provide a 50 Ω input and output impedance match to the antenna and mixer RF terminals, respectively. In some cases, when dealing with high levels of input power, linearity is an essential issue. However, for the particular case of passive imaging, the input power levels are so low that 1-dB compression point (IP1dB) requirements are not stringent. Therefore, the LNA design presented for millimeter-wave passive imaging focuses on minimizing noise figure and maximizing gain. As such, resistive degeneration is not employed (which typically degrades gain and noise figure, while improving linearity and impedance matching). A 50 Ω impedance match can be attained without degeneration, using series transmission lines and an ac coupling capacitor. Ideally, for the passive-imaging application, the LNA should achieve >20 dB gain throughout the 8 GHz of bandwidth, $\approx$5 dB noise figure, to allow for $\pm$1-3 dB of additional NF incurred in the antenna and flip-chip bonding losses, for an overall receiver noise figure of $\approx$8 dB. Stability is also a critical issue in LNA design. A fully differential LNA configuration and high reverse input-output isolation provides optimal stability conditions by mitigating common-mode noise and suppressing input-output feedback,

respectively.

Given that the Low Noise Amplifier is designed specifically to contribute the lowest noise in the system, while also providing substantial gain at the front end, it is necessary to qualify the importance of achieving low noise in this element, and also to design such that the LNA noise figure dominates the overall system noise figure. As such, some theoretical background will be provided to highlight the significant theoretical parameters of LNA design.

4.0.1 Noise Factor Derivation

Noise is usually quantified in terms of the noise factor, which is a measure of the degradation in signal-to-noise ratio introduced by a system. Noise Factor is denoted F, and defined as follows:

$$F = \frac{Total\ output\ noise\ power}{Output\ noise\ due\ to\ input\ source} \tag{4.1}$$

This can also be expressed as:

$$F = \frac{SNR_{in}}{SNR_{out}} \tag{4.2}$$

The noise figure is simply $10 * \log F$.Understanding the derivation of the "'Friis Equation"' can lead to a more comprehensive understanding of each component's contribution to the overall system noise figure [33]- [34]. Typical receivers are made up of cascaded stages, with each stage contributing a certain amount of noise to the overall output noise. We can infer the noise figure of a cascaded system theoretically by modelling each component of a receiver with its equivalent noiseless 2-port network, as shown in Figure 4-1.

Referring to Figure 4-1, derivation of the overall cascaded noise figure leads to the following equation [29], [46]:

$$F_{total} = F_1 + \frac{F_2 - 1}{G_1} + \frac{F_3 - 1}{G_1 G_2} \tag{4.3}$$

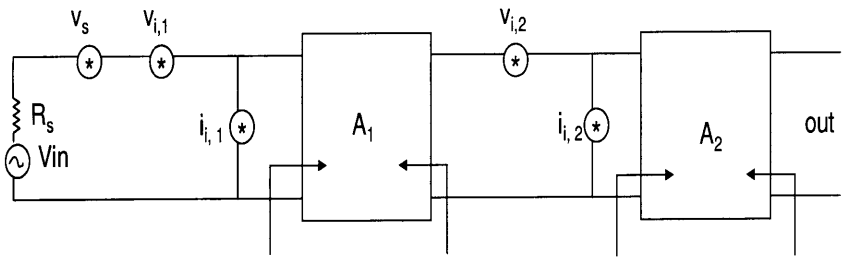

Figure 4-1: *Noise Figure calculation for cascaded stages.*

This clearly demonstrates that the front-end LNA design is crucial in order to achieve an overall low receiver noise figure.

4.1 Design

This section will detail several key issues in the LNA design, including the choice of LNA topology, designing for minimum noise figure and optimal input impedance match, and the output matching scheme.

4.1.1 LNA Topology

The LNA is a two-stage, independently biased cascode design. The cascode topology allows for higher gain and isolation. High gain in a passive imaging system is imperative, given that the input power to the receiver is very low. Figure 4-2 and Figure 4-3 show the simplified schematic and small signal model of the cascode topology, respectively, for which

$$g_m = \frac{i_c}{v_{be}}, \; and \; r_\pi = \frac{v_{be}}{i_b}. \tag{4.4}$$

Also,

$$g_m = \frac{I_c}{V_T}, \; and \; r_\pi = \frac{\beta_o}{g_m}, \; and \; r_o = \frac{V_A}{I_C}. \tag{4.5}$$

where β_o and V_A depend on the transistor design.

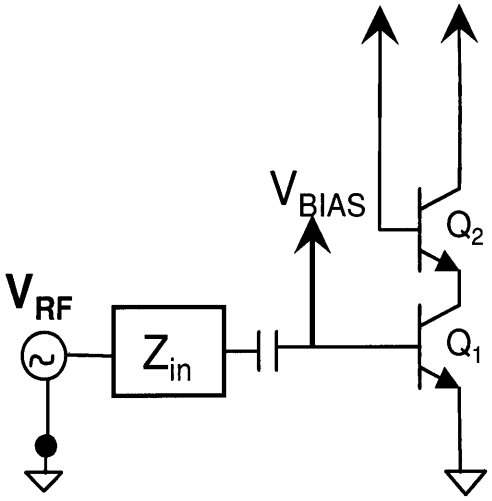

Figure 4-2: *Simple BJT Cascode Schematic.*

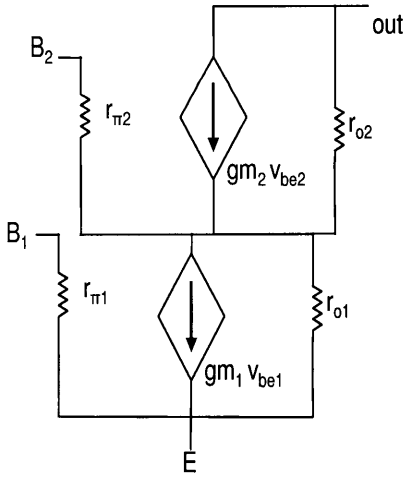

Figure 4-3: *Simplified Small Signal Equivalent Circuit Model for BJT Cascode.*

Mathematical analysis of this small-signal model yields the following parameters:

$$Voltage\ gain: \ A_v = \frac{v_{out}}{v_{in}} = -g_{m1}(r_{\pi 2}||r_{o1})(g_{m2}r_{o2}+1) \tag{4.6}$$

$$Input\ Resistance: \ R_{in} = \frac{v_{in}}{i_{in}} = r_{\pi 1} \tag{4.7}$$

$$Output\ Resistance: R_{out} = \frac{v_{out}}{i_{out}} = r_{02} + (r_{\pi 2}||r_{o1})(g_{m2}r_{o2}+1) \tag{4.8}$$

The output resistance is substantially larger than that of a single BJT stage (by a factor of $\approx\beta_o$), which is why the voltage gain is also significantly higher. However, once the cascode amplifier encounters a lower load resistance, R_L, the gain decreases significantly and becomes approximately the same as that of a single-stage amplifier, since the large output resistance is in parallel with the significantly smaller (typically 50 ohm) load resistance. However, the main difference between these two topologies is that the cascode transistor provides a very small input resistance ($\frac{1}{g_{m2}}$, on the order of $\approx 50\Omega$), which decreases the output resistance of the common emitter transistor, substantially limiting its gain. The overall gain is recovered by the common base cascode, but the Miller feedback capacitance from the collector to base of the common emitter stage is dramatically reduced. A reduced Miller capacitance improves S12 and thus yields better stability. Therefore, the cascode amplifier topology has a much wider bandwidth, and therefore, a much larger gain at higher frequencies.

The two stages are cascaded together to provide the required amount of gain at the front end. Each stage can be biased independently, which allows for gain control on the second stage while impacting the noise figure (NF) minimally. The LNA schematic is shown in Figure 4-4.

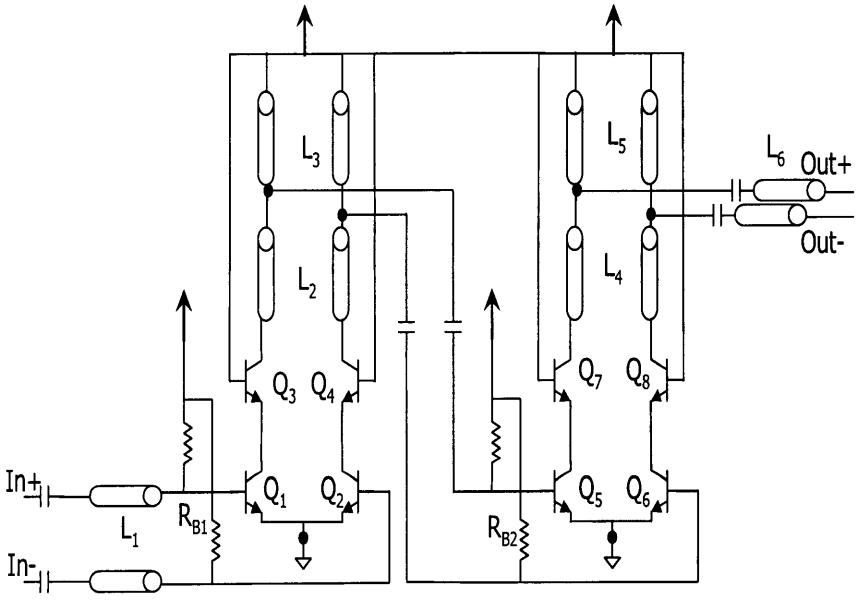

Figure 4-4: *2-Stage Cascode LNA Schematic.*

4.1.2 Design for Simultaneous Minimum NF and Impedance Match

In designing the differential LNA, the simultaneous minimum NF and input impedance match are achieved by matching the optimal source impedance to 50 ohms. This is detailed in [47]. By going through these derivations, it becomes clearer that the minimum noise figure can be achieved if the actual source susceptance and conductance are optimal. These parameters can be designed to approximately equal 50 Ω. These derivations are also connected to a more complex expression which relates the minimum noise figure to BJT parameters I_C, V_T, f_T, β_o, R_E, and R_B. This derivation is helpful in that it intuitively clarifies how the minimum noise figure is affected by these physical BJT parameters. To describe this process theoretically, we must revert back to the noise figure calculation in this chapter's introduction. We can derive the input-referred noise figure by referring to the equivalent 2-port model of Figure ??, this time expressed by its Norton equivalent, shown in Figure 4-5. The configuration is shown such that we can calculate the noise figure in terms of input short circuit current, where:

$$F = \frac{Output\ Noise\ Power\ (tot)}{Output\ noise\ due\ to\ input\ source} = \frac{i^2_{out(tot)}}{i^2_{iout(in)}} = \frac{i^2_{in,sc(tot)}}{i^2_{in,sc(in)}} \tag{4.9}$$

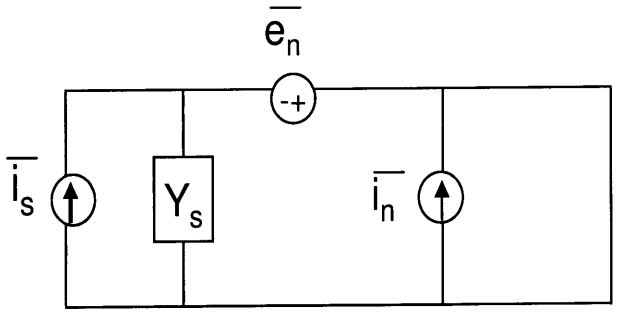

Figure 4-5: *2-Port Network for Short Circuit Current Analysis.*

Here, we represent the noise figure in terms of the input short circuit current because we scale both output currents by the current gain β in order to get the input-referred noise figure expression. Next, assuming that the source noise power and the two-port network are uncorrelated, the expression for the noise factor becomes, by inspection of Figure 4-5:

$$F = \frac{i_s^2 + |i_n + Y_s e_n|^2}{i_s^2} \tag{4.10}$$

It is necessary to consider the possibility of correlation between e_n and i_n, such that $i_n = i_c + i_u$, where i_c represents the correlated noise power, and i_u represents the uncorrelated noise power. We can express the correlated values in terms of a "correlation" admittance, such that $i_c = Y_c e_n$, where

$$Y_c = \frac{i_c}{e_n} = G_c + jB_c \tag{4.11}$$

Algebraic manipulation of (4.10) in terms of the correlation admittance Y_c, yields the resulting noise factor:

$$F = 1 + \frac{i_u^2 + |Y_c + Y_s|^2 e_n^2}{i_s^2} \tag{4.12}$$

Note that expression (4.12) is written in terms of voltage and noise currents; we can now replace these terms with impedances and admittances so as to determine minimum noise factor by finding the optimal source admittance:

$$R_n = \frac{e_n^2}{4kT\Delta f}, \quad G_u = \frac{i_u^2}{4kT\Delta f}, \quad G_s = \frac{i_s^2}{4kT\Delta f} \tag{4.13}$$

$$F = 1 + \frac{G_u + |Y_c + Y_s|^2 R_n}{G_s} \tag{4.14}$$

In order to find the optimal source admittance for the minimum noise factor, we first must express the admittances Y_c and Y_s as the sum of B (susceptance) and G

(conductance):

$$F = 1 + \frac{G_u + [(G_c + G_s)^2 + (B_c + B_s)^2]R_n}{G_s} \tag{4.15}$$

Next, we must differentiate the noise factor with respect to the source susceptance and conductance. Setting the derivative to zero will determine the total source admittance that will yield the minimum noise factor:

$$\frac{dF}{dB_s} = [\frac{2B_c}{G_s} + \frac{2B_s}{G_s}]R_n = 0 \rightarrow -B_c = B_s = B_{opt} \tag{4.16}$$

$$\frac{dF}{dG_s} = -G_s^- 2(G_u + G_c^2 R_n) + R_n = 0 \rightarrow R_n = \frac{G_u + G_c^2 R_n}{G_s^2} \rightarrow G_s = \sqrt{\frac{G_u}{R_n} + G_c^2} = G_{opt} \tag{4.17}$$

Now, having solved for the optimal source admittance for the minimum noise factor, we can express F_{min} in terms of the optimal source susceptance and conductance:

$$F_{min} = 1 + 2R_n \left(\sqrt{\frac{G_u}{R_n} + G_c^2} + G_c \right) = 1 + 2R_n \left(G_{opt} + G_c \right) \tag{4.18}$$

Finally, we can express the true noise factor F in terms of F_{min}:

$$F = F_{min} + \frac{R_n}{G_s} \left((G_s - G_{opt})^2 + (B_s - B_{opt})^2 \right) \tag{4.19}$$

Given (4.19), we can conclude that the minimum noise figure can, in fact, be achieved, provided that the actual source conductance and susceptance are optimal. When we take these parameters into account, however, we also must consider the RF input impedance match. In order to preserve the minimum noise figure, we begin the design by finding the appropriate bias current through the common emitter transistor of the first stage of the LNA. The bias current which yields the lowest minimum noise figure is selected. Next, the first-stage common emitter transistor is sized to bring the optimum source impedance close to 50 ohms. This can be done in simulation, by analyzing constant noise factor circles on a Smith Chart, and finding the common

emitter size which places the minimum noise figure nearest the center of the Smith Chart. The final matching of input impedance and optimum source impedance to 50 ohms is set by the transmission line (L1) attached to the bases of Q1 and Q2. The coupling capacitor at the input is also used as part of the matching network.

In this design, since optimization of gain and noise figure were key priorities, no explicit emitter degeneration was used. Degeneration is typically used to achieve better linearity in a circuit; however, given that the power received in a passive imager is so low, it is not a substantial concern. Emitter degeneration typically degrades the overall g_m of the transistor. Since gain is proportional to g_m, and noise figure is inversely proportional to g_m, emitter degeneration thereby degrades both the gain and noise figure (see Figure 4-6).

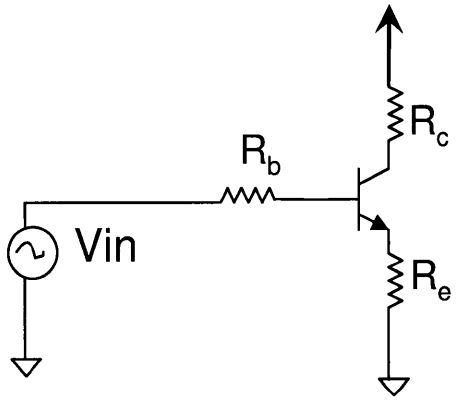

Figure 4-6: *Common Emitter Transistor with Emitter Degeneration.*

$$G_m \approx \frac{g_m}{1 + g_m R_E} \tag{4.20}$$

We can also observe directly that the minimum noise figure is increased proportionally by a factor of $\sqrt{R_E}$ in Voinigescu's derivation for minimum noise factor [47]:

$$F_{min} \approx 1 + \frac{n}{\beta_o} + \frac{f}{f_T}\sqrt{\frac{2I_C}{V_T}(R_E + R_B)\left(1 + \frac{f_T^2}{\beta_o f^2}\right) + \frac{n^2 f_T^2}{\beta_o f^2}} \tag{4.21}$$

Connecting to 4.21 from 4.18 is nontrivial in that it requires derivation of the noise

resistance R_n, optimum source admittance Y_{opt}, and F_{MIN} in terms of the noise correlation matrix whose parameters are defined as C_{A11}, C_{A21} and C_{A22}. The noise correlation matrix is defined for a two-port network as follows [48]:

$$C_A = 2kT \begin{pmatrix} R_n & \frac{NF_{min}-1}{2} - R_n Y_{opt} \\ \frac{NF_{min}-1}{2} - R_n Y_{opt}^* & R_n |Y_{opt}|^2 \end{pmatrix} \; where from Equation 4.11,$$

$Y_c = Y_{opt}$, and:

$$R_n = C_{A11} \tag{4.22}$$

$$Y_{opt} = G_{opt} + jB_{opt} = \sqrt{\frac{C_{A22}}{C_{A11}} - \left(\frac{Im(C_{A12})}{C_{A11}}\right)^2} + j\frac{Im(C_{A12})}{C_{A11}} \tag{4.23}$$

$$F_{MIN} = 1 + 2(Re(C_{A12})) + C_{A11} G_{opt} \tag{4.24}$$

The Y-parameter matrix is defined for the two-port network as follows:

$$\begin{pmatrix} I_1 \\ I_2 \end{pmatrix} = \begin{pmatrix} Y_{11} & Y_{12} \\ Y_{21} & Y_{22} \end{pmatrix} = \begin{pmatrix} V_1 \\ V_2 \end{pmatrix}$$

where $Y_{11} = \frac{I_1}{V_1}$, $Y_{12} = \frac{I_1}{V_2}$, $Y_{21} = \frac{I_2}{V_1}$, and $Y_{22} = \frac{I_2}{V_2}$. These y-parameters are derived from the general 2-port noise-free transistor model, as shown in Figure 4-7, where the base-emitter connection represents port 1, and the collector-emitter connection represents port 2 [47].

The parameters of the noise correlation matrix are defined as follows [47]:

$$C_{A11} = \frac{\overline{v_n^2}}{4kT\Delta f} = \frac{\overline{i_c^2}}{4kT\Delta f |Y_{21}|^2} + (r_E + r_B) \approx \frac{n^2 V_T}{2I_C} + (r_E + r_B) \tag{4.25}$$

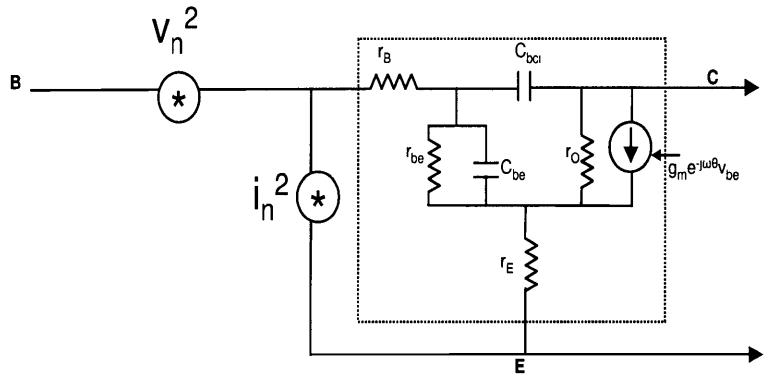

Figure 4-7: *Noise-Free Y Parameters block. The connection between Base-Emitter represents Port 1, and the connection between Collector-Emitter represents Port 2.*

where n is approximately equal to one, the collector current "ideality factor."

$$C_{A21} = \frac{v_n^* i_n}{4kT\Delta f} = \frac{Y_{11} * \overline{i_c^2}}{4kT\Delta f |Y_{21}|^2} \tag{4.26}$$

$$C_{A22} = \frac{\overline{i_n^2}}{4kT\Delta f} = \frac{Y_{11}^2 * \overline{i_c^2}}{4kT\Delta f |Y_{21}|^2} + \frac{\overline{i_b^2}}{4kT\Delta f} \tag{4.27}$$

Substituting Equations 4.22-4.24 into 4.25-4.27 yields 4.28-4.30 [47]:.

$$R_n = \frac{n^2 V_T}{2I_C} + (r_E + r_B) \tag{4.28}$$

$$Y_{opt} = \sqrt{\frac{I_B Y_{21}^2 + I_C |Y_{11}|^2}{2V_T |Y_{21}|^2 (r_E + r_B) + I_C} - \left(\frac{I_C Im(Y_{11})}{2V_T |Y_{21}|^2 (r_E + r_B) + I_C} \right)^2} - j \frac{I_C Im(Y_{11})}{2V_T |Y_{21}|^2 (r_E + r_B) + I_C} \tag{4.29}$$

$$F_{MIN} = 1 + \frac{I_C}{V_T Y_{21}^2} \left(Re(Y_{11}) + \sqrt{\left(1 + \frac{2V_T |Y_{21}|^2 (r_E + r_B)}{I_C} \right) \left(|Y_{11}|^2 + \frac{I_B |Y_{21}|^2}{I_C} \right) - Im(Y_{11})^2} \right) \tag{4.30}$$

This derivation then leads to a final expression for Y_{opt} and R_{opt} after solving for the y-parameters, for which

$$Y_{opt} \approx \frac{f}{f_T R_n} * \left(\sqrt{\frac{I_C}{2V_T}(r_E + r_B)(1 + \frac{f_T^2}{\beta_o f^2}) + \frac{n^2 f_T^2}{4\beta_o f^2}} - j\frac{n}{2} \right) \tag{4.31}$$

$$R_{opt} \approx \frac{f}{f_T R_n} * \frac{\sqrt{\frac{I_C}{2V_T}(r_E + r_B)(1 + \frac{f_T^2}{\beta_o f^2}) + \frac{n^2 f_T^2}{4\beta_o f^2}}}{\frac{I_C}{2V_T}(r_E + r_B)\left(1 + \frac{f_T^2}{\beta_o f^2}\right) + \frac{n^2}{4}\left(1 + \frac{f_T^2}{\beta_o f^2}\right)} \tag{4.32}$$

With these expressions, we can return to the original expression for F_{MIN}, as in Equation 4.18, shown below for convenience:

$$F_{min} = 1 + 2R_n (G_{opt} + G_c) \tag{4.33}$$

where $G_c \approx 0$. Using the results in Equation 4.31, given that $Y_{opt} = G_{opt} + jB_{opt}$, we can simplify for F_{min} to yield the results originally presented in 4.21:

$$F_{min} \approx 1 + \frac{n}{\beta_o} + \frac{f}{f_T}\sqrt{\frac{2I_C}{V_T}(R_E + R_B)\left(1 + \frac{f_T^2}{\beta_o f^2}\right) + \frac{n^2 f_T^2}{\beta_o f^2}} \tag{4.34}$$

where n is the collector current "ideality factor" (≈ 1), and β_o is the dc current gain, which renders the term effectively zero. This comes from the G_c term, which tends to approximate to zero. [29].

4.1.3 Output Match

The output match of the LNA is achieved through classical transmission line theory using shunt-stub and series transmission lines Figure 4-8 - Figure 4-11. The output matching scheme can be calculated theoretically by modeling the collector-base capacitance and the base resistance to ground when looking into the collector of the cascode transistors of Figures 4-8 and 4-9. Once the appropriate equivalent circuit values are determined, this complex impedance is normalized and placed on the admittance chart Figure 4-11. First, a series transmission line is adjusted moving away from the load in order to transform the real part of the load impedance to 50 ohms (normalized, curve 1 (C1) in Figure 4-11). Next, a shunt-stub line is adjusted (curve 2 (C2) in Figure 4-11), connected up to Vdd. This transmission line is purely reactive, and therefore is used to negate the reactive component of the load impedance, and thus match to the 50 ohm port.

4.2 Measured Results

Figure 4-12 illustrates the simulated vs. measured results for the 77-GHz LNA. The input match and gain achieve generally good agreement between simulation and measurement around 77-GHz. However, the NF shows a significant amount of discrepancy below 74 GHz because the test setup included a downconversion mixer with a cutoff frequency of 75-GHz. As such, an RF input below 74-75 GHz cannot be measured ac-

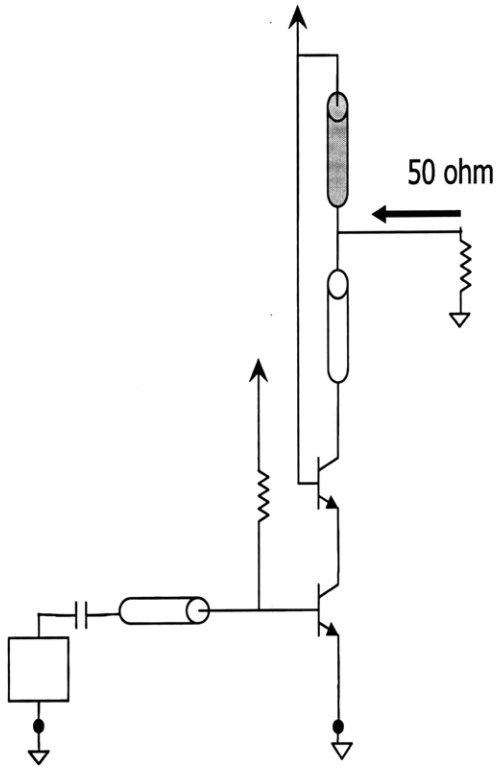

Figure 4-8: *2nd Stage of LNA for Output Load Approximation.*

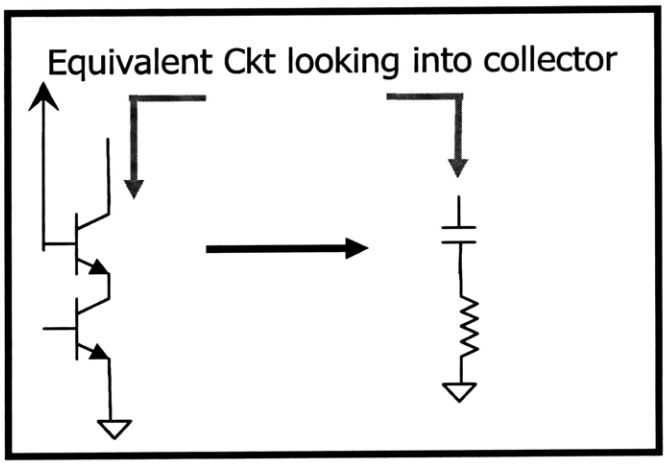

Figure 4-9: *Approximation of Equivalent Circuit Looking into Collector of the Cascode Transistor.*

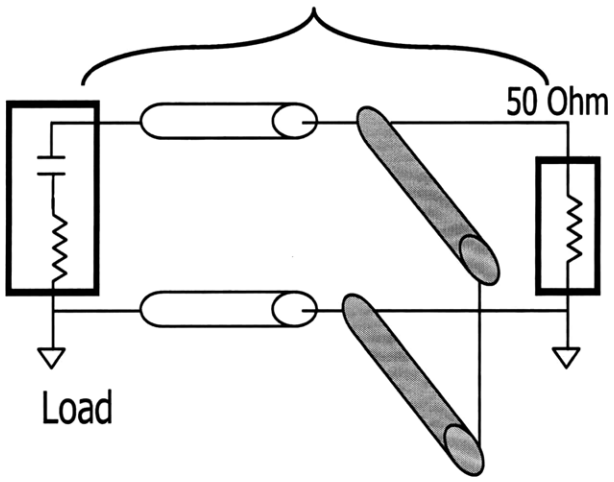

Figure 4-10: *Transmission Line Matching Network (Shunt Stub and Series Transmission Lines).*

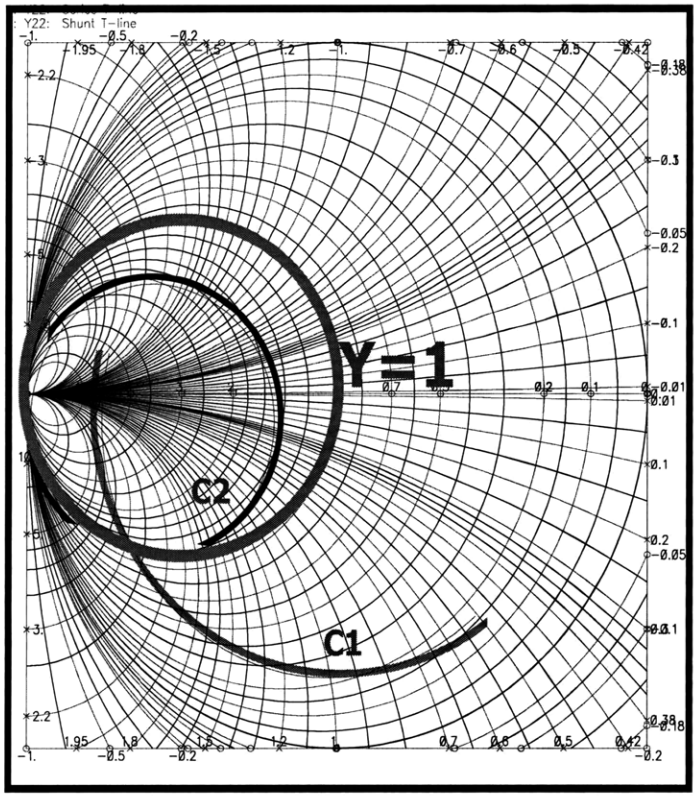

Figure 4-11: *Smith Chart Sweep of Transmission Line Lengths for Optimal Load Impedance Matching.*

curately. The output match plot (S22) indicates a discrepancy between the measured and simulated result in that there is an additional resonant point at approximately 50-GHz. This is due to an unmodeled series parasitic inductance in the output stage.

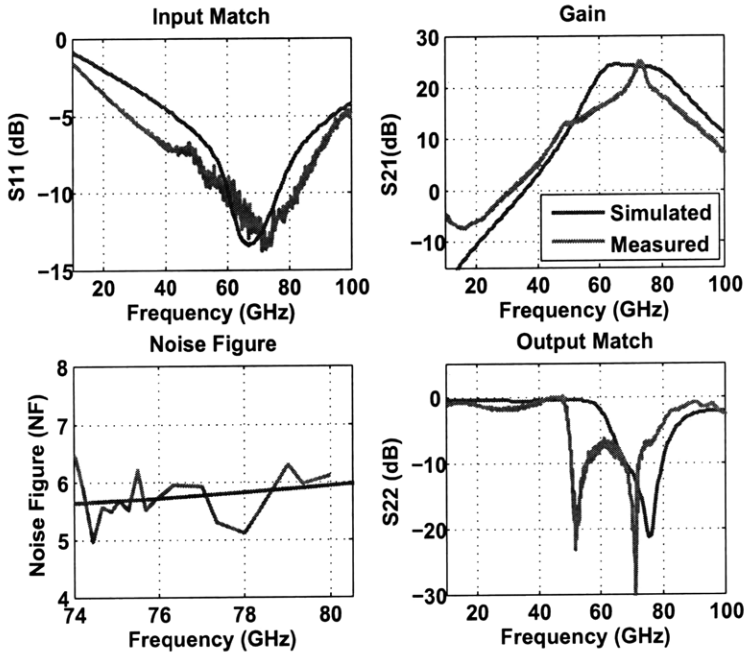

Figure 4-12: *LNA Simulated vs. Measured Results.*

This parasitic effect has been reproduced in simulations, as illustrated in Figure 4-13. The arrows in the LNA die photo indicate a path of ac coupling capacitors which added parasitic inductance that the extraction tool did not model. This inductive path is illustrated in the schematic sketch at the bottom of Figure 4-13. In simulation, transmission lines were added to this path in order to reproduce the inductance introduced by this parasitic path, and thereby reproduce the 50-GHz resonance. These transmission lines were simulated with the extracted layout to achieve the plotted result shown in Figure 4-14. The plot shown in Figure 4-14 matches more closely with the characteristic shown in the measured results, in that it achieves a secondary resonance point close to 50 GHz. There is some discrepancy in the absolute value

of the impedance match (S_{22}) and the frequency characteristic. However, the main concept that the parasitic inductance simulation proved was that the characteristic discrepancy observed between simulation and measurement could be replicated with the addition of parasitic inductance in the output signal path.

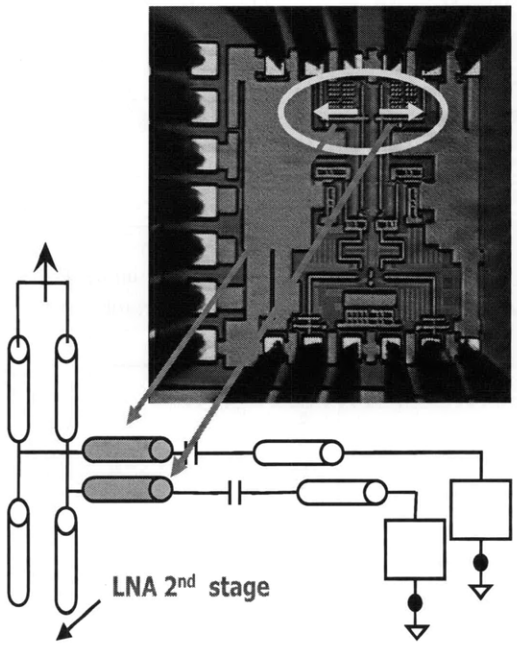

Figure 4-13: *Illustration of Inductive Parasitic Path Occuring at the Output Stage of the LNA*

The LNA achieved 30 dB of reverse isolation throughout the frequency range. High reverse isolation is imperative in that it prevents feedback from creating instabilities. However, it was found in measurement that oscillations would occur for high values of bias voltage for the second stage common emitter transistor. The second stage bias voltage was designed for 1.2 V; however, since oscillations occurred at that voltage, the bias voltage was reduced to a stable point of approximately 0.9-1.0 V.

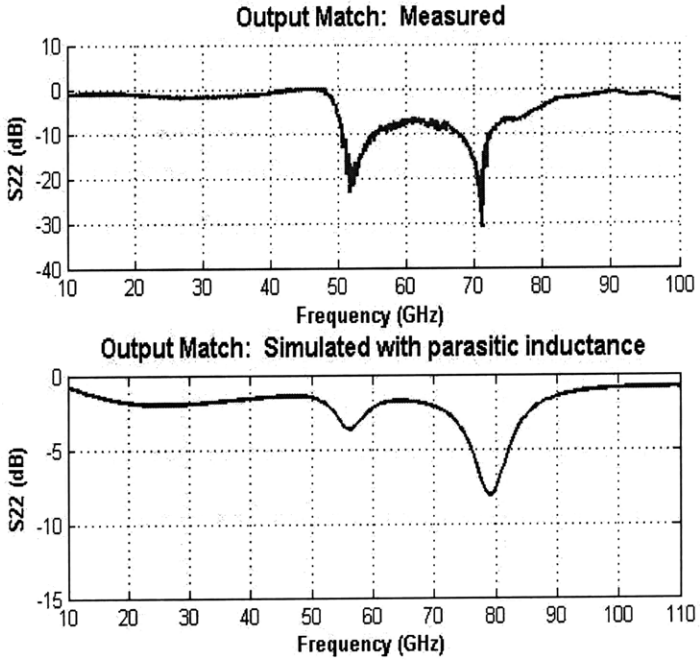

Figure 4-14: *Simulated vs. Measured Results with Parasitic Inductance*

4.3 94 GHz LNA

There are several advantages to designing a passive imaging system for the 94-GHz imaging band, including higher spatial resolution, lower atmospheric attenuation, and higher antenna gain for a given antenna size. Therefore, as described in the System section of this thesis, a front end receiver operating in the 91-99 GHz region was designed. The LNA design used the same topology as the 77-GHz design already described in this chapter, with the input and output matching networks re-tuned for operation in the 91-99 GHz frequency regime. Collector current and overall power dissipation remained largely similar to that of the 77-GHz design. Figure 4-15 illustrates the simulated vs. measured results for the 91-99 GHz range, including input and output match, gain and noise figure, as also in the 77-GHz version, Figure 4-12.

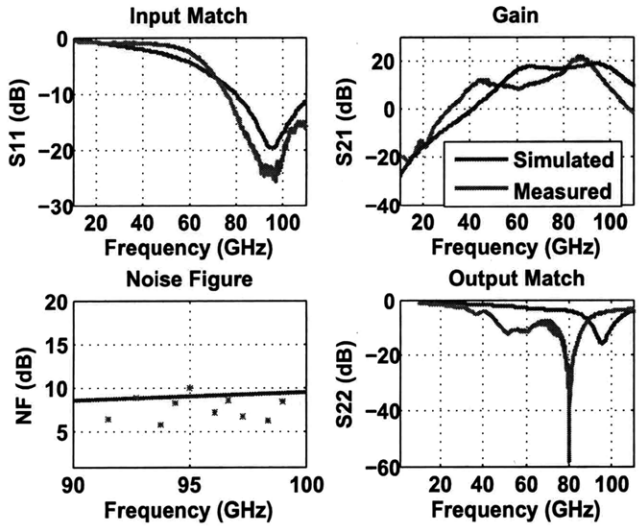

Figure 4-15: *LNA 91-99 GHz Simulated vs. Measured Results.*

The 94-GHz LNA exhibits excellent gain, noise figure, and S11 performance with

some discrepancy in the S22 match. This can be attributed to a similar phenomenon as described in the 77-GHz LNA; albeit this result is less pronounced, since the output match exhibits simply a frequency mismatch, rather than an excessive secondary resonance. However, the overall S22 performance is still adequate for up to 90-GHz. This impedance match improves for the integrated version of the front end, because the output bondpads are removed, achieving an overall higher frequency output impedance match. The same phenomenon occurs for the 77-GHz LNA. The LNA exhibits excellent gain and noise figure, especially at 90-GHz, but also performs considerably well (> 10 dB gain) for 60 GHz of bandwidth.

4.4 LNA Summary and Conclusions

LNAs designed for 73-81 GHz and 91-99 GHz were presented, achieving maximum gains of 26 dB and 22 dB, respectively. The measured center frequencies were shifted down from the simulated center frequencies due to unmodelled parasitic inductance. However, these measured results indicate standalone measurements with output bondpads. Integration of each LNA with the mixer terminals eliminates the bondpads, thereby shifting the frequencies upward. Table 4.1 summarizes the 91-99 GHz LNA performance at 94-GHz and the 73-81 GHz LNA at 77 GHz, as well as 90 GHz and 75 GHz, where each respective LNA performed best. Performance is highlighted in terms of maximum gain, NF, S11, S22, and DC Power Consumption.

Table 4.1: LNA Performance Parameters Table

Freq. (GHz)	Max Gain (dB)	Noise Figure (dB)	S11, S22 (dB)	P_{DC} mW)	Bandwidth
90	22	7.0	-25, -9.5	56	40-100 GHz
94	16	8.0	-23, -5	56	40-100 GHz
77	20	6.0	-11.5, -7.5	55	45-95 GHz
75	26	5.5	-13, -10	55	45-95 GHz

Chapter 5

Double-Balanced Mixer

The mixer is foundational to the superheterodyne architecture of a receiver system, which provides the frequency translation from an RF input to an IF output for digital processing. Specifically in millimeter-wave applications, the RF signal occurs at such a high frequency, it must be downconverted for baseband processing. The mixer is typically a nonlinear, active system made up of transistors, but it can also be passive (that is, it may be made up of active components, but it provides only conversion loss). A mixer features three ports: The RF (Radio Frequency) port, the LO (Local Oscillator) port, and the IF (intermediate frequency) port. The LO signal is the strongest signal, which turns the active switches on and off; the RF signal is modulated by the LO signal, and the IF output signal is obtained by low-pass filtering at the mixer output.

5.1 Fundamental Mixer Characteristics

All mixers provide time-domain multiplication of two signals, which results in the convolution of signals in the frequency domain. The trigonometric identity shown below can more clearly elucidate this concept:

$$(A\cos\omega_1 t)\,(B\cos\omega_2 t) = \frac{AB}{2}[\cos(\omega_1-\omega_2)t + \cos(\omega_1+\omega_2)t] \tag{5.1}$$

The primary function of any mixer is to provide frequency translation from a high RF signal to a manageable intermediate frequency. However, there are several other key parameters to consider in mixer design, as these parameters tend to impact the performance of the overall receiver system. Among the most important performance parameters are Conversion Gain, Noise Figure, Linearity and LO-RF Isolation.

Mixer conversion gain is usually defined as the "voltage conversion gain", ie. the ratio of the rms voltage at the output of the IF port to the value of the rms voltage at the RF input port. Another way to define mixer conversion gain is "power conversion gain", which is the ratio of the power available at the IF load to the power available from the RF source. Since it is more straightforward to measure power conversion gain, we will refer to the mixer conversion gain as the power conversion gain in this thesis.

The Noise Figure of a mixer can be referred to as either the double-sideband (DSB) NF or the single-sideband (SSB) NF. In either case, it is defined as the ratio of the SNR at the RF port to the SNR at the IF port. However, the nuance in the noise figure definition considers the fact that image noise is frequency-translated into the desired IF signal band. More specifically, the desired RF signal is downconverted with the noise in the RF signal band as well as the noise in the image band. Therefore, considering a noiseless downconversion mixer, if one assumes that the frequency translation is the same in the signal band as in the image band, then the output SNR will be half of the input SNR. By this definition, even a noiseless mixer has a NF of 3 dB. This is defined as the SSB NF. The DSB NF is typically 3-dB lower than the SSB NF. In this thesis, all references to NF will be in terms of the SSB NF.

A mixer's linearity is often a more important parameter than the LNA linearity, since the mixer follows the LNA gain stage, making the incoming RF signal significantly larger than it appears at the antenna terminals. Linearity is a measure of the dynamic range of the mixer, usually measured by the 1-dB compression point. This measurement indicates the point at which the output signal stops being proportional to the input signal. In this case, as the RF signal increases, the output signal remains unchanged. The 1-dB compression point indicates the RF input for which the ideal

output and the real output differ by 1-dB.

LO-RF port isolation requirements vary to a large extent, depending upon the environment and frequency regime in which the mixer is used. If there are several interferers in the specified RF frequency range, then a high amount of RF-LO feedthrough would allow interferers to interact with the mixer core LO port, and this could potentially interfere with the modulation of the desired RF signal. A few reasons for requiring high LO-RF isolation is that LO leakage could result in radiation of the LO signal through the RF antenna, or high amounts of LO signal on the subsequent IF stage could desensitize the succeeding receiver stages.

5.2 Mixer Topologies

Among the several mixer topologies that are commonly used, this thesis focuses on active mixers that incorporate conversion gain. The two mixer topologies investigated in this thesis for millimeter-wave applications are single-balanced and double-balanced topologies.

The single-balanced topology employs a current-steering method such that a differential LO signal is fed to each input of a differential pair, and the RF is fed through a transconducting tail transistor, as shown in Figure 5-1. The LO signal must be large enough such that the total output current is commutated from Q1 to Q2, and vice versa. This particular multiplier converts the RF voltage into a current, which occurs at the collector of the transconducting tail transistor. This current is then multiplied by the LO square wave, such that the output current can be defined by equation (5.2):

$$i_{out}(t) = sgn[\cos\omega_{LO}t](I_{BIAS} + I_{RF}\cos\omega_{RF}t) \tag{5.2}$$

The main caveat in single-balanced topology is that of poor RF-LO isolation, which tends to overload IF amplifiers. Also, poor LO isolation can cause the LO signal to reflect at the output port and radiate out of the transmit/receive antenna. If substantial LO suppression is desired, a double-balanced topology may be used, which

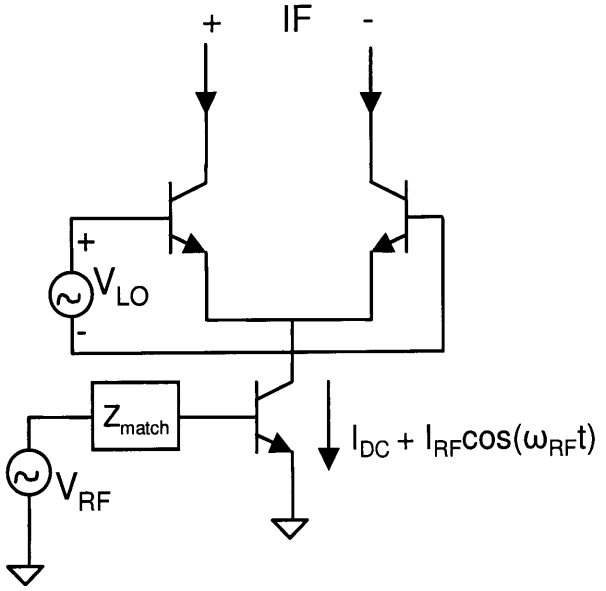

Figure 5-1: *Single-Balanced Mixer Topology.*

exploits symmetry to cancel the LO signal. A double-balanced mixer topology is shown in Figure 5-2. This is essentially two single-balanced mixers combined, such that the RF transconductors are differential, as well as the LO inputs. The anti-parallel configuration of the LO signals yield a sum of the LO terms to zero, but the RF term will double: As V_{LO} is positive, Q_1 and Q_4 turn on: $IF_{out+} = I_{RF+}$, $IF_{out-} = I_{RF-}$. Then, $IF_{total} = IF_{out+} - IF_{out-} = 2I_{RF}$

The RF transconductance amplifier is typically implemented in one of two ways; either a common-base or common-emitter amplifier is used (Figures 5-3 and 5-4). The common-base typically achieves an impedance match more easily, since the impedance looking into a common-base amplifier is $\frac{1}{g_m}$, which is closer to 50 Ω than the input impedance of a common-emitter, which is $r_\pi = \frac{\beta_o}{g_m} = \frac{V_T}{I_B}$. However, the common emitter configuration has superior noise performance. For the case of the common-base amplifier, the common-base configuration has unity current gain. Thus, whatever noise current is present at the emitter of the common base amplifier will appear directly at the collector. Thus, all of the noise from the RF source is passed directly to the output of a common-base amplifier. However, for the case of the common-

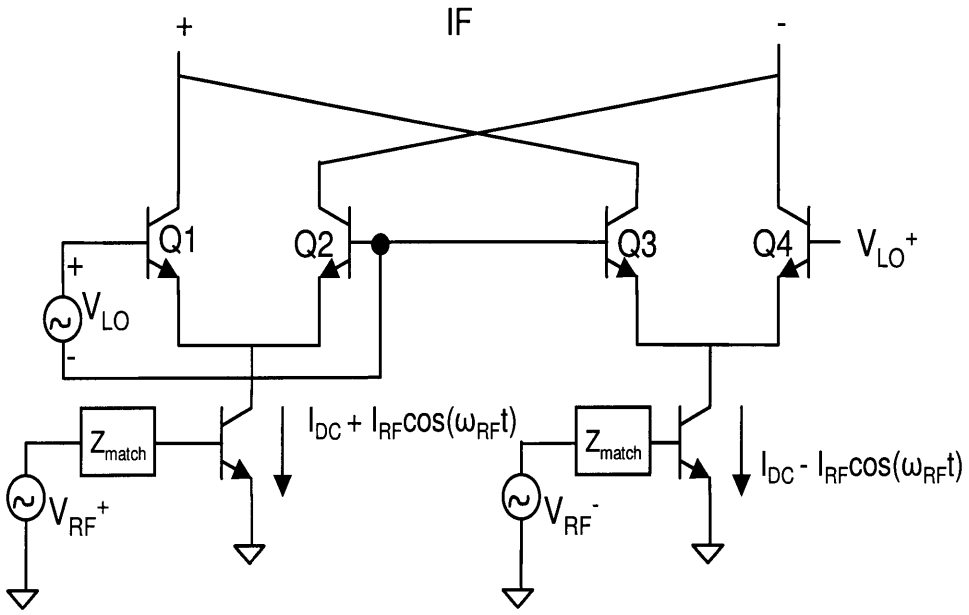

Figure 5-2: *Double-Balanced Mixer Topology.*

emitter, the source noise has a path to ground through the emitter. Therefore, the common-base configuration will theoretically always have a higher minimum noise figure than that of the common-emitter. It is for this reason that many designers tend to use the common-emitter configuration. This configuration was also chosen for the mixer design presented in this thesis, after simulation analysis.

5.3 77-GHz Double-Balanced Downconversion Mixer

This section will detail the design, characterization and results of the 77-GHz double-balanced mixer used in both the 77-GHz and 94-GHz front end receiver designs.

5.3.1 Design

The 77-GHz Double-Balanced Mixer core design is a Gilbert-cell topology with inductive degeneration. A single-balanced configuration would allow substantial LO feedthrough given its inherently poor LO-RF isolation. As such, a double-balanced configuration (and hence, a fully-differential system) was chosen. The mixer schematic

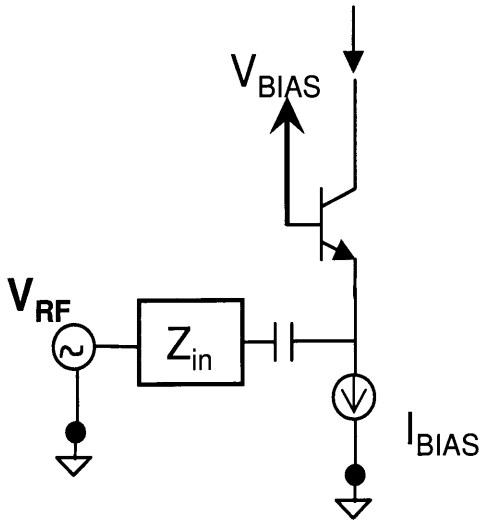

Figure 5-3: *Common-base configuration.*

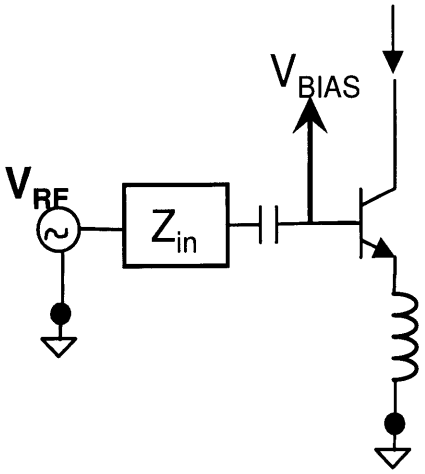

Figure 5-4: *Common-emitter configuration.*

is shown in Figure 5-5, and was originally designed by Helen Kim of Lincoln Laboratories. The RF transconductance stage is a common-emitter topology, which implements an impedance match for minimum noise figure, following the technique described in [47]. The series transmission line in the RF impedance matching network is 260 μm long, and the inductive degeneration is 124 μm long, providing 46pH of inductance.

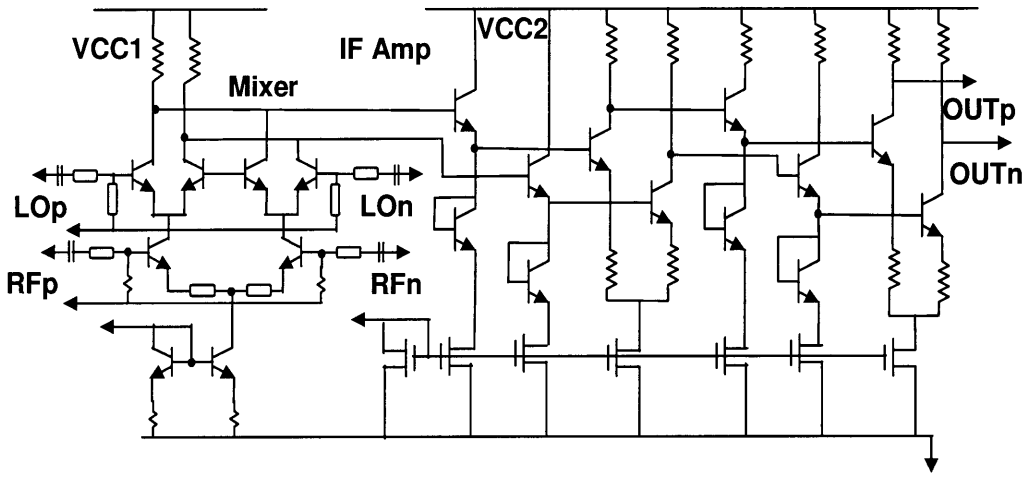

Figure 5-5: *Double-Balanced Mixer Schematic.*

The RF mixer core is followed by a two-stage IF amplifier, each stage consisting of an emitter-follower followed by an emitter-coupled pair to provide a substantive amount of IF gain. The diode-connected BJTs below the emitter-followers provide a $1/g_m$ resistance and a fixed DC voltage drop, which remains consistent at approximately 0.8 V- 0.88 V over process and temperature. These allow for the same DC value to remain at the drain of the NMOS current sources, which bias the current through the IF amplifier stages. The NMOS current sources are used rather than BJTs to save voltage supply headroom.

This double-balanced mixer is designed for an RF input of 73-81 GHz, which is downconverted to 1-9 GHz IF. The 2-stage IF amplifier further amplifies and matches to 50 ohms. The transistor size, bias current and transmission line matching were chosen for optimum NF and maximum gain while accommodating the required IP1dB.

The stand-alone mixer has a broadband 180 balun at LO and RF input ports

for testing purposes. These baluns each occupy an area of 1mm x 525 μm, and are used strictly for simplification of testing, such that single-ended external LO and RF sources can be used to interface with the chip. The baluns provide differential RF and LO input signals to the respective input ports of the double-balanced mixer.

5.3.2 Measured Results

The mixer noise figure was tested using an Agilent Noise Figure Analyzer and the setup described in the Chapter 2 of this thesis. The mixer noise figure ranged from $\approx 12 - 14$ dB from 73-81 GHz, and the conversion gain ranged from $\approx$ 20-26 dB for the 8-GHz RF frequency range. The conversion gain and NF measured vs. simulated results are shown in Figure 5-6.

The measured results agree relatively well vs. simulated results, with discrepancies occurring at the upper frequency range. This is most likely due to unmodeled parasitic inductance occuring in the RF input stage, which makes the input impedance match more frequency-tuned and less wideband. With a more tuned RF input impedance match at the lower end of the RF frequency range than at the high end, the conversion gain will drop with increasing frequency. The mixer also achieved an input-referred 1-dB compression point of -26 dBm, and an output-referred 1-dB compression point of -2 dBm. Considering the expected RX power of the system to be -60 dBm, the linearity this mixer achieved is certainly well within its specified expected performance. Figure 5-7 illustrates the mixer 1-dB compression point (including the 180 balun loss).

The mixer achieved better than 40 dB of LO-RF and LO-IF isolation. LO-IF isolation is important in that the LO signal is large-signal and could potentially overload the IF amplifier. LO-RF isolation is important because it is undesirable to have large-signal LO power leaking back through the RF path and potentially radiating into the atmosphere. In every case, the measured results were similar to the simulated results. The total DC power dissipation for the mixer is 67 mW. The total die area, including the test baluns, is 2.0mm x 1.4mm. Excluding the baluns, the total area (including the pads for probe-testing) is approximately 1mm x 1.4mm.

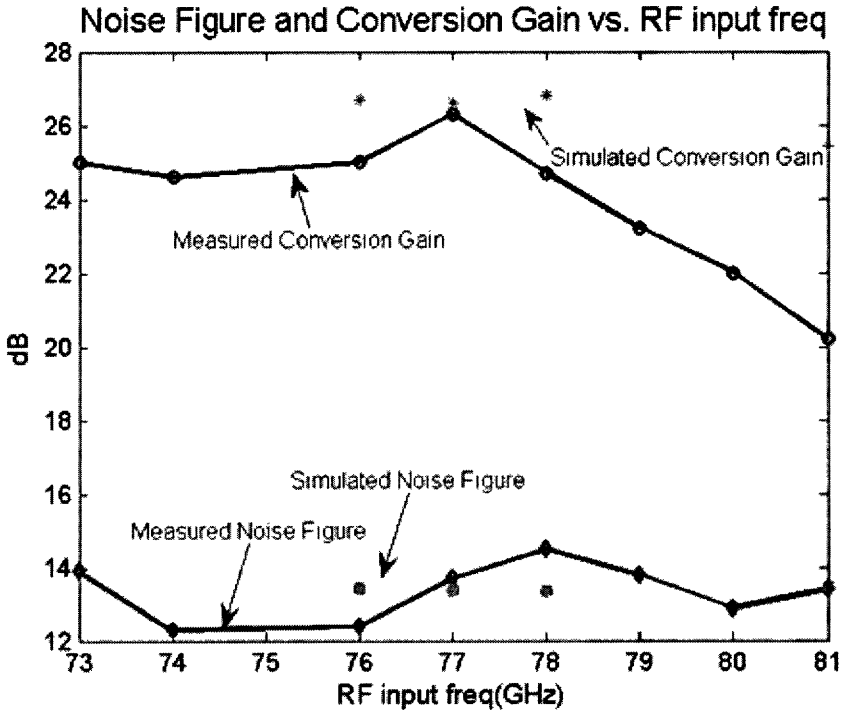

Figure 5-6: *77-GHz Mixer Simulated vs. Measured Noise Figure and Conversion Gain.*

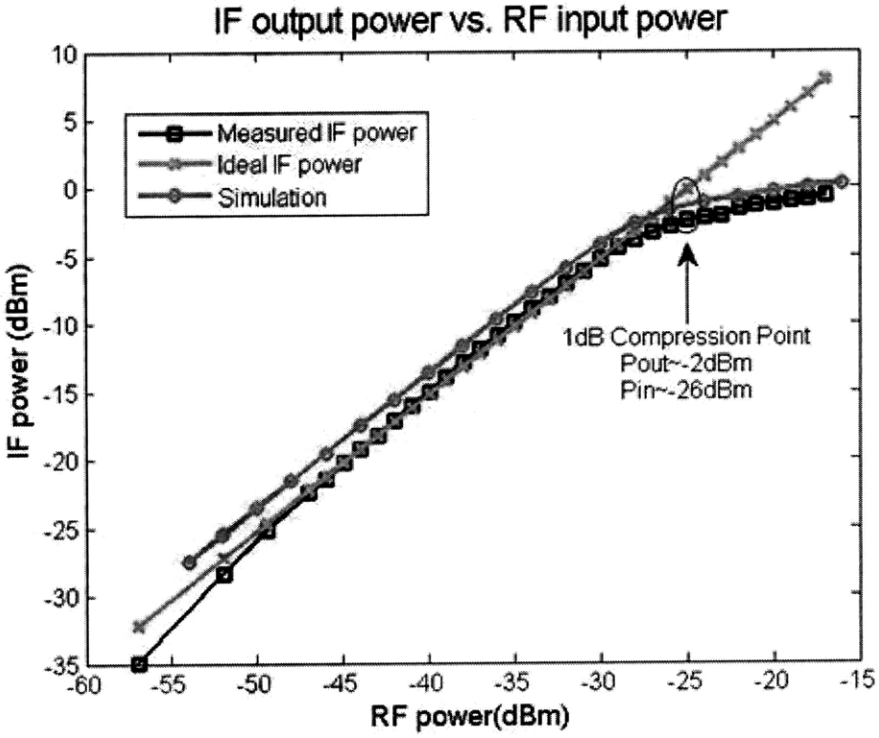

Figure 5-7: *77-GHz Mixer Simulated vs. Measured Input-Referred 1-dB Compression Point.*

5.4 Mixer Summary and Conclusions

A 73-81 GHz Double-Balanced Mixer and IF amplifier was presented, which achieved 20-26 dB conversion gain, 12-14 dB noise figure and -26 dB IP1dB. Table 5.1 summarizes the mixer performance parameters, including gain, NF, IP1dB, area, and DC Power Consumption.

Table 5.1: Mixer Performance Parameters Summary

Freq. (GHz)	Conv. Gain (dB)	Noise Figure (dB)	IP1dB (dBm)	P_{DC} mW	Area mm^2
73-81	20-26	12-14	-26	67	1 x 1.4

This mixer is a double-balanced Gilbert Cell configuration, which achieves greater than 40 dB LO-RF and LO-IF isolation, 67 mW DC Power consumption, and 1 x 1.4 mm^2 Area. All mixer measured parameters are sufficient for the specifications required for passive imaging in the 73-81 GHz frequency regime, and they compare favorably among other published results. The mixer die photo is shown in Figure 5-8.

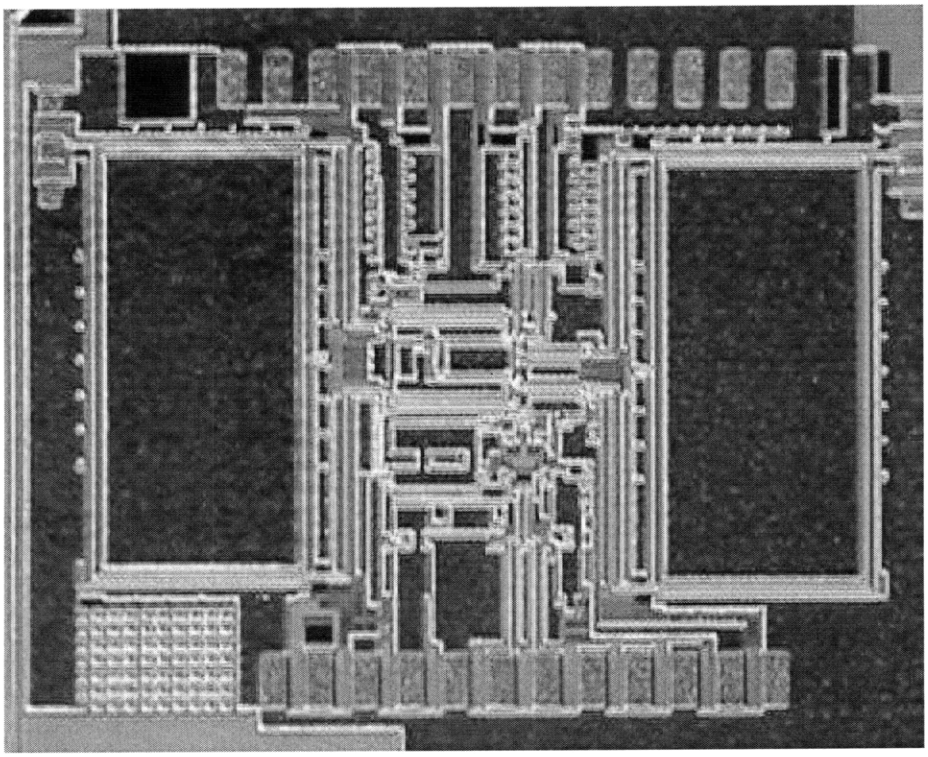

Figure 5-8: *77-GHz Mixer Die Photo.*

Chapter 6

Cross-Coupled Voltage-Controlled Oscillator

In virtually every transmit/receive system, a local oscillator signal is used via a frequency translator to downconvert the incoming RF signal into a usable intermediate or baseband frequency. This function can be provided externally by an LO source, or on-chip through the means of a standalone voltage controlled oscillator (VCO) or a VCO as part of a larger phase-locked loop system. Oscillators are inherently unstable and nonlinear systems, by definition, as the key characteristic of their operation involves positive feedback.

This thesis explores active millimeter-wave LC oscillators, which contain the key properties of requiring no RF input (only DC power is required), self-starting oscillation, providing sufficient amplification by active devices to compensate for resistive loss, and frequency selection by the LC resonator designed as part of the VCO core. In order to provide a clean, controllable and reliable LO signal, the VCO would make up an integral part of a phased-lock loop (PLL), which is currently being designed. The VCO in this work is used to demonstrate functionality with an on-chip LO, which eventually will be part of the PLL of [49].

Key design parameters considered are center frequency, output power, power consumption, phase noise and tuning range. Other theoretical considerations include start-up condition, long-term and short-term frequency stability.

The requirements set forth by the passive imaging application reflect the specifications required by the LO ports of the double-balanced mixer. Specifically, the mixer requires a minimum of -2 dBm of LO power, and an operating frequency of 72 GHz, such that the IF output frequency range is 1-9 GHz, given a 73-81 GHz RF input frequency range. It is desirable to have a reasonable amount of tuning range, in the case that the VCO exhibits a measured center frequency discrepancy from its desired value. This can be attained in a coarse manner by varying the power supplies, and in a fine manner by adjusting the varactor control voltages. Phase noise is also an important consideration for millimeter-wave passive imaging, in that it is desirable to have a clean, large-signal LO source to downconvert the RF energy. Given the available literature at the time of design, it was desirable to achieve better than -85 dBc/Hz phase noise, with the goal of further improving the phase noise of the internal LO signal with the use of a PLL.

6.1 VCO Fundamental Theory

The following section provides a tutorial to define fundamental VCO concepts, including the necessity of negative resistance and positive feedback to provide oscillation, as well as general phase noise theory. Also discussed in this section is the effect of phase noise on the overall receiver noise figure.

6.1.1 Negative Resistance and Positive Feedback

In general, the fundamental understanding of how an oscillator works requires understanding of the necessity of negative resistance and positive feedback. It is well known that negative resistance in a feedback system creates oscillation, as positive resistance will simply dampen an oscillation. Negative resistance, provided by active circuits, will negate the dissipative effects of parasitic resistance in the oscillator tank. [29], [2]. Figure 6-1 and the following analysis can more clearly explain the concept.

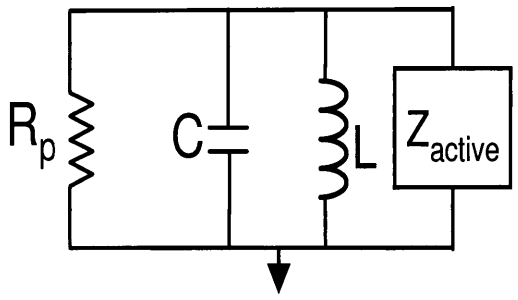

Figure 6-1: *LC Resonator Tank.*

If we assume that we have designed an LC frequency-selective tank, then at the resonant frequency, the LC tank will approximate an open circuit. Therefore, the total tank resistance we must compute at the resonant frequency is $R_p||R_{active}$, where R_{active} is the resistance looking into the oscillator core of the active devices (ie. negative resistance), and R_p is the parasitic resistance of the VCO core.

This yields:

$$R_p||R_{active} = \frac{R_p R_{active}}{R_p + R_{active}} \tag{6.1}$$

So, in order to maintain negative resistance, and thus start-up and sustain oscillation, a necessary condition is that:

$$|R_p| > |R_{active}| \tag{6.2}$$

This concept can also be illustrated using active devices with a frequency-selective LC tank. Figure 6-2 shows a BJT cross-coupled pair oscillator for which the input resistance is calculated to determine a sufficient parallel tank resistance value to start-up

and sustain oscillation. Since the magnitude of the signal at the collector of Q1 is equivalent to the magnitude of the signal at the collector of Q2, but opposite in sign, we can model the input resistance of each transistor as that of diode-connected transistors with a negative multiplier in the feedback path. This is illustrated conceptually in Figure 6-3.

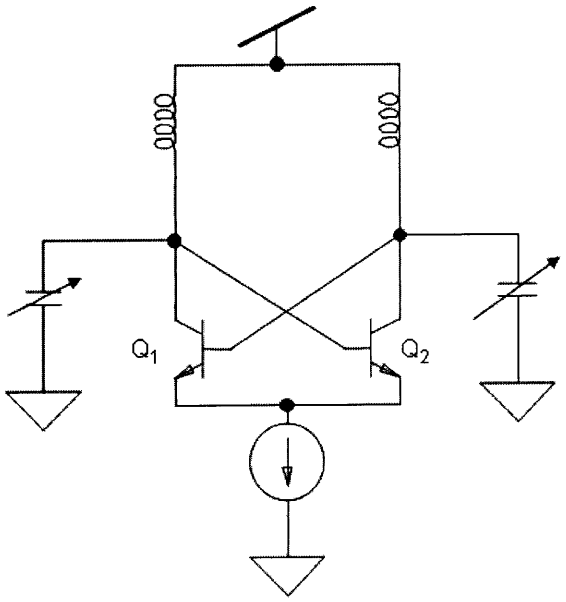

Figure 6-2: *BJT Cross-Coupled Pair with Frequency-Selective LC Tank.*

This figure can be simplified in terms of its pi model (shown in Figure 6-4, whereby we know that all DC voltages and currents are the same through Q_1 and Q_2):

$$g_{m1} = -g_{m2} \tag{6.3}$$

$$V_1 = -V_2 \tag{6.4}$$

$$V_1 - V_2 = 2V_1 = V_{tot} \tag{6.5}$$

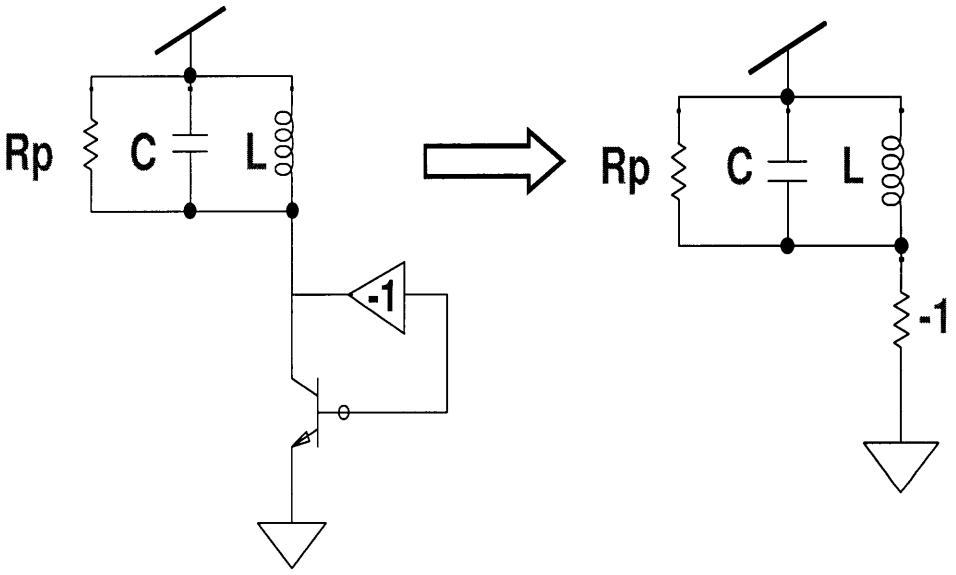

Figure 6-3: *Illustration of $-g_m$ resistance model for active BJT device. [2]*

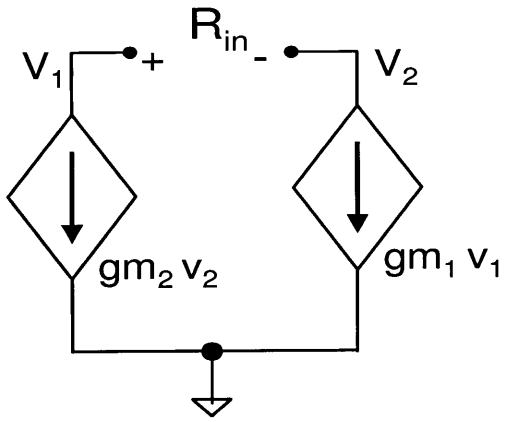

Figure 6-4: *Simplified BJT Cross-Coupled Pi Model for calculating input resistance.*

Thus, the total input resistance to the BJT cross-coupled pair is the ratio of the total voltage to the total current:

$$R_{in} = \frac{V_{tot}}{-g_{m2}} = \frac{-2}{g_m} \tag{6.6}$$

Given the analysis from equation 6.2, this means that R_p in the LC parallel tank must be greater than $\frac{2}{g_m}$ in order to start-up and sustain oscillation. In this case, then, the energy lost in R_p will be renewed by the active devices with every oscillation cycle.

One important concept to note is that, although this model implies constant positive feedback, this is not sustainable in an actual oscillator; in other words, the oscillation will not grow until the transistors blow up, as they are limited by the supply rails. Instead, there is a damping mechanism in place that limits the amplitude of the oscillation. This is set by the LC tank and the cutoff region of the active transistors. Once the collector of Q1 goes high, Q2 turns on and brings its collector output to a low ac value. The LC tank then continues the oscillation cycle, eventually bringing the collector of Q1 back down, thereby bringing down the base voltage of Q2, allowing the collector of Q2 to increase, and so on.

6.1.2 Phase Noise

Phase noise is an exceedingly important parameter of a VCO, in that it quantitatively describes carrier-to-noise ratio. It is essentially desirable to limit the thermal noise of the oscillator output, while maximizing the carrier (output) signal strength. Thermal noise causes frequency fluctuation, which in turn creates a spread in spectral content centered around the carrier frequency. We can determine the noise-to-signal ratio by noting that the signal energy E_{stored} in the VCO RLC tank is given by $E_{stored} = \frac{1}{2}CV^2$, such that the mean-square voltage signal is $\overline{V_{sig}^2} = \frac{E_{stored}}{C}$. By definition, the only source of noise in an RLC tank is the tank resistance, we can calculate the total mean-square noise voltage by integrating the thermal noise of the resistor over the

RLC tank noise bandwidth [29]:

$$\overline{V_n^2} = 4kTR \int |\frac{Z(f)}{R}|^2 df = \frac{4KTR}{4RC} = \frac{kT}{C} \tag{6.7}$$

The noise-to-signal ratio is defined as the ratio of the total mean-square noise voltage to the total mean-square signal voltage, which equates to the following:

$$\frac{N}{S} = \frac{kT}{E_{stored}} \tag{6.8}$$

In order to bring this equation into terms of the VCO tank quality factor Q, we can remember that the fundamental definition of Q is:

$$Q = \omega \frac{energy\ stored}{average\ power\ dissipated} = \frac{\omega E_{stored}}{P_{dissipated}} \tag{6.9}$$

This allows for the definition of carrier-to-noise ratio in terms of the oscillator Q:

$$\frac{S}{N} = \frac{QP_{dissipated}}{\omega kT} \tag{6.10}$$

This essentially summarizes mathematically what we expect for high signal-to-noise ratio: Higher Q and power dissipation lead to a stronger signal, while lower frequency and temperature decrease noise. Also, for a given oscillator Q, higher power dissipation will lead to improved phase noise.

In order to derive a quantitative calculation for oscillator phase noise, we first take into account the current noise across the oscillator tank, given by: $\frac{\overline{i_n^2}}{\Delta f} = 4kTG$. Next, we appproximate the effective impedance which is seen by the noise current source. This particular impedance will solely be that of an LC resonator, because in theory, the circuit provides just enough negative resistance to negate the positive tank resistance in order to produce an oscillation at the carrier frequency. Therefore, the impedance seen by the noise current source can be approximated given small displacements $\Delta\omega$ from the center frequency ω_o:

$$Z(\omega_o + \Delta\omega) \approx j\frac{\omega_o^2 L}{2\Delta\omega} \tag{6.11}$$

Note that the impedance seen by the current source is inductive, and as $\Delta\omega$ gets larger, the impedance looks less like an open circuit. We can also express this in terms of Q, since we also know that $Q = \frac{R}{\omega_o L}$. As such, the expression for the impedance of the oscillator tank becomes:

$$Z(\omega_o + \Delta\omega) \approx j\frac{\omega_o}{G2Q\Delta\omega} \tag{6.12}$$

To get an expression for the mean-square noise voltage, we simply take the mean-square current noise and multiply it by the squared magnitude of the tank impedance:

$$\frac{\overline{v_n^2}}{\Delta f} = \frac{\overline{i_n^2}}{\Delta f} * |Z|^2 = 4kTR\left(\frac{\omega_o}{2Q\Delta\omega}\right)^2 \tag{6.13}$$

This expression mathematically defines the mean-square voltage noise; however, most often it is more interesting to express this noise relative to the carrier strength. The mean-square voltage noise can be normalized to the mean-square carrier voltage, thus describing the noise ratio in decibels (or dBc/Hz). This is the most common way phase noise is expressed, and it is written as follows:

$$L(\Delta\omega) = 10\log\left(\frac{\overline{v_n^2}/\Delta f}{\overline{v_{sig}^2}}\right) = 10\log\frac{2kT}{P_{sig}}\left(\frac{\omega_o}{2Q\Delta\omega}\right)^2 \tag{6.14}$$

It is easily inferred that as the Q of the oscillator tank and the power of the signal increase, the phase noise improves. Also, as the frequency offset increases, the phase noise improves. This makes intuitive sense because the farther away from the carrier signal, the closer the measurement is to the noise floor. This is why it is very important to specify the frequency offset when reporting phase noise; otherwise the measurement is meaningless. Most often in millimeter-wave oscillator designs, the phase noise is reported at 1-MHz offset.

While this approximation of phase noise generally holds for small $\Delta\omega$, it is not consistent for increasing frequency offset. This aberration from the theoretical model is due to the presence of noisy active components in the oscillator and buffers, which cause the phase noise to flatten out into the noise floor rather than continuing to

decrease as a function of $\Delta\omega^2$. A more accurate model was presented by D.B. Leeson [50]. The theoretical model with Leeson's modifications is described in 6.15.

$$L(\Delta\omega) = 10\log\left(\frac{2FkT}{P_{sig}}\left(1+\left(\frac{\omega_o}{2Q\Delta\omega}\right)^2\right) * \left(1+\frac{\Delta\omega_{1/f^3}}{|\Delta\omega|}\right)\right) \tag{6.15}$$

6.1.3 LO Phase Noise and its effect on Receiver Performance

An important factor in determining the amount of phase noise acceptable by a VCO is how the overall noise will affect the receiver performance. While the LO signal and RF carrier signal are downconverted to a usable IF frequency, inevitably the oscillator noise is also downconverted, which appears in the IF band and affects the overall noise floor and thus the signal-to-noise ratio of the receiver.

Fortunately, for the millimeter-wave imaging regime of 77-GHz, there are no overt neighboring high-power RF signals that must be designed around. In fact, we can make the assumption that any neighboring signals would not be of any higher signal strength than that which we expect for our RF signal, or $-60\ dBm$. In this case, we can first determine the increase in the noise floor of the receiver due to its own noise figure. This is given in [51] as follows:

$$P_{nRx} = F - 174 \quad (dBm/Hz) \tag{6.16}$$

where the noise figure of the receiver the -174 dBm/Hz figure comes from the absolute noise floor in a one-Hertz bandwidth:

$$P_n = kTB \tag{6.17}$$

where $T = 290K$, $k = 1.38e-23\ m^2kgs^{-2}K^{-1}$, and $B = 1\ Hz$. This yields 4.002e-21 W, or -204 dB. Converting this to dBm yields $P_n = -174\ dBm$. This is also explained in [52].

The noise power due to the LO phase noise can be determined given a specified offset frequency, depending on where the RF carrier signal occurs. For example, we can calculate the noise power of the nearest -60 dBm RF carrier due to the an LO

phase noise of -100 dBc/Hz at 1 MHz offset as follows:

$$P_o = P_c + L(1MHz) = -160\ dBm/Hz \tag{6.18}$$

This sum at the given offset from the RF signal carrier yields a new apparent noise floor, which has 14 dB difference from the -174 dBm/Hz absolute noise floor of the receiver, and therefore a 14 dB increase in the receiver effective noise figure. In order to ensure that the VCO phase noise contributes essentially no noise to the receiver system at a given frequency offset, given an RF carrier power of -60 dBm, an LO phase noise of $\approx$ -114 dBc/Hz would be required.

6.2 Design and Characterization

The following section will detail the VCO design, including the cross coupled BJT core and buffers. The layout will also be discussed, as well as the full characterization scheme.

6.2.1 Topology- VCO Core

The topology chosen for the Millimeter-Wave VCO design was a cross-coupled BJT design. This topology provides negative resistance looking into the VCO core. Transistor sizes are chosen such that enough current can be pushed and pulled in order to provide sufficient output power at high millimeter-wave frequencies, while not adding excessive parasitic and inherent tank capacitance. The transistor sizes chosen for the VCO core were 2.75μm. The core design also incorporates independent base biasing in order to provide more autonomous control over the output VCO frequency (considering that extraneous factors such as parasitics and simulation model errors could occur and affect the output frequency). Capacitive feedback was also used in the core design, as it acted as a capacitive divider to enable substantially higher output frequency and output power. This will be explained more fully with simulation results in subsequent subsections.

The VCO core design is shown in Figure 6-5. Without the capacitive feedback, the circuit becomes that which is illustrated in Figure 6-2. One can determine the frequency of oscillation of this VCO tank without running a transient simulation by simply running an s-parameter simulation. The LC tank is calculated to resonate at a slightly higher frequency than the target output frequency, due to the extra capacitance in the VCO core. This capacitance is given by $C\pi = C_j + \tau g_m$, where C_j is the junction capacitance, determined by geometry, and τg_m is the transconductance, $\frac{I_c}{V_{th}}$, multiplied by the forward transit time.

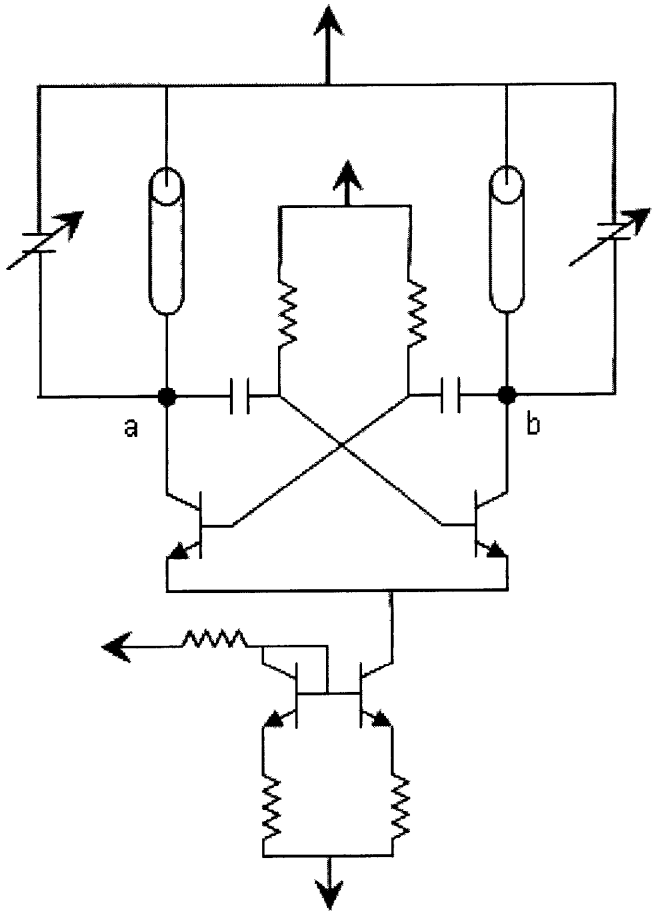

Figure 6-5: *VCO Core Design Schematic.*

The VCO includes a varactor in the LC tank, which provides a tank capacitance

ranging from $\approx$ 40fF to 95 fF, depending on the control voltage. This provides a nominal frequency tuning range, which can be widened or narrowed depending on the inductance value in the tank. A mid-range fixed capacitance value of 65fF was chosen for simulations of the standalone VCO core to illustrate how the capacitive feedback affects the overall output power and frequency, and ultimately, the phase noise of the oscillator.

When simulating the s-parameters of the VCO with a simulation port across the tank and core (between nodes a and b), the exact frequency at which the VCO will oscillate can be determined by analyzing the Smith Chart. We can see that the cross-coupled pair VCO without capacitive feedback oscillates at a much lower frequency, due to the high value of Cπ, which brings down the overall output frequency. The oscillation point of the tank can be found by observing the point on the Smith Chart at which the best impedance match is made (on the real impedance axis), with a trace cursor that indicates the impedance and frequency. It should be noted that this impedance match occurs for negative resistance, or outside of the Smith Chart's positive impedance circles. This is a clear indication of oscillation. Figure 6-6 shows the Smith Chart S11 for the cross-coupled pair without capacitive feedback, and Figure 6-7 shows the Smith Chart S11 for the cross-coupled pair with capacitive feedback.

It should be noted that the capacitive feedback provides an output frequency difference of 30 GHz higher, due to the capacitive division of Cπ. In this particular schematic, the BJTs are 2.75μm with 5mA DC bias current through each core transistor, and 10mA DC tail current. Cπ is 80fF at the DC bias point of 5mA, but this approximately doubles as the entire tail current is pushed through each transistor in the core during oscillation, as Cπ increases as a function of collector current. The varactor capacitance has been set to a fixed 65 fF, contributing to a total of $\approx$ 229 fF of capacitance. This, combined with 46pH of inductance provided by the 100 μm long transmission line inductor, corresponds to a theoretical resonant frequency of $\approx$ 49 GHz, given $f = \frac{1}{2\pi\sqrt{LC}}$. Simulation of the LC tank with an ideal capacitance of 229 fF and a 100 μm, 8μm thick microstrip inductor approximating 46 pH of inductance

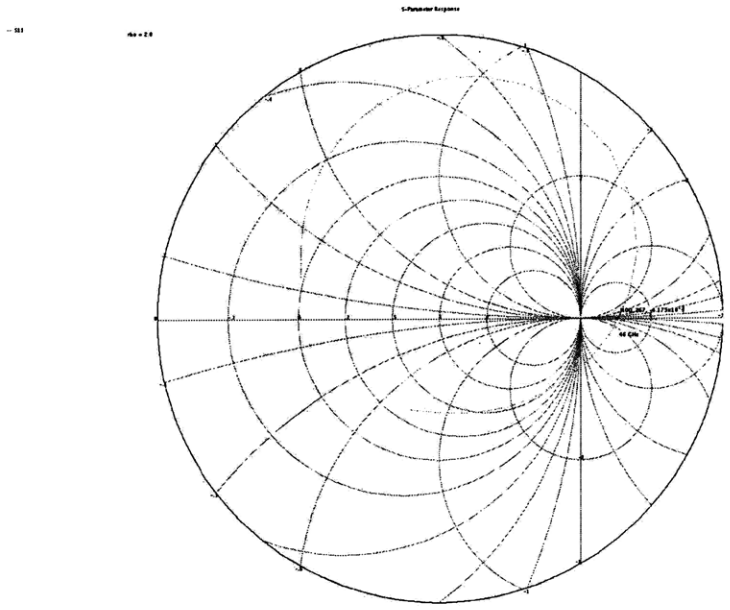

Figure 6-6: *VCO Core S-parameter response without Capacitive Feedback.*

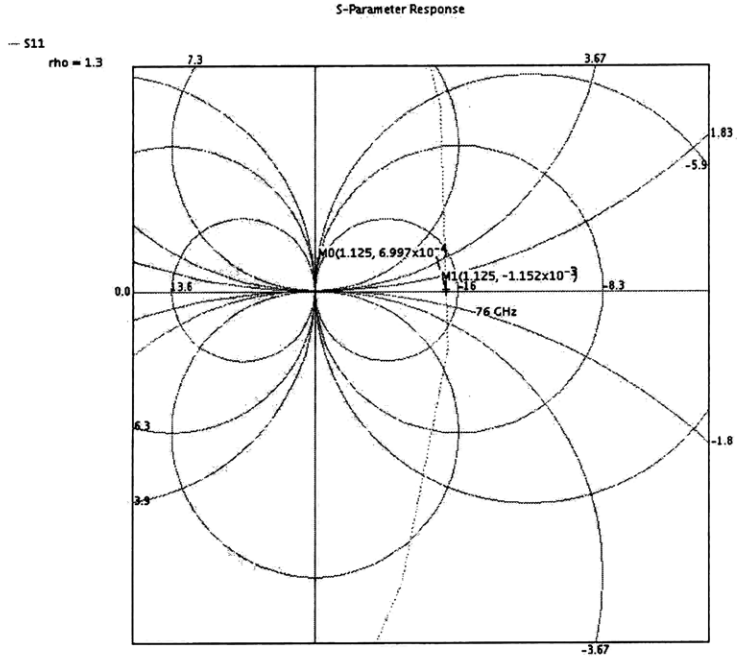

Figure 6-7: *VCO Core S-parameter response with Capacitive Feedback.*

yields approximately the same output frequency at $\approx$ 47 GHz, showing very close theoretical and simulated agreement.

Once the theoretical and simulated output frequency of the VCO core has been verified based on inductance, transistor and core capacitance, it is important to check that the capacitive division is the source of the frequency increase. The feedback capacitance should ideally be very small, so as to dominate the overall value of capacitance seen by the oscillator. A capacitance value of 15 fF is chosen, which is too small to create with MIM capacitors. This is resolved in layout using the M3-M4 metal layers, which have the smallest amount of spacing between them, thereby providing the maximum amount of capacitance per unit area of metal. A feedback capacitance value of 15 fF will yield a total capacitance (seen as Cπ) of $\approx$ 13.7 fF, which approximately doubles as twice the current flows through the BJT. This is added to the varactor capacitance (in this case, 65 fF), for a final output frequency value of $\approx$ 76 GHz. Both output frequencies can be verified in simulation with simple S-parameter Smith Chart simulation, making simulation match closely to theory.

Another advantage of capacitive division is that the output power is significantly improved. In this particular simulation, we see an improvement of 12 dB in output power with the addition of the feedback capacitors; however, this is not entirely reflective of the actual power improvement, as the LC tank is tuned for 75 GHz, and the bias current is also optimized for operation in that frequency region. However, the output voltage swing for a VCO core with no capacitive feedback is on the order of 100's of millivolts, whereas the output voltage swing for a VCO core with capacitive feedback is on the order of volts. The feedback capacitors enable a much higher output voltage swing without saturating the base-collector junction. The improvement in output power translates to an improvement in phase noise, as phase noise is inverse-logarithmically proportional to output power. The full VCO schematic is shown in Figure 6-8.

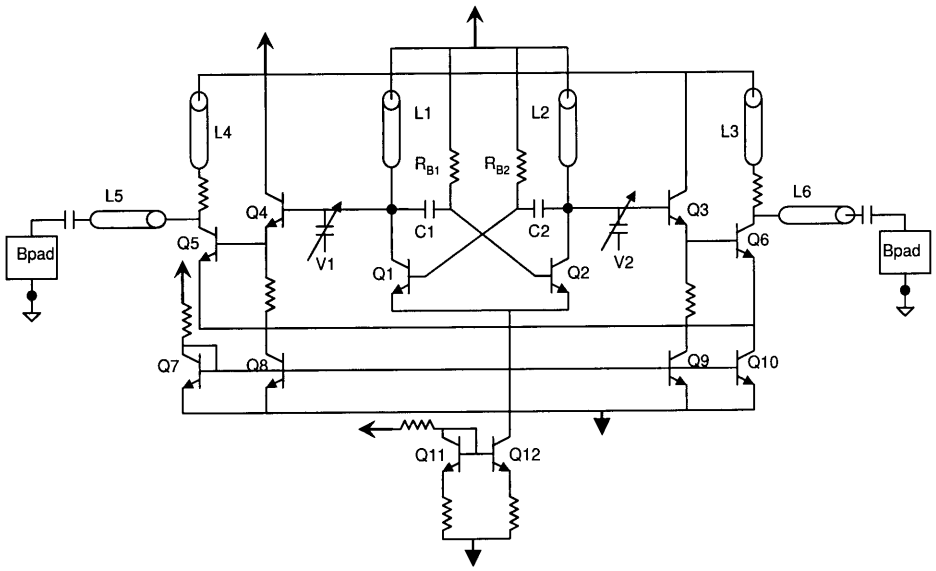

Figure 6-8: *VCO Full Schematic.*

6.2.2 Topology- VCO Buffers

The VCO output buffers are comprised of emitter followers sized and biased for maximum output voltage swing, followed by an emitter-coupled pair with inductive peaking to maximize the output power to a 50-ohm load. This technique is known as power-matching, which is used for large-signal outputs in oscillator and power amplifier design [29]. These also resonate with the junction capacitance to provide a real load impedance at the output frequency. The output buffers are independently DC biased from the VCO core for better output control. The resistors at the output of the emitter followers are used to keep the DC level at the current source collectors consistent with that of the emitter-coupled pair.

The series transmission lines in series with the AC coupling capacitor were necessary to route the differential VCO outputs to the inputs of the double-balanced mixer, which were approximately 150 μm apart. While this does add a nominal amount of loss in output power, it does not significantly affect the output frequency of the VCO.

6.2.3 Layout

The VCO is a very layout-sensitive circuit, due to excess parasitics and asymmetries which can exist. In fact, all circuit elements operating in the millimeter-wave regime are sensitive in this way. In order to limit common-mode noise, the layout was made as symmetrical as possible. The VCO core layout is illustrated in Figure 6-9, and the full layout is illustrated in Figure 6-10. The feedback capacitors in the VCO core are highlighted by a box in the center of the VCO core layout, implemented in M3 and M4 because of the very small relative spacing between the two metal layers. The LC tank inductors (also highlighted above the capacitors) are implemented with the two 100-μm long microstrip transmission lines which bend and connect at the center of the core to vdd. The series transmission lines extending to the output at the bondpads are used simply to route the VCO output to the mixer LO input terminals, as explained above. The large microstrip transmission lines which envelope the VCO core and bend to connect to vdd are the peaking inductors seen in the output buffer

of the VCO schematic. The total chip size is 690 μm x 650 μm, including bondpads. The size reduces to approximately 375 μm x 550 μm when the LO output bondpads are not in use.

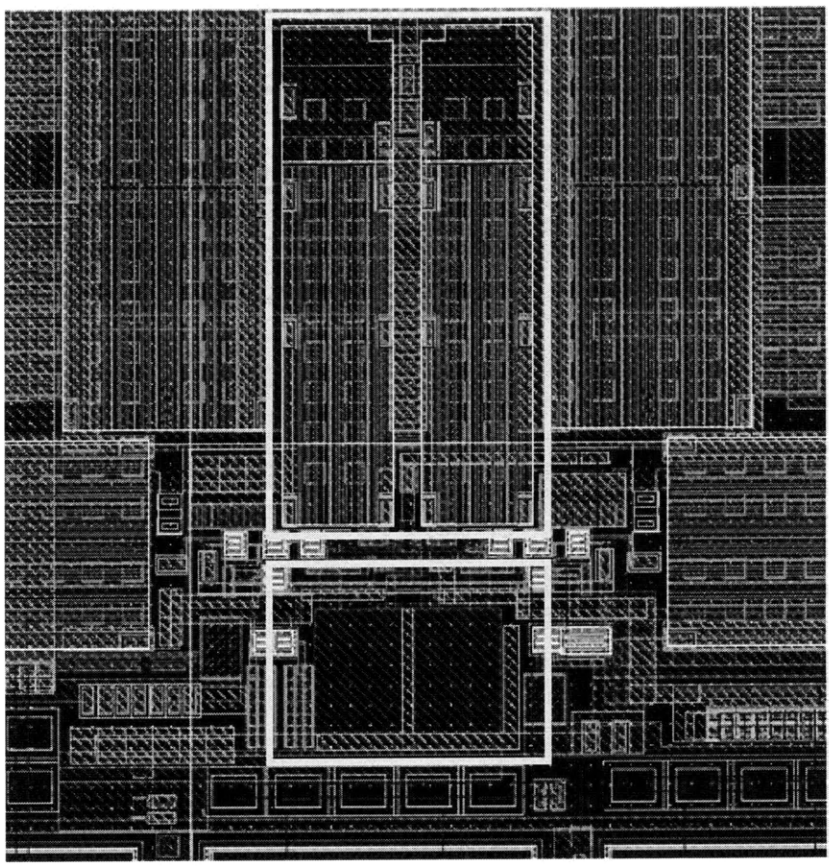

Figure 6-9: *VCO Core Layout, illustrating the feedback capacitors and symmetry.*

6.2.4 Testing Methodology

The VCO was tested using on-chip probing at MIT's Lincoln Laboratory with Infinity GSG probes rated up to 110-GHz. The output power was measured on both an Agilent spectrum analyzer and then verified by a W-band power meter. All power loss by external components was separately measured and calibrated out, including that of the probes, adapters, and mm-gore cables.

The VCO phase noise was measured on an Agilent Spectrum Analyzer using

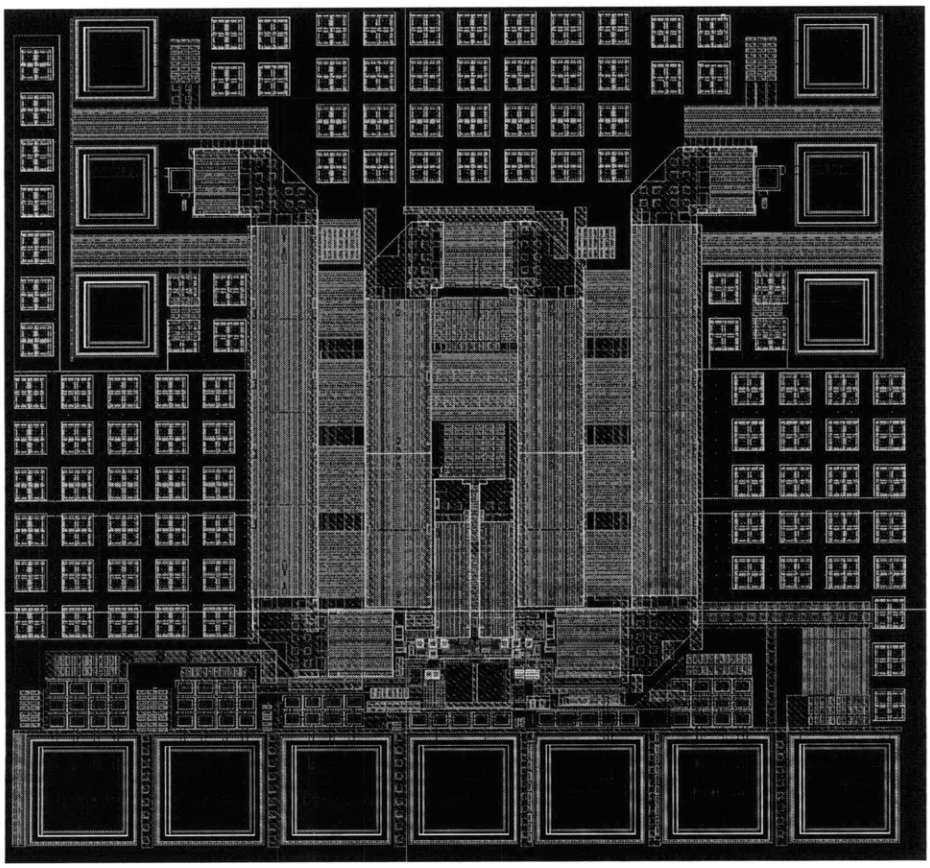

Figure 6-10: *VCO Breakout Layout.*

a resolution bandwidth of 100-KHz (which corresponds to an extra $10\log 100e3 = 50dB$) of phase noise to be subtracted from the result measured by the delta marker on the spectrum analyzer. The phase noise was measured at 1-MHz offset from the center frequency, which is the most typically reported phase noise offset measurement in the mm-wave literature. The method used for capturing the phase noise was an injection-locking method, whereby an external signal was injected into the VCO through one of the outputs to "lock" the VCO output signal and more accurately measure the phase noise produced by the VCO alone.

6.3 VCO Summary and Conclusions

The VCO included in the receiver was designed for operation at 72-GHz, to provide an IF of 1-9 GHz for an RF input of 73-81 GHz. Two VCO breakouts were tested; one was designed for higher frequency operation and achieved -86 dBc/Hz phase noise at 75 GHz, and the other performed at 70.5 GHz with -93 dBc/Hz phase noise at 1 MHz offset from the carrier. Both were tunable by about 3 GHz. The VCO integrated in the receiver used the same layout as the VCO which achieved an output frequency of 70.5 GHz (standalone), but operated at a center frequency of approximately 72 GHz, as inferred from receiver measurements with a fixed RF frequency. The reason for the shift to a higher frequency was likely due to the elimination of the bondpads (as well as the inductive probes used to measure the standalone VCO), which loaded the VCO output and brought the operating frequency down. The on-chip LO phase noise is assumed to be similar to that of the lower frequency VCO tested, since its equivalent layout was used in the integrated receiver. Figures 6-11 and 6-12 illustrate the VCO phase noise measured at an output frequency of 70 GHz and 75 GHz, respectively.

The noise power and overall effect on receiver noise figure due to the LO phase noise is also determined. Since we are interested in an IF frequency of 1-9 GHz, the frequency offset of the RF carrier from the LO would essentially be 1 GHz, where the VCO achieves $\approx$ 112 dBc/Hz. Therefore, we can calculate the noise power of the

nearest RF carrier due to the LO phase noise at 1 GHz as follows:

$$P_o = P_c + L(1GHz) = -60 + (-112) = -172\ dBm/Hz \tag{6.19}$$

This sum at the given offset from the RF signal carrier yields a new apparent noise floor with a 2 dB difference from the -174 dBm/Hz absolute noise floor of the receiver, and therefore a 2 dB increase in the receiver effective noise figure. In order to ensure that the VCO phase noise contributes essentially no noise to the receiver system at a given frequency offset, given an RF carrier power of -60 dBm, an LO phase noise of $\approx$ -114 dBc/Hz would be required at that frequency offset, as mentioned previously.

For the case of a 1 MHz offset (where the phase noise of the VCO was specified to achieve -93 dBc/Hz), the RF signal carrier yields a new apparent noise floor of 21 dB difference from the -174 dBm/Hz absolute noise floor of the receiver, and a 12 dB difference from the noise floor of the receiver, P_{nRx}, due to its own noise figure. If we were concerned about carriers within 1 MHz of the LO frequency, the VCO required performance of -114 dBc/Hz would be far greater than its current measured performance of -93 dBc/Hz in order to ensure that it would contribute essentially no noise to the receiver system. This is indeed achievable if the VCO is phase-locked in a PLL system; also, the VCO phase noise can be improved by several means, including mitigating parasitics and using smaller NMOS varactors.

The output power for the VCOs were in the approximate range of -2 to +2 dBm throughout the frequency of operation, as measured on a W-band power sensor. Power dissipation for the VCO is 73 mW, and the area is 700 μm x 550 μm. The VCO Die Photo is illustrated in Figure 6-13.

Table 6.1 summarizes the VCO performance parameters.

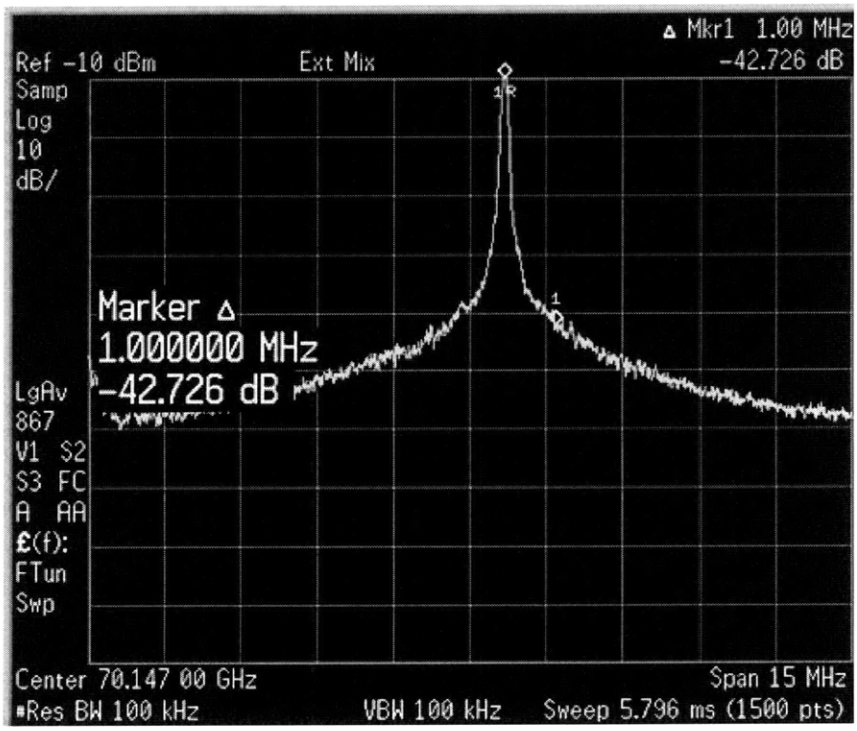

Figure 6-11: *VCO Phase Noise Measurement at 70.1 GHz.*

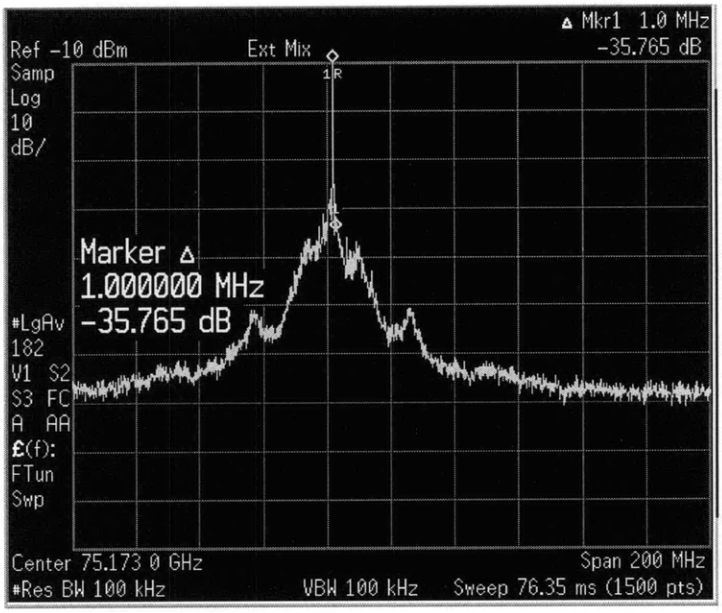

Figure 6-12: *VCO Phase Noise Measurement at 75 GHz.*

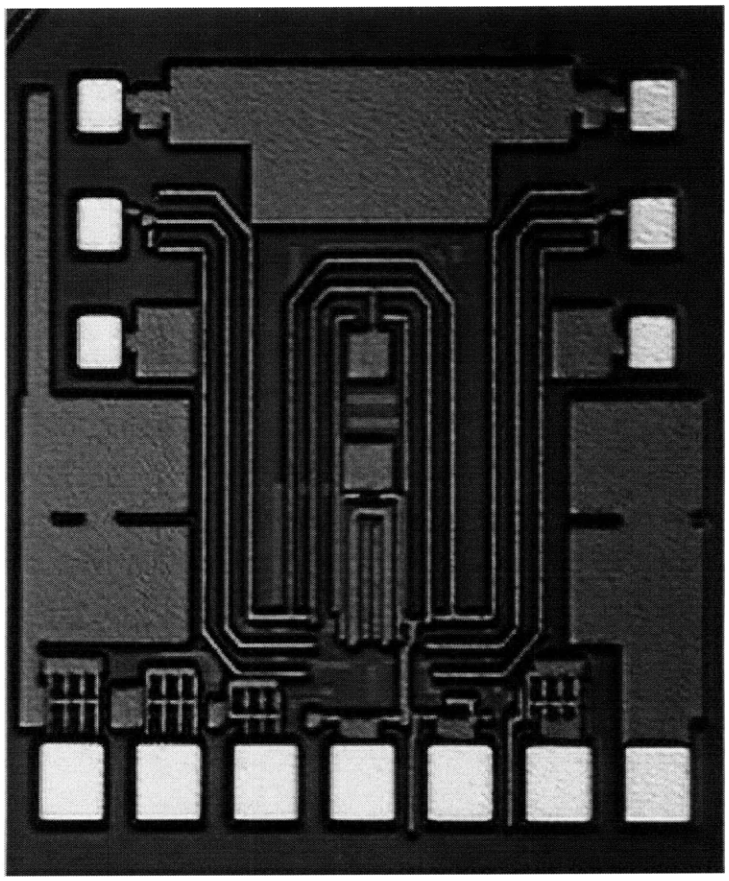

Figure 6-13: *VCO Die Photo.*

Table 6.1: VCO Performance Parameters Table

Center Freq. (GHz)	Output Power (dBm)	Phase Noise (dBc/Hz) @ 1 MHz	Tuning Range	P_{DC} (mW)	Area (mm^2)
70.5	-2 $\rightarrow$ +1.5	-93	3 GHz	73	.385
75	-2 $\rightarrow$ +1.5	-86	3 GHz	73	.385

Chapter 7

Conclusions

7.1 Overall Impact

The overarching highlight of this work is the integration of a high efficiency antenna onto a high performance receiver front end while preserving the overall performance with minimal loss. This scheme improves overall receiver sensitivity. Also, this method simplifies the overall packaging scheme which eliminates W-band interconnections, requiring only connections to the significantly lower IF frequency band. Overall, this work also sheds light on the importance of antenna and circuit co-design by emphasizing the critical contribution that the antenna makes to overall receiver noise figure.

7.2 Thesis Summary

Fully characterized 77-GHz and 94-GHz front end receivers have been presented for millimeter-wave passive imaging, achieving the highest gains and lowest noise figures reported for silicon-based receivers in these frequency regimes, with wideband performance. Wideband Millimeter-Wave antennas were also designed, fabricated and fully characterized using a unique mm-wave measurement technique for GSG probe stations. The unpackaged antenna performance yields maximum gains ranging from 10-13 dB from 70-100 GHz, with greater than 90% efficiency. Finally, most notable

about this work is the co-design and flip-chip assembly of these integrated wideband antennas that achieve excellent radiation efficiency, bandwidth and gain. This flip-chip method proves to be the lowest-loss integration method to date, yielding an average of 0.5-1dB of loss overall, for a typical package efficiency of 80-90%. When compared to systems which implement on-chip antennas, these results prove to be far superior in overall receiver performance, namely because on-chip antenna efficiency is so poor (usually $< 10\%$ in most reported cases [12]- [23]). Poor antenna efficiency directly impacts a receiver's noise figure and gain performance, and unfortunately, these results are typically not reported inclusively when characterizing a receiver's overall performance.

The 77-GHz Front End Receiver achieves 46 dB max conversion gain, 6.5-10 dB noise figure, OP1dB of +2 dBm and DC power dissipation of 122 mW, while the 94-GHz receiver achieves 47 dB max conversion gain, 7-12.5 dB noise figure, and DC power dissipation of 120 mW. The standalone circuit blocks which make up the RF front end systems also individually achieve good performance. The 77-GHz LNA achieves 4.9-6.0 dB NF, 18-26 dB gain, and S11, S22 of -13.0 and -12.8 dB, respectively. The Double-Balanced Mixer achieves 12-14 dB NF, 20-26 dB conversion gain and -26dBm P1dB (input-referred). The VCO achieves output power from -2 to 0 dBm with phase noise of -93 dBc/Hz at 72 GHz, and 3 GHz tuning range. The 94-GHz LNA achieves 22-dB max gain, 7.0 dB NF, -25 dB and -10 dB S11 and S22, respectively. This LNA also exhibits excellent Ultra-Wideband performance, achieving >10 dB gain from 40-100 GHz.

Table 7.1, displays a State-of-the-Art Comparison of silicon-based receivers (including some individual receiver components) in both SiGe and CMOS technologies. A graphical State-of-the-Art Comparison is illustrated in Figure 7-1, highlighting noise figure vs. gain performance.

Table 7.1: State-of-The-Art Comparisons of Silicon-Based Receivers and/or Receiver Components

Ref.	*Tech.*	*RX Integ. Level*	*Freq. Range (GHz)*	*RX Max Gain (dB)*	*Noise Fig. (dB)*	*IP1dB (dBm)*	*P_{DC} mW*	*Area mm^2*
[53]	.13 μm SiGe	LNA/Mix/ LO Buff	75-86	28	11	-16	1072	1
[54]	.13 μm SiGe	LNA/Mix/ IF Amp/VCO	81-90	36	Not Meas.	-33	274	.135
[55]	SiGe	LNA/Mix/ Balun	75.5-77.5	30	11.5	-26	440	1.16
[56]	SiGe	LNA/Mix/ IF Amp/VCO	77-79	25.6	9-10.5	-24	240	1.17
[57]	65-nm CMOS	LNA/Mix/ IF Buffer	80-84	12	9-10	-13	94	.30
[8]-[58]	.13 μm SiGe	LNA/Mix/ IF Amp/VCO	77-83	37	8-10	-27.5	161	2.25
[59]	SiGe	Trans.: VCO/Mix	150-170	-23.5	Not Meas.	-1*	295	.455
[59]	SiGe	LNA	140/156	17	Not Meas.	-1*	112	.08
[60] [61]	SiGe	LNA	77-84	17	5.6 (sim)	-17	14.4	.54
[60]	SiGe	Mixer	73-81	6	14.9	Not Rep.	Not Rep.	$\approx$2.1**
[62]	SiGe	LNA/Mix/ VCO	77-79	21.7	10.2 (sim)	Not Rep.	595	1.26
[63]	45-nm CMOS	Mix/ IF Amp	109-112	19.5	13.2	Not Rep.	Not Rep.	Not Rep.
[64]	130-nm CMOS	LNA	51-65	12	8.8	2.0*	54	Not Rep.
[65]	65-nm CMOS	LNA/Mix IF Amp	100-140	-15	Not Rep.	-12 (LNA IP1dB)	54	.406 Rep.
This Work	.13 μm SiGe	LNA/Mix/ IF Amp	73-81	46	6.5-10.5	-38	122	1.7
This Work	.13 μm SiGe	LNA/Mix/ IF Amp	91-99	46.5	7-12.5	-39	120	1.6

*(OP1dB)

**Not Directly Reported; size is inferred from full chip photo.

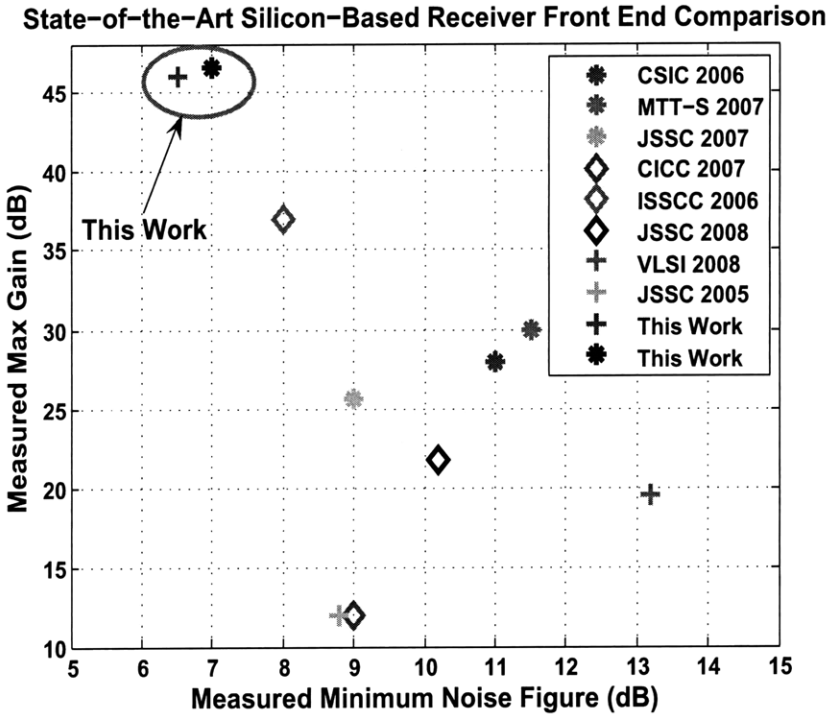

Figure 7-1: *State-of-the-Art Graphical Comparison: Noise Figure vs. Gain.*

7.3 Future Work

Several key areas investigated in this thesis have great potential for improvement and further exploration. These areas include (but are certainly not limited to) packaging methods, noise figure improvement, reliable LO generation, and improvement of parasitic modeling. While this work contributed towards overall packaging methods by eliminating the need for external W-band connections, an overall packaging scheme still presents a substantial challenge in that it is necessary to package the full chip including a low-loss IF connection with minimally intrusive effects to the antenna. The method that was used in this work for chip characterization was on-chip prob-

ing; however, this method may soon be replaced by full packages in order to realize a functional prototype.

Another key area still requiring improvement is the overall receiver noise figure, as this directly affects the receiver sensitivity (as defined in Chapter 2: $\Delta T \approx (T_A + T_N) * \sqrt{\frac{1}{BW\zeta}}$). When comparing the state-of-the-art MMW silicon-based receiver results to other systems, including discrete receivers and III-V receivers, silicon-based systems still do not exhibit the lowest noise figures. This largely is due to inherent noise in the silicon-based substrates, but there is still room for overall improvement in silicon-based systems. As mentioned in Chapter 2, noise figure mitigation can be achieved with the implementation of image-rejection schemes, such as an image-reject bandpass filter. However, this is not a trivial design, as it requires filters with very low insertion loss and exact impedance matching about the image band in order to provide effective noise mitigation.

Reliable local oscillator generation is imperative in order to provide a low phase noise modulation signal to the receiver front end. On-chip LO generation requires a full on-chip PLL, which also presents significant design challenges in the MMW regime, due to the complexity of the system. While the VCO is an essential component of the PLL, also critical is the careful design of each element in the loop that interacts with the VCO and an understanding of this interaction on a thorough level. Designing for test is also nontrivial, because the placement of a bondpad and probe on a critical node can disrupt the PLL performance.

Finally, improvement of parasitic modeling is a large area that still requires work in the MMW regime. This is largely because most low frequency circuit design does not necessitate parasitic extraction of inductance. However, with increasing frequency, routing wires represent larger values of parasitic inductance which can significantly alter impedance matching parameters.

Aside from the general concepts described, there are countless opportunities for impactful influences and improvements in MMW design, including expanding operating frequencies, improving test equipment, improving test methods and characterization methods, expanding integration levels and system complexity, and identifying

new and useful applications, to name a few. With further advancement of silicon technology and component modeling, lower noise figures, higher system complexities and packaging developments will be achievable. These further advancements will certainly make silicon-based MMW systems an even more viable and competitive technology than they have already proven to be.

Appendix A

A.1 Antenna Gain vs. Angle: Azimuth Plane

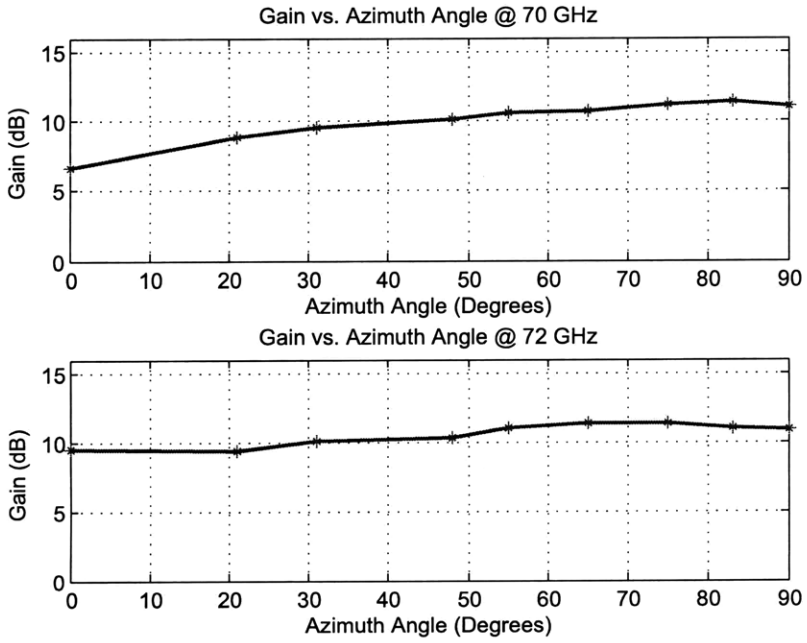

Figure A-1: *Antenna Gain vs. Angle: 70 GHz and 72 GHz, Azimuth Plane.*

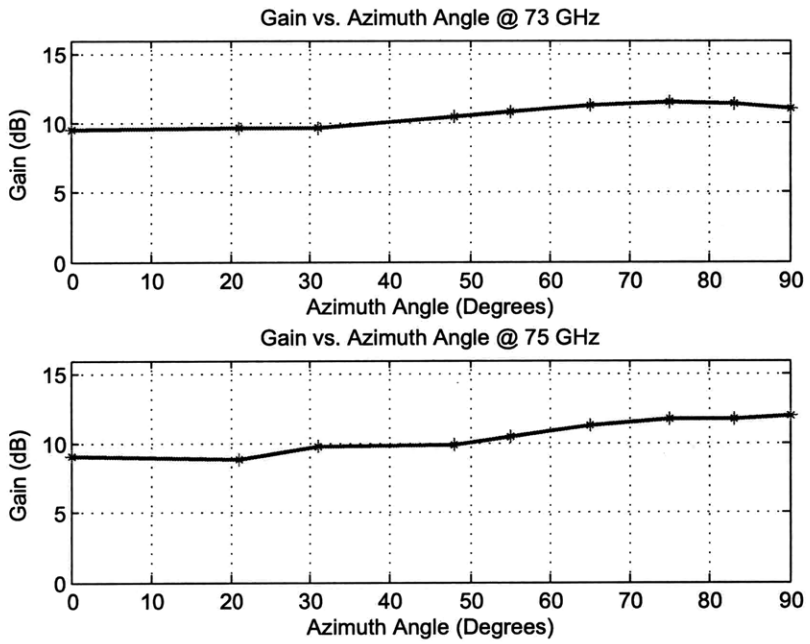

Figure A-2: *Antenna Gain vs. Angle: 73 GHz and 75 GHz, Azimuth Plane.*

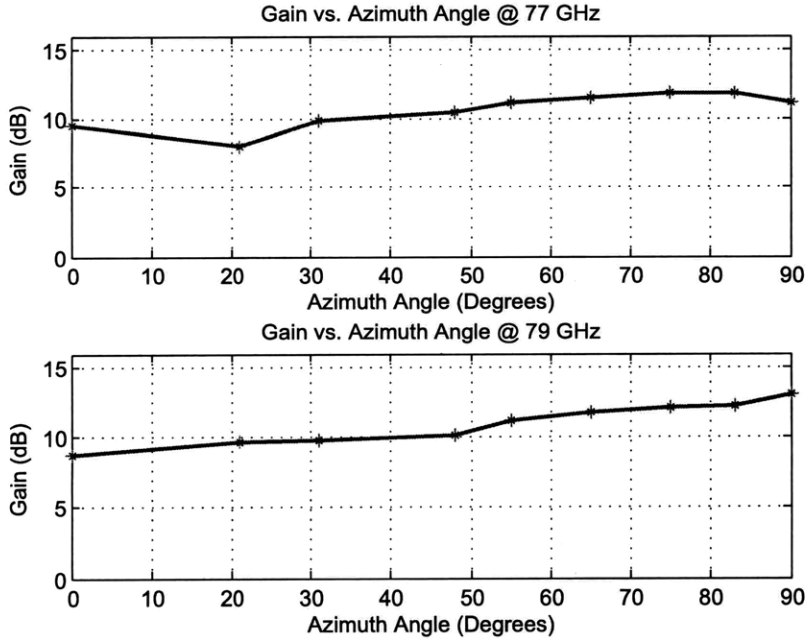

Figure A-3: *Antenna Gain vs. Angle: 77 GHz and 79 GHz, Azimuth Plane.*

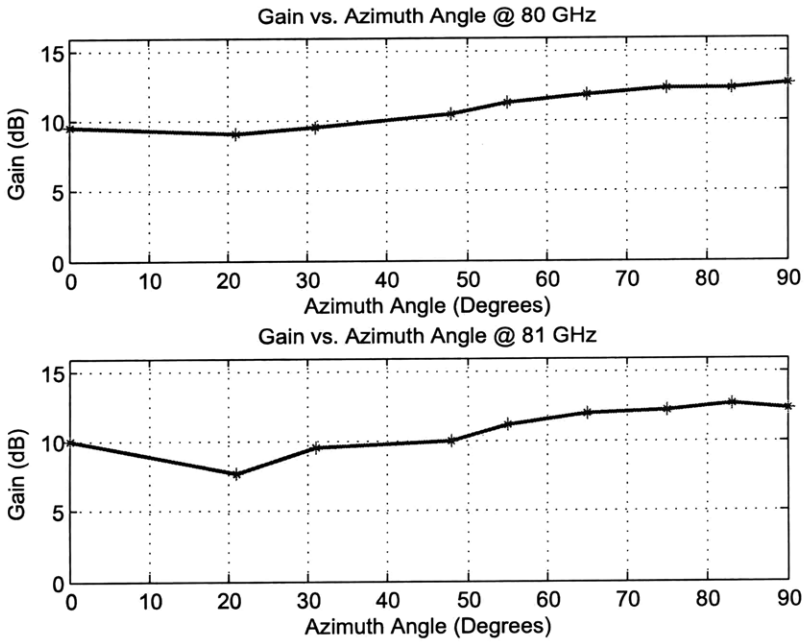

Figure A-4: *Antenna Gain vs. Angle: 80 GHz and 81 GHz, Azimuth Plane.*

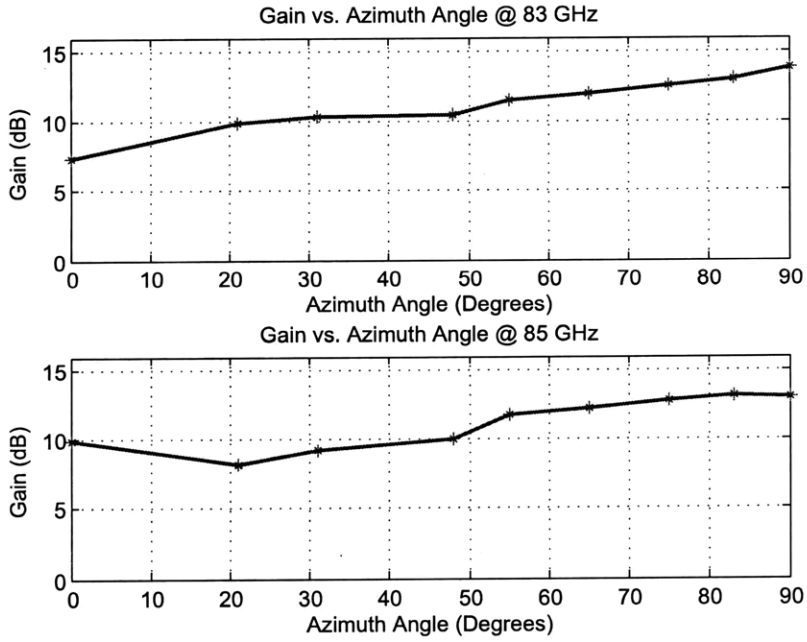

Figure A-5: *Antenna Gain vs. Angle: 83 GHz and 85 GHz, Azimuth Plane.*

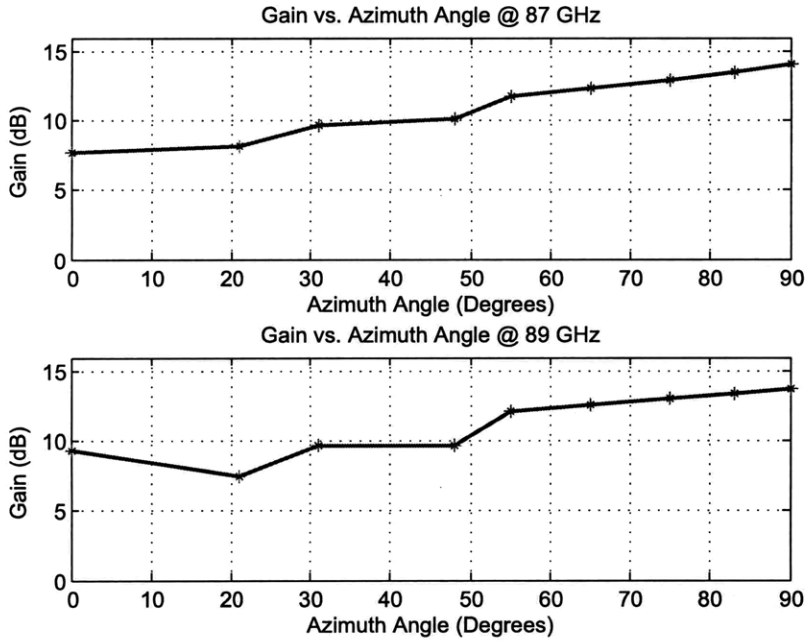

Figure A-6: *Antenna Gain vs. Angle: 87 GHz and 89 GHz, Azimuth Plane.*

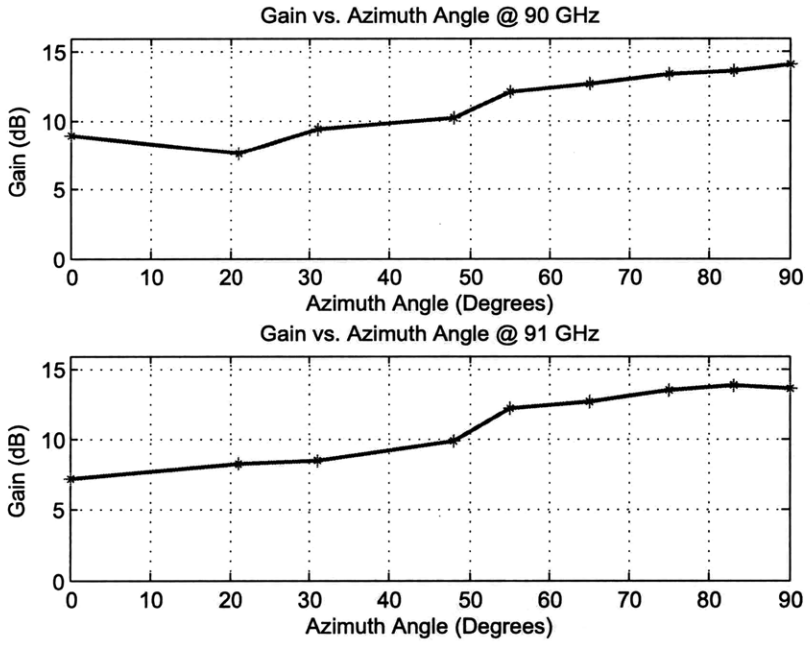

Figure A-7: *Antenna Gain vs. Angle: 90 GHz and 91 GHz, Azimuth Plane.*

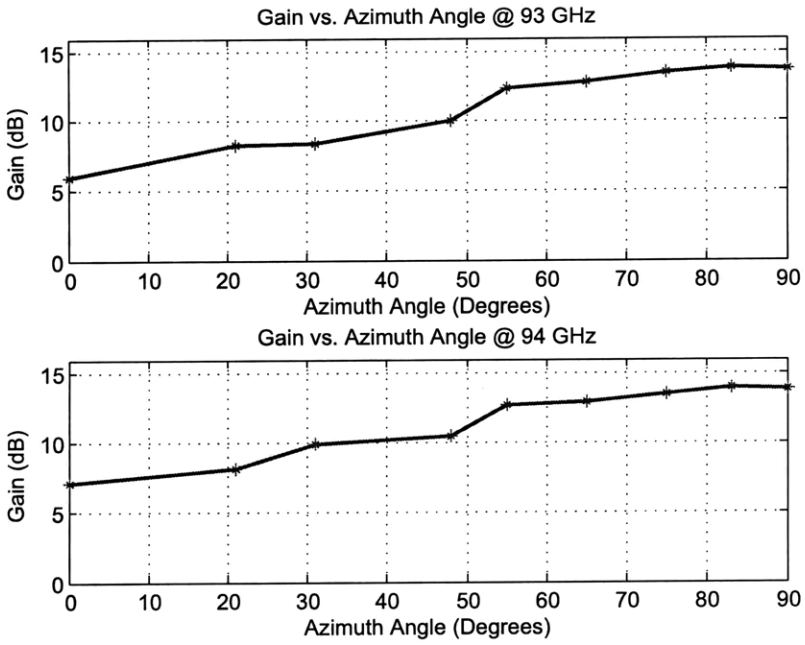

Figure A-8: *Antenna Gain vs. Angle: 93 GHz and 94 GHz, Azimuth Plane.*

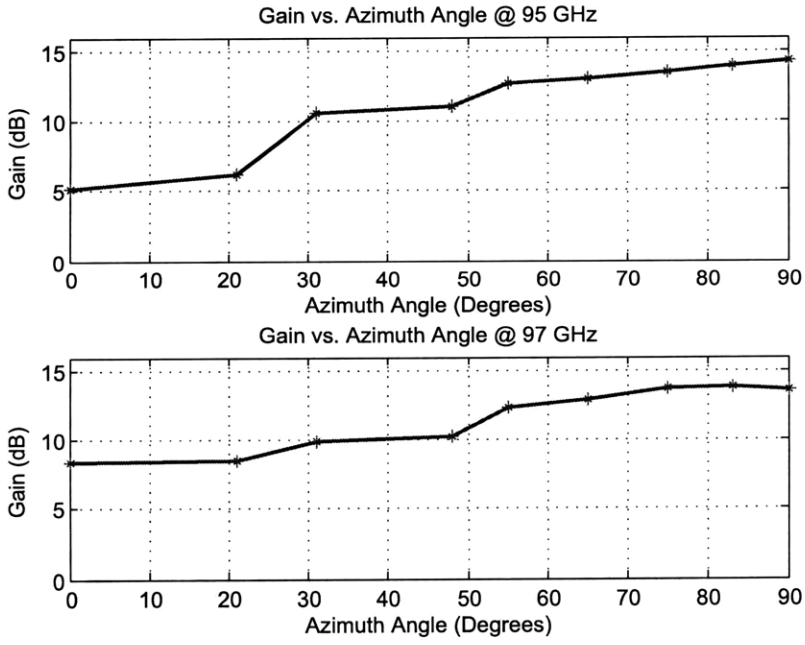

Figure A-9: *Antenna Gain vs. Angle: 95 GHz and 97 GHz, Azimuth Plane.*

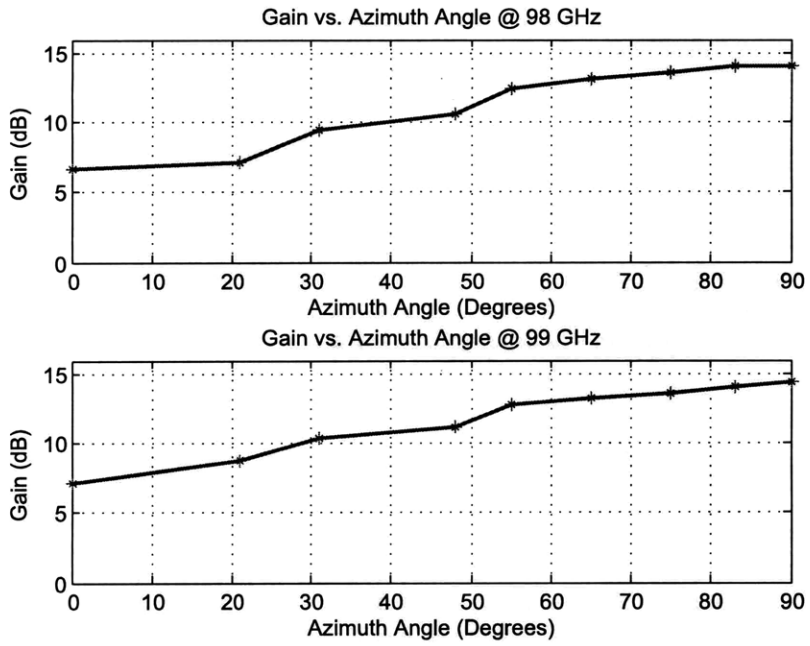

Figure A-10: *Antenna Gain vs. Angle: 98 GHz and 99 GHz, Azimuth Plane.*

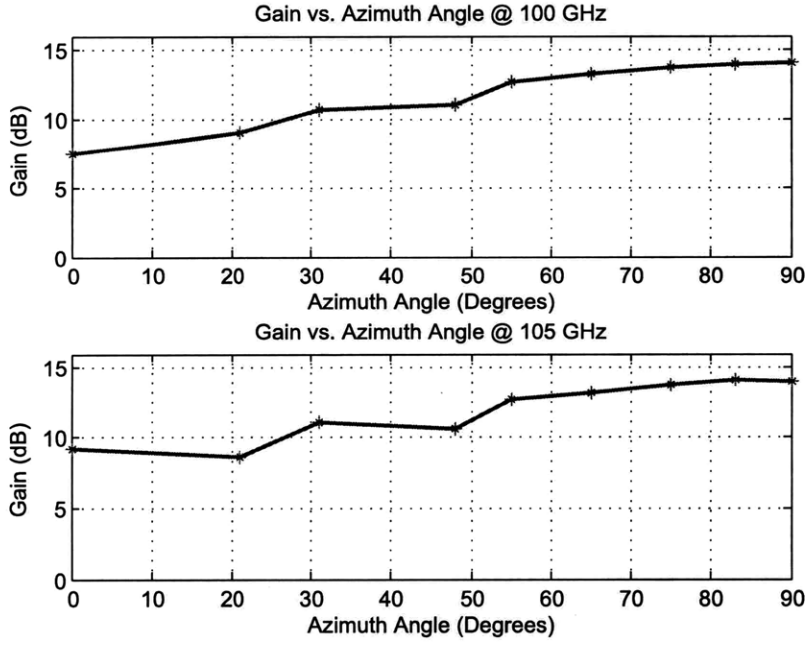

Figure A-11: *Antenna Gain vs. Angle: 100 GHz and 105 GHz, Azimuth Plane.*

Appendix B

B.1 Antenna Gain vs. Angle: Elevation Plane

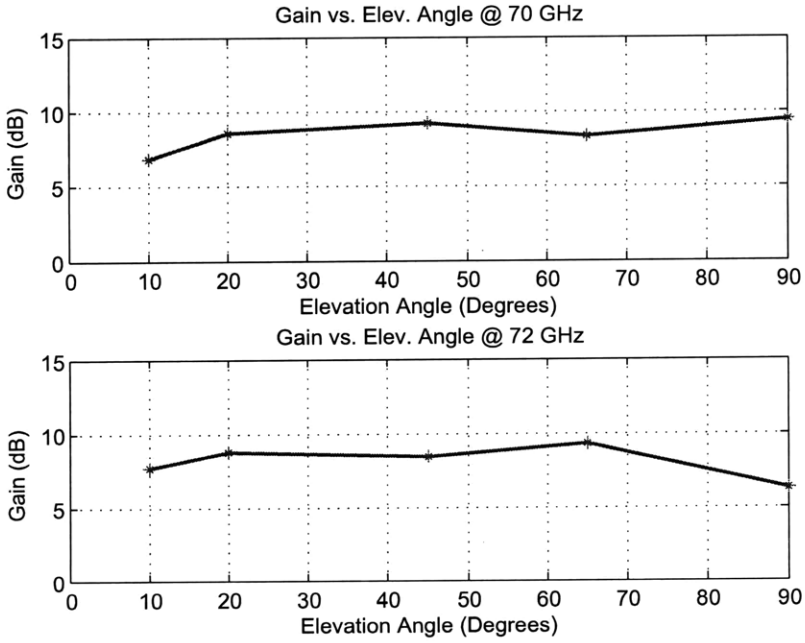

Figure B-1: *Antenna Gain vs. Angle: 70 GHz and 72 GHz, Elevation Plane.*

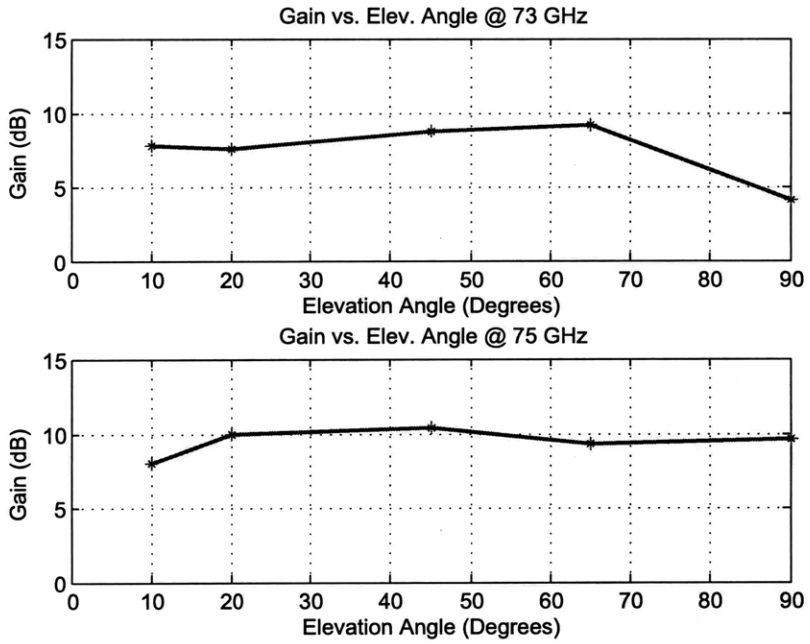

Figure B-2: *Antenna Gain vs. Angle: 73 GHz and 75 GHz, Elevation Plane.*

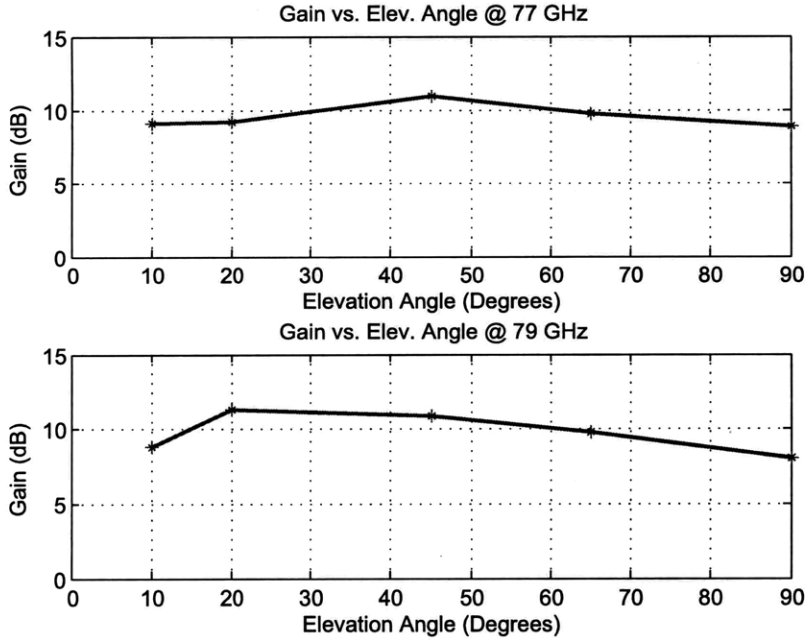

Figure B-3: *Antenna Gain vs. Angle: 77 GHz and 79 GHz, Elevation Plane.*

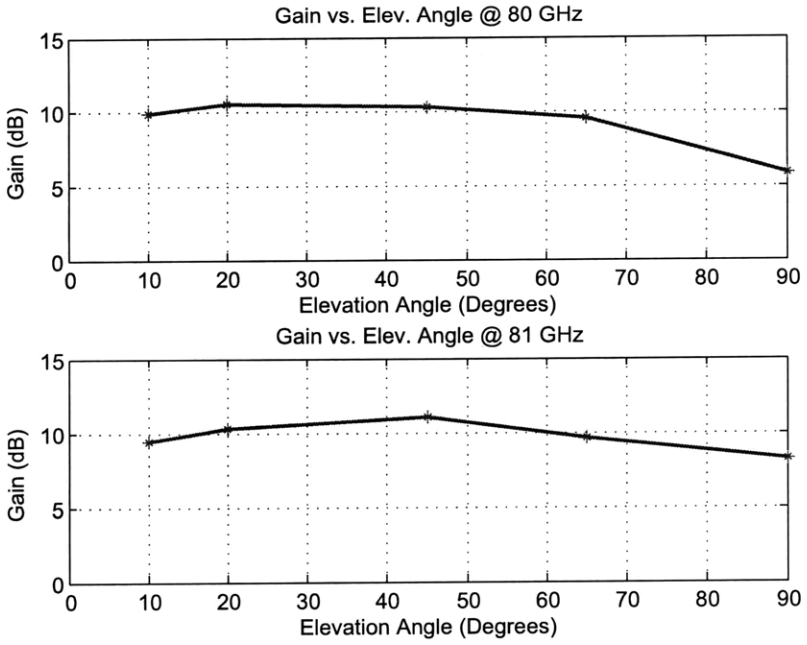

Figure B-4: *Antenna Gain vs. Angle: 80 GHz and 81 GHz, Elevation Plane.*

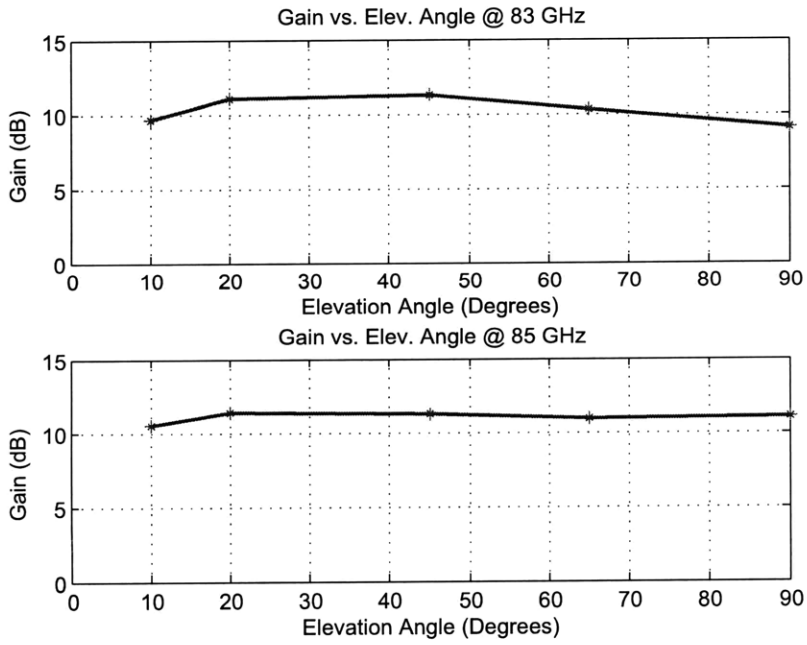

Figure B-5: *Antenna Gain vs. Angle: 83 GHz and 85 GHz, Elevation Plane.*

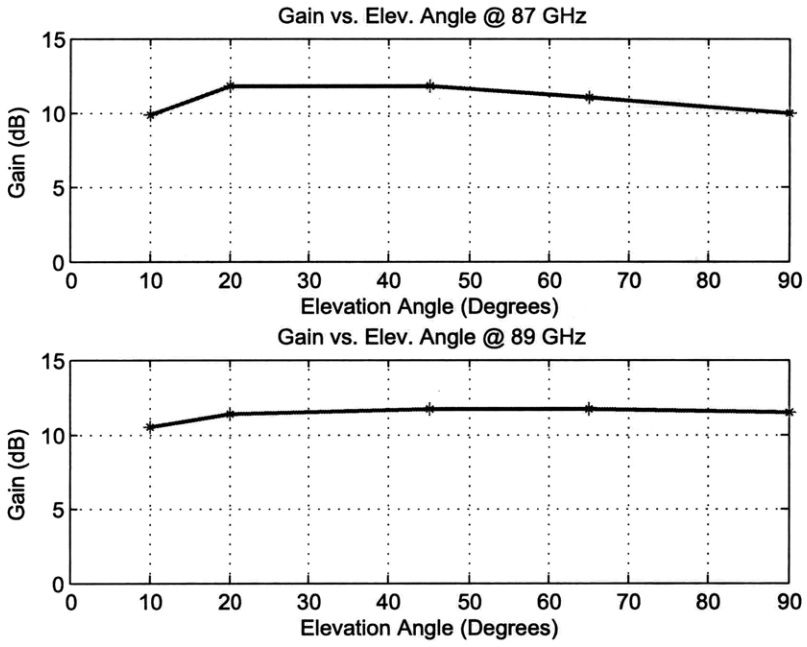

Figure B-6: *Antenna Gain vs. Angle: 87 GHz and 89 GHz, Elevation Plane.*

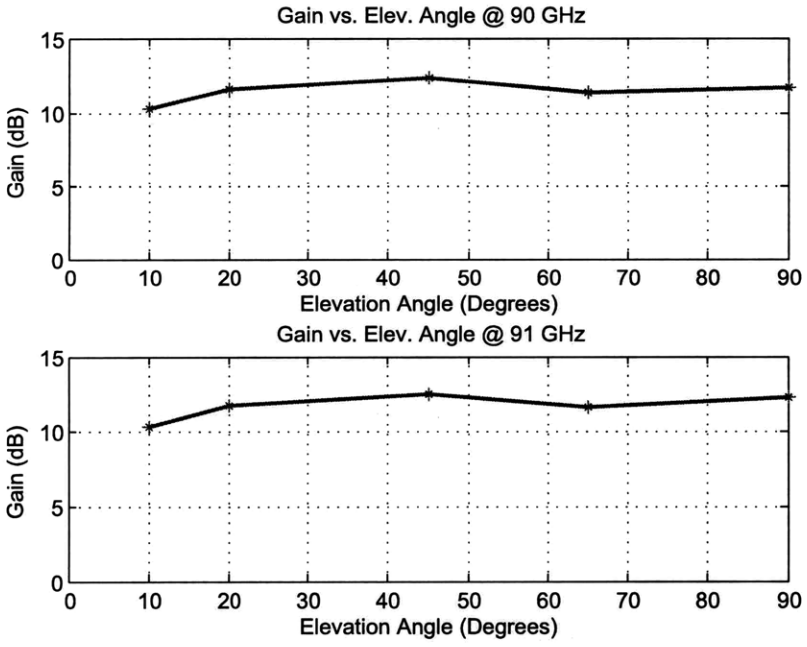

Figure B-7: *Antenna Gain vs. Angle: 90 GHz and 91 GHz, Elevation Plane.*

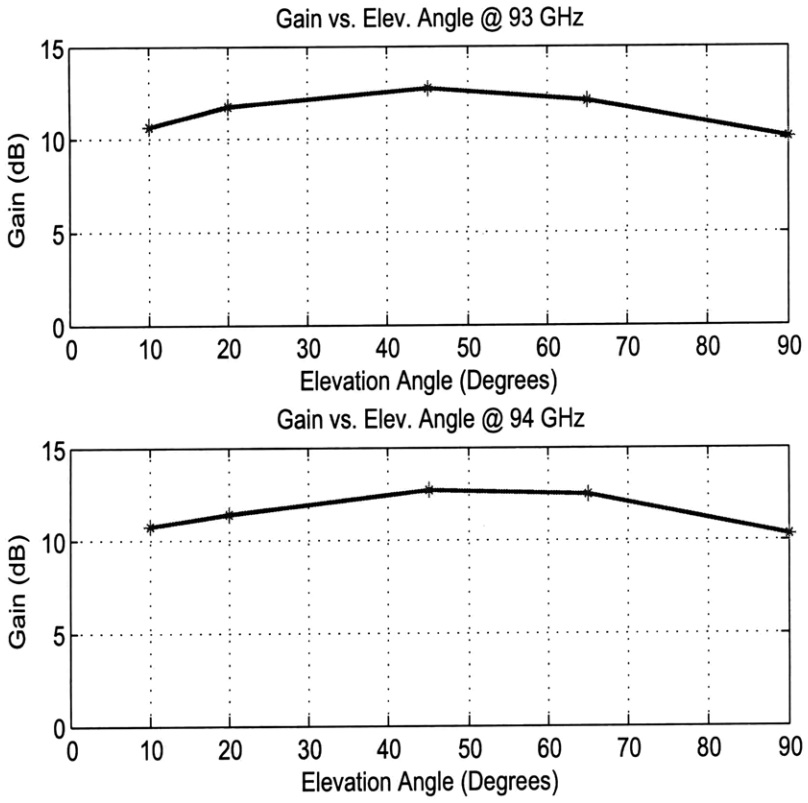

Figure B-8: *Antenna Gain vs. Angle: 93 GHz and 94 GHz, Elevation Plane.*

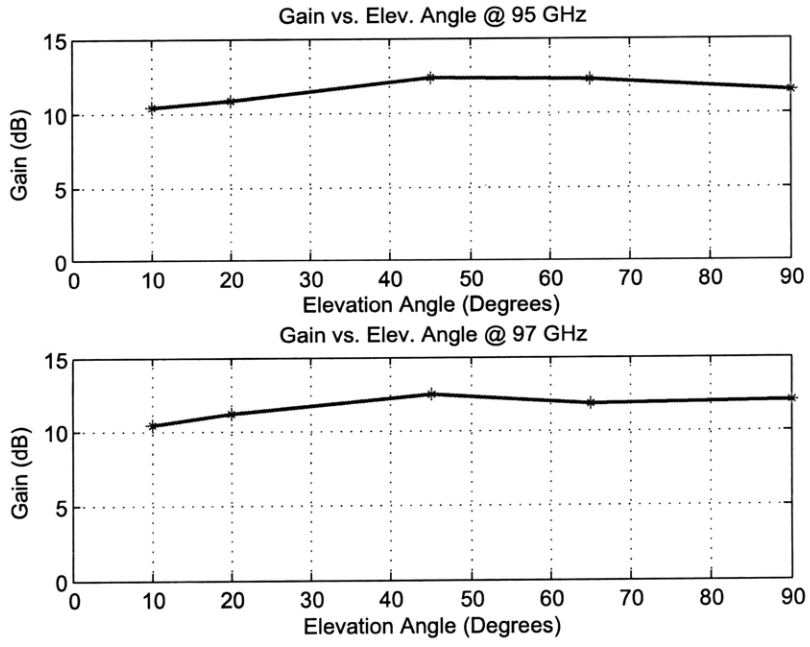

Figure B-9: *Antenna Gain vs. Angle: 95 GHz and 97 GHz, Elevation Plane.*

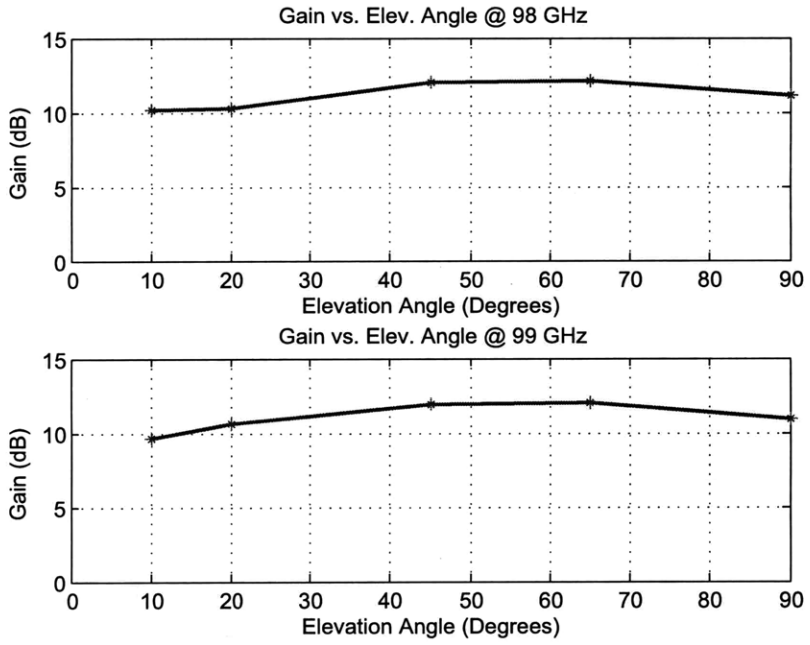

Figure B-10: *Antenna Gain vs. Angle: 98 GHz and 99 GHz, Elevation Plane.*

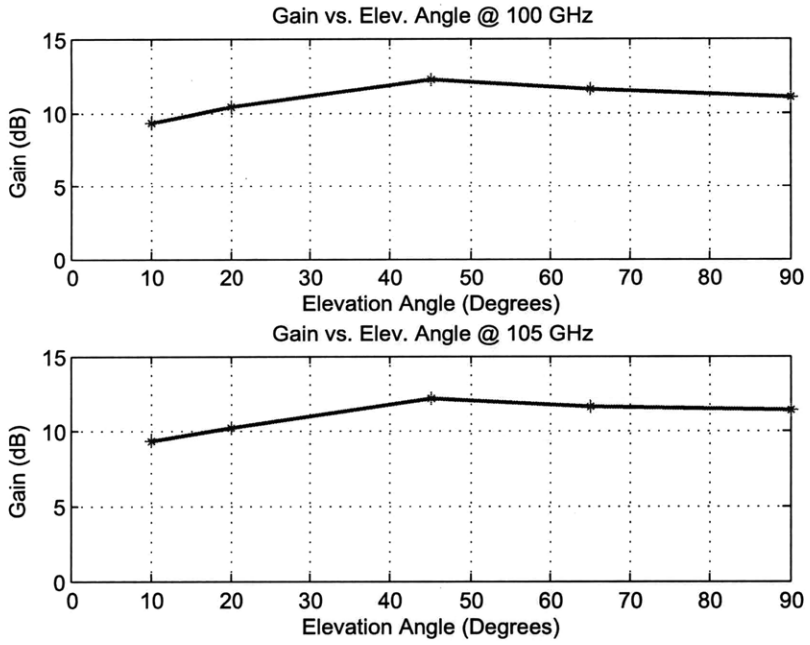

Figure B-11: *Antenna Gain vs. Angle: 100 GHz and 105 GHz, Elevation Plane.*

Appendix C

C.1 Antenna Gain vs. Frequency

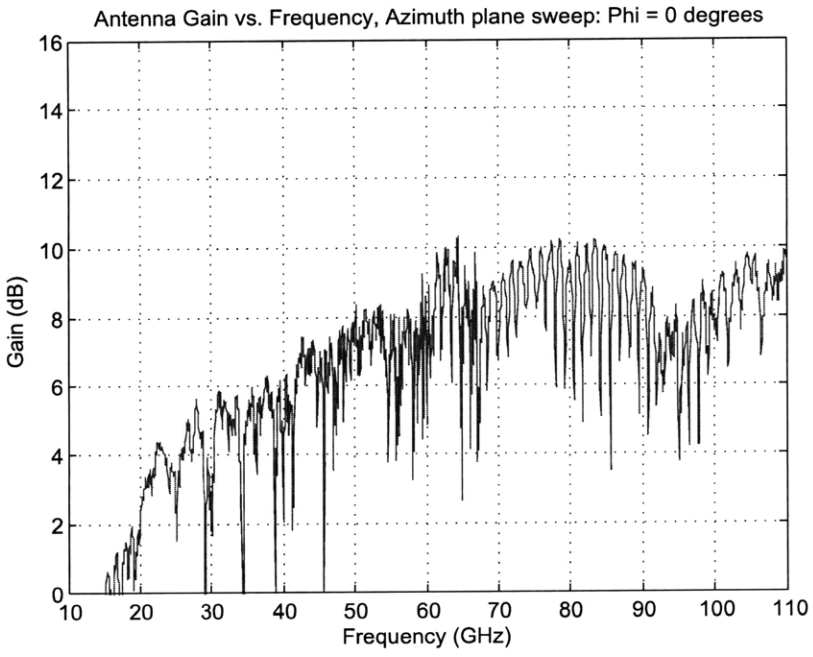

Figure C-1: *Antenna Gain vs. Frequency: Azimuth Plane.*

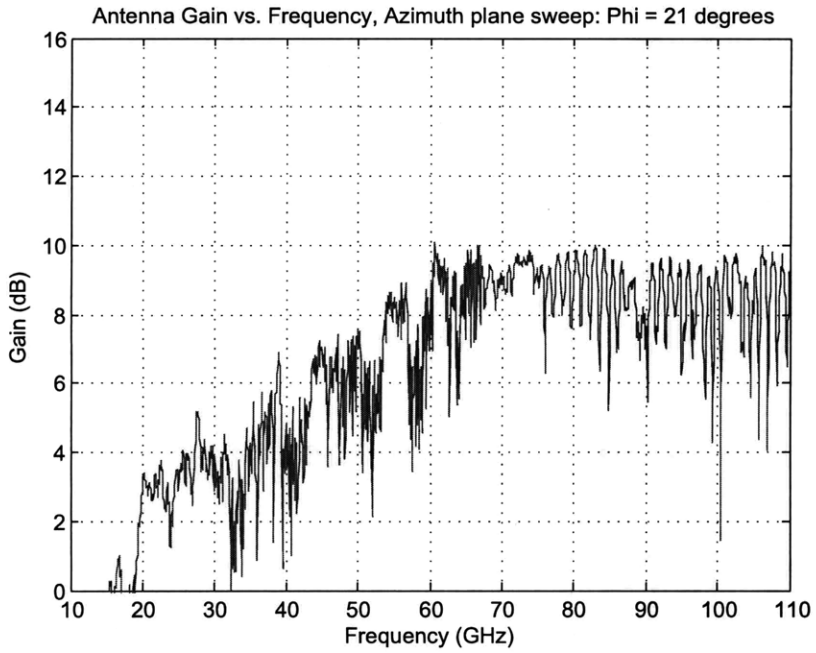

Figure C-2: *Antenna Gain vs. Frequency: Azimuth 21 Degrees.*

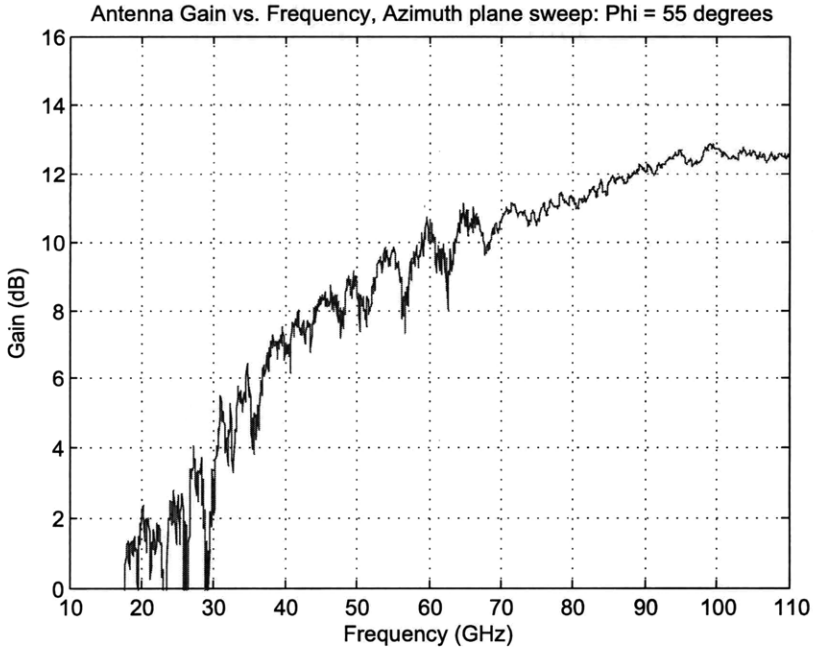

Figure C-3: *Antenna Gain vs. Frequency: Azimuth 55 degrees.*

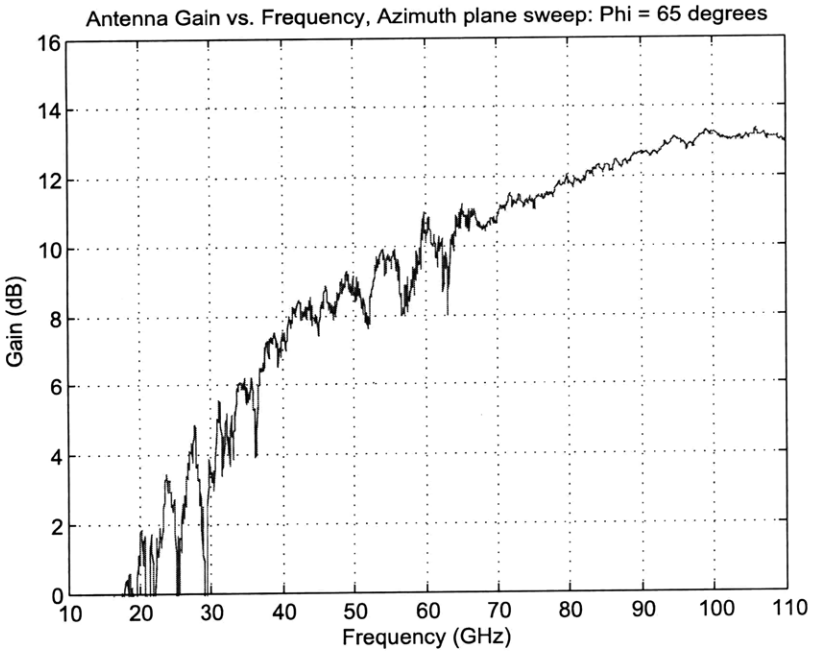

Figure C-4: *Antenna Gain vs. Frequency: Azimuth 65 degrees.*

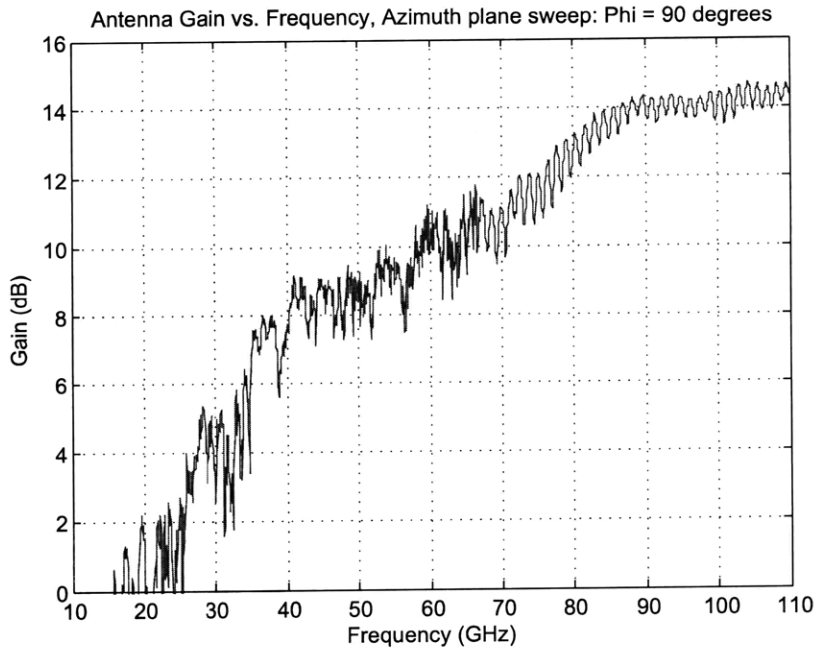

Figure C-5: *Antenna Gain vs. Frequency: Azimuth 90 degrees.*

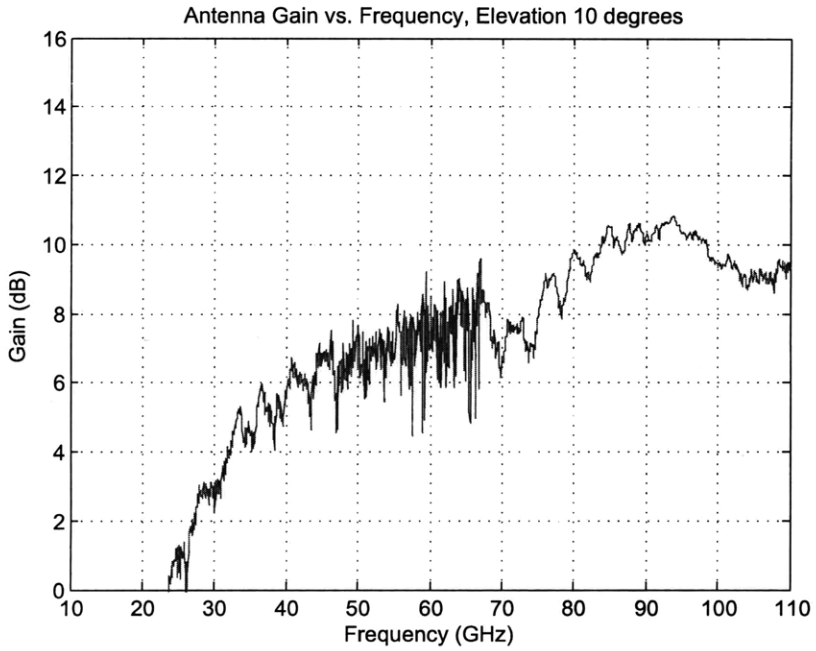

Figure C-6: *Antenna Gain vs. Frequency: Elevation Plane.*

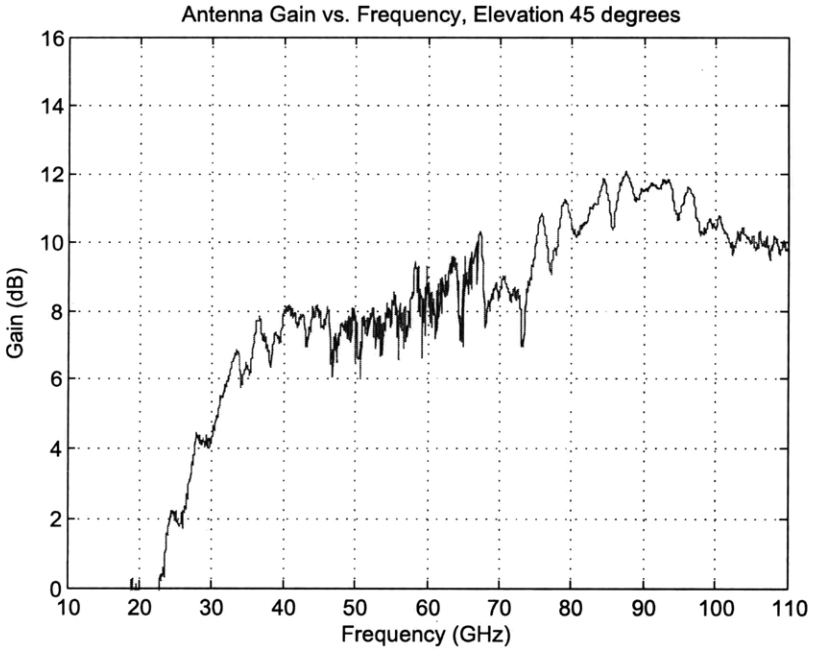

Figure C-7: *Antenna Gain vs. Frequency: Elevation 45 degrees.*

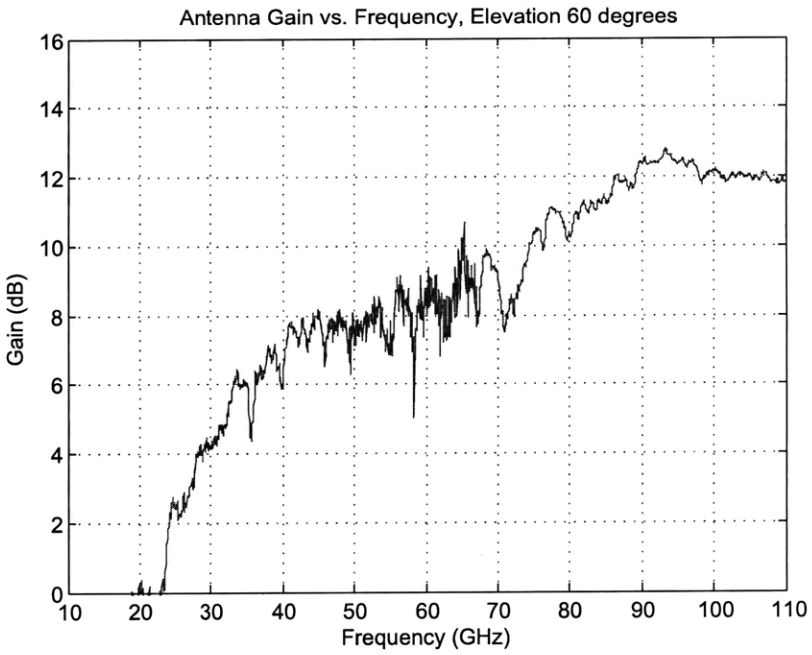

Figure C-8: *Antenna Gain vs. Frequency: Elevation 60 degrees.*

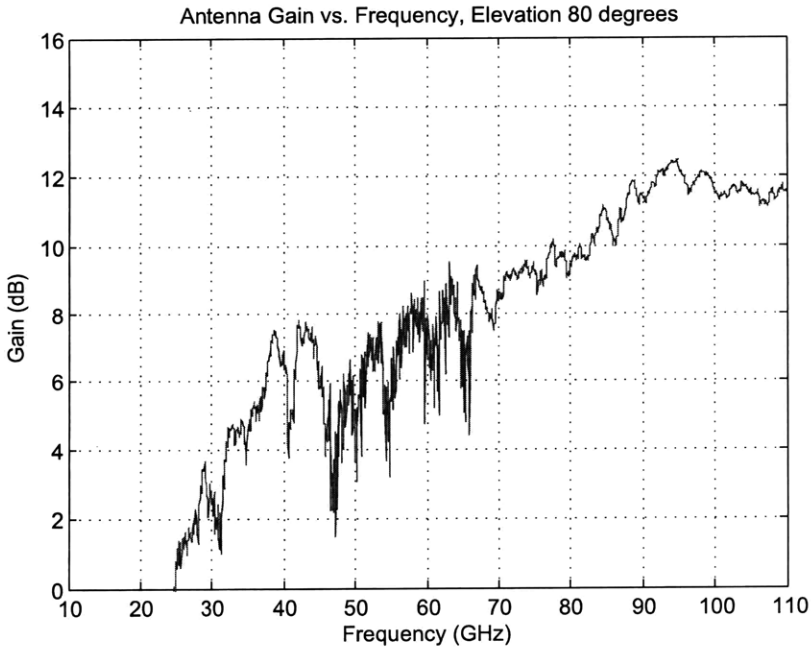

Figure C-9: *Antenna Gain vs. Frequency: Elevation 80 degrees.*

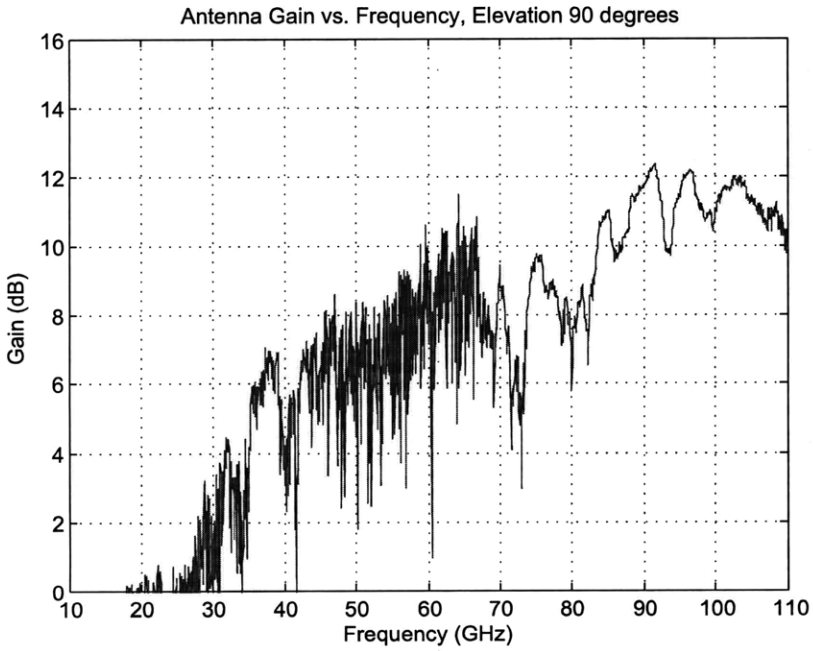

Figure C-10: *Antenna Gain vs. Frequency: Elevation 90 degrees.*

Bibliography

[1] Isaiah Blankson. Passive millimeter wave imaging with super-resolution: Application to aviation safety in extremely poor visibility, Presented at the University of Minnesota, May, 2001.

[2] Behzad Razavi. *RF Microelectronics.* Prentice Hall, 1998.

[3] P.F. Goldsmith, C.-T. Hsieh, G.R. Huguenin, J. Kapitzky, and E.L. Moore. Focal plane imaging systems for millimeter wavelengths. *Microwave Theory and Techniques, IEEE Transactions on*, 41(10):1664–1675, Oct 1993.

[4] K.W. Chang, H. Wang, S.B. Bui, T.-h. Chen, K.L. Tan, T.-N. Ton, J. Berenz, G.S. Dow, T.S. Lin, D.C. Garske, and L.C.T. Liu. A w-band monolithic downconverter. *Microwave Theory and Techniques, IEEE Transactions on*, 39(12):1972–1979, Dec 1991.

[5] T.N. Ton, B. Allen, H. Wang, G.S. Dow, E. Barnachea, and J. Berenz. A w-band, high-gain, low-noise amplifier using phemt mmic. *Microwave and Guided Wave Letters, IEEE*, 2(2):63–64, Feb 1992.

[6] H. Wang, R. Lai, T.H. Chen, P.D. Chow, J. Velebir, K.L. Tan, D.C. Streit, P.H. Liu, and G. Ponchak. A monolithic w-band three-stage lna using 0.1 mu m inalas/ingaas/inp hemt technology. *Microwave Symposium Digest, 1993., IEEE MTT-S International*, pages 519–522 vol.2, 1993.

[7] J.-S. Rieh, B. Jagannathan, H. Chen, K.T. Schonenberg, D. Angell, A. Chinthakindi, J. Florkey, F. Golan, D. Greenberg, S.-J. Jeng, M. Khater,

F. Pagette, C. Schnabel, P. Smith, A. Stricker, K. Vaed, R. Volant, D. Ahlgren, G. Freeman, K. Stein, and S. Subbanna. Sige hbts with cut-off frequency of 350 ghz. *Electron Devices Meeting, 2002. IEDM '02. Digest. International*, pages 771–774, 2002.

[8] A. Natarajan, A. Komijani, X. Guan, A. Babakhani, and A. Hajimiri. A 77-ghz phased-array transceiver with on-chip antennas in silicon: Transmitter and local lo-path phase shifting. *Solid-State Circuits, IEEE Journal of*, 41(12):2807–2819, Dec. 2006.

[9] S.T. Nicolson, P. Chevalier, A. Chantre, B. Sautreuil, and S.P. Voinigescu. A 77-79-ghz doppler radar transceiver in silicon. *Compound Semiconductor Integrated Circuit Symposium, 2007. CSIC 2007. IEEE*, pages 1–4, Oct. 2007.

[10] Juo-Jung Hung, T.M. Hancock, and G.M. Rebeiz. A 77 ghz sige sub-harmonic balanced mixer. *Solid-State Circuits, IEEE Journal of*, 40(11):2167–2173, Nov. 2005.

[11] H. Kim, S. Duffy, J. Herd, and C. Sodini. Sige ic- based mm-wave imager. *Circuits and Systems, 2007. ISCAS 2007. IEEE International Symposium on*, pages 1975–1978, May 2007.

[12] Kihong Kim, Hyun Yoon, and K.K. O. On-chip wireless interconnection with integrated antennas. *Electron Devices Meeting, 2000. IEDM Technical Digest. International*, pages 485–488, 2000.

[13] K. Kim and K.K. O. Characteristics of integrated dipole antennas on bulk, soi, and sos substrates for wireless communication. *Interconnect Technology Conference, 1998. Proceedings of the IEEE 1998 International*, pages 21–23, Jun 1998.

[14] A.B.M.H. Rashid, S. Watanabe, and T. Kikkawa. High transmission gain integrated antenna on extremely high resistivity si for ulsi wireless interconnect. *Electron Device Letters, IEEE*, 23(12):731–733, Dec 2002.

[15] R. Li, W. Bomstad, J. Caserta, X. Guo, and O. Kenneth. Evaluation of integrated antennas for wireless connection between an integrated circuit and an off-chip antenna. *Interconnect Technology Conference, 2003. Proceedings of the IEEE 2003 International*, pages 120–122, June 2003.

[16] K.T. Chan, A. Chin, Y.B. Chen, Y.-D. Lin, T.S. Duh, and W.J. Lin. Integrated antennas on si, proton-implanted si and si-on-quartz. *Electron Devices Meeting, 2001. IEDM Technical Digest. International*, pages 40.6.1–40.6.4, 2001.

[17] K.T. Chan, A. Chin, Y.D. Lin, C.Y. Chang, C.X. Zhu, M.F. Li, D.L. Kwong, S. McAlister, D.S. Duh, and W.J. Lin. Integrated antennas on si with over 100 ghz performance, fabricated using an optimized proton implantation process. *Microwave and Wireless Components Letters, IEEE*, 13(11):487–489, Nov. 2003.

[18] M. Singer, K.M. Strohm, J.-F. Luy, and E.M. Biebl. Active simmwic-antenna for automotive applications. *Microwave Symposium Digest, 1997., IEEE MTT-S International*, 3:1265–1268 vol.3, Jun 1997.

[19] P.M. Mendes, S. Sinaga, A. Polyakov, M. Bartek, J.N. Burghartz, and J.H. Correia. Wafer-level integration of on-chip antennas and rf passives using high-resistivity polysilicon substrate technology. *Electronic Components and Technology Conference, 2004. Proceedings. 54th*, 2:1879–1884 Vol.2, June 2004.

[20] Jau-Jr Lin, Xiaoling Guo, Ran Li, J. Branch, J.E. Brewer, and K.K. O. 10 improvement of power transmission over free space using integrated antennas on silicon substrates. *Custom Integrated Circuits Conference, 2004. Proceedings of the IEEE 2004*, pages 697–700, Oct. 2004.

[21] Y.P. Zhang, M. Sun, and L.H. Guo. On-chip antennas for 60-ghz radios in silicon technology. *Electron Devices, IEEE Transactions on*, 52(7):1664–1668, July 2005.

[22] L.H. Guo, A.P. Popov, H.Y. Li, Y.H. Wang, V. Bliznetsov, G.Q. Lo, N. Balasubramanian, and D.-L. Kwong. A small oca on a 10.5-mm2 2.45-ghz rfid tag-design

and integration based on a cmos-compatible manufacturing technology. *Electron Device Letters, IEEE*, 27(2):96–98, Feb. 2006.

[23] A. Shamim, L. Roy, N. Fong, and N.G. Tarr. 24 ghz on-chip antennas and balun on bulk si for air transmission. *Antennas and Propagation, IEEE Transactions on*, 56(2):303–311, Feb. 2008.

[24] M. Sasaki. Design of a millimeter-wave cmos radiation oscillator with an above-chip patch antenna. *Circuits and Systems II: Express Briefs, IEEE Transactions on*, 53(10):1128–1132, October 2006.

[25] U.R. Pfeiffer and A. Valdes-Garcia. Millimeter-wave design considerations for power amplifiers in an sige process technology. *Microwave Theory and Techniques, IEEE Transactions on*, 54(1):57–64, Jan. 2006.

[26] F. Pascal, C. Chay, M.J. Deen, S.G. Jarrix, C. Delseny, and A. Penarier. Comparison of low freq noise in iii-v and si/sige hbts. *Circuits Devices Syst. IEE Proceedings*, 151(2), April 2004.

[27] A.K. Kirtania, M.B. Das, S. Chandrasekhar, L.M. Lunardi, G.J. Qua, R.A. Hamm, and Li-Wu Yang. Measurement and comparison of 1/f noise and g-r noise in silicon homojunction and iii-v heterojunction bipolar transistors. *Electron Devices, IEEE Transactions on*, 43(5):784–792, May 1996.

[28] R.G. Meyer. Low-power monolithic rf peak detector analysis. *Solid-State Circuits, IEEE Journal of*, 30(1):65–67, Jan 1995.

[29] T. H. Lee. *The Design of CMOS Radio-Frequency Integrated Circuits.* Cambridge University Press, 1998.

[30] B. Dehlink, M. Engl, K. Aufinger, and H. Knapp. Integrated bandpass filter at 77 ghz in sige technology. *Microwave and Wireless Components Letters, IEEE*, 17(5):346–348, May 2007.

[31] Lan Nan, K. Mouthaan, Yong-Zhong Xiong, Jinglin Shi, S.C. Rustagi, and Ban-Leong Ooi. Design of 60- and 77-ghz narrow-bandpass filters in cmos technology. *Circuits and Systems II: Express Briefs, IEEE Transactions on*, 55(8):738–742, Aug. 2008.

[32] J.A. Kong. *Electromagnetic Wave Theory.* E M W, 2000.

[33] Morgenthaler Staelin and Kong. *Electromagnetic Waves.* Pearson Education, 1998.

[34] D.M. Pozar. *Microwave and RF Design of Wireless Systems.* Wiley, New York, USA, 2001.

[35] IEEE Transactions on Antennas and Propagation. Vol. ap-17, no. 3., 1969.

[36] C. A. Balanis. *Antenna Theory and Analysis.* Wiley, New York, USA, 1997.

[37] W. Stutzman. *Antenna Theory and Design.* Wiley, New York, USA, 1998.

[38] A. Hajimiri. mm-wave silicon ics: Challenges and opportunities. *Custom Integrated Circuits Conference, 2007. CICC '07. IEEE*, pages 741–747, Sept. 2007.

[39] K. Carver and J. Mink. Microstrip antenna technology. *Antennas and Propagation, IEEE Transactions on*, 29(1):2–24, Jan 1981.

[40] E. Belohoubek and E. Denlinger. Loss considerations for microstrip resonators. *Microwave Theory and Technology, IEEE Transactions on*, MTT-23:522–526, June 1975.

[41] L. Lewin. Radiation from discontinuities in stripline. volume 107 of *Presented at IEEE Antennas and Propagation Conference*, pages 163–170, Feb 1960.

[42] J. Powell and A. Chandrakasan. Differential and single ended elliptical antennas for 3.1-10.6 ghz ultra wideband communication. *Antennas and Propagation Society International Symposium, 2004. IEEE*, 3:2935–2938 Vol.3, June 2004.

[43] P.J. Gibson. The vivaldi aerial. *European Microwave Conference, 1979. 9th*, pages 101–105, Oct. 1979.

[44] H.H Beverage. The wave antenna. *Transactions AIEE*, 42:215, 1923.

[45] Rogers. 4000 series data sheet. `http://www.integratedtest.com/products/pcb-fabrication/laminates/Rogers4003-4350.pdf`.

[46] Donhee Ham. Harvard es272 lecture notes, Fall 2007.

[47] S.P. Voinigescu, M.C. Maliepaard, J.L. Showell, G.E. Babcock, D. Marchesan, M. Schroter, P. Schvan, and D.L. Harame. A scalable high-frequency noise model for bipolar transistors with application to optimal transistor sizing for low-noise amplifier design. *Solid-State Circuits, IEEE Journal of*, 32(9):1430–1439, Sep 1997.

[48] P. Hillbrand, H. Russer. An efficient method for computer aided noise analysis of linear amplifier networks. *Circuits and Systems, IEEE Transactions on*, pages 235–238, April 1976.

[49] Khoa Nguyen. Digital phase tightening for millimeter-wave imaging, August 2008.

[50] D.B. Leeson. A simple model of feedback oscillator noise spectrum. *Proceedings of the IEEE*, 54(2):329–330, Feb. 1966.

[51] C. John Grebenkemper. Local oscillator phase noise and its effect on receiver performance, 1981.

[52] Rob Howald. Making more noise, 2005.

[53] Bernhard Dehlink, Hans-Dieter Wohlmuth, Klaus Aufinger, Franz Weiss, and Arpad L. Scholtz. An 80 ghz sige quadrature receiver frontend. *Compound Semiconductor Integrated Circuit Symposium, 2006. CSIC 2006. IEEE*, pages 197–200, Nov. 2006.

[54] S.T. Nicolson, K.A. Tang, K.H.K. Yau, P. Chevalier, B. Sautreuil, and S.P. Voinigescu. A low-voltage 77-ghz automotive radar chipset. *Microwave Symposium, 2007. IEEE/MTT-S International*, pages 487–490, June 2007.

[55] M. Hartmann, C. Wagner, K. Seemann, J. Platz, H. Jager, and R. Weigel. A low-power low-noise single-chip receiver front-end for automotive radar at 77 ghz in silicon-germanium bipolar technology. *Radio Frequency Integrated Circuits (RFIC) Symposium, 2007 IEEE*, pages 149–152, June 2007.

[56] S.T. Nicolson, K.H.K. Yau, P. Chevalier, A. Chantre, B. Sautreuil, K.W. Tang, and S.P. Voinigescu. Design and scaling of w-band sige bicmos vcos. *Solid-State Circuits, IEEE Journal of*, 42(9):1821–1833, Sept. 2007.

[57] K.W. Tang, M. Khanpour, P. Garcia, C. Gamier, and S.P. Voinigescu. 65-nm cmos, w-band receivers for imaging applications. *Custom Integrated Circuits Conference, 2007. CICC '07. IEEE*, pages 749–752, Sept. 2007.

[58] A. Natarajan, A. Komijani, X. Guan, A. Babakhani, and A. Hajimiri. A 77-ghz phased-array transceiver with on-chip antennas in silicon: Transmitter and local lo-path phase shifting. *Solid-State Circuits, IEEE Journal of*, 41(12):2807–2819, Dec. 2006.

[59] E. Laskin, P. Chevalier, A. Chantre, B. Sautreuil, and S.P. Voinigescu. 80/160-ghz transceiver and 140-ghz amplifier in sige technology. *Radio Frequency Integrated Circuits (RFIC) Symposium, 2007 IEEE*, pages 153–156, June 2007.

[60] S.K. Reynolds, B.A. Floyd, U.R. Pfeiffer, T.J. Beukema, T. Zwick, J. Grzyb, D. Liu, and B.P. Gaucher. Progress toward a low-cost millimeter-wave silicon radio. *Custom Integrated Circuits Conference, 2005. Proceedings of the IEEE 2005*, pages 563–570, Sept. 2005.

[61] B.A. Floyd. V-band and w-band sige bipolar low-noise amplifiers and voltage-controlled oscillators. *Radio Frequency Integrated Circuits (RFIC) Symposium, 2004. Digest of Papers. 2004 IEEE*, pages 295–298, June 2004.

[62] Li Wang, S. Glisic, J. Borngraeber, W. Winkler, and J.C. Scheytt. A single-ended fully integrated sige 77/79 ghz receiver for automotive radar. *Solid-State Circuits, IEEE Journal of*, 43(9):1897–1908, Sept. 2008.

[63] R.G. Meyer. Circuit performance characterization of digital 45-nm cmos technology for applications around 110 ghz. *VLSI Circuits, 2008 IEEE Symposium on*, pages 162–163, June 2008.

[64] C.H. Doan, S. Emami, A.M. Niknejad, and R.W. Brodersen. Millimeter-wave cmos design. *Solid-State Circuits, IEEE Journal of*, 40(1):144–155, Jan. 2005.

[65] S.T. Nicolson, A. Tomkins, K.W. Tang, A. Cathelin, D. Belot, and S.P. Voinigescu. A 1.2v, 140ghz receiver with on-die antenna in 65nm cmos. *Radio Frequency Integrated Circuits Symposium, 2008. RFIC 2008. IEEE*, pages 229–232, 17 2008-April 17 2008.

[66] A. Babakhani, X. Guan, A. Komijani, A. Natarajan, and A. Hajimiri. A 77-ghz phased-array transceiver with on-chip antennas in silicon: Receiver and antennas. *Solid-State Circuits, IEEE Journal of*, 41(12):2795–2806, Dec. 2006.

[67] W. Mayer, M. Meilchen, W. Grabherr, P. Nuchter, and R. Guhl. Eight-channel 77-ghz front-end module with high-performance synthesized signal generator for fm-cw sensor applications. *Microwave Theory and Techniques, IEEE Transactions on*, 52(3):993–1000, March 2004.

[68] B.A. Floyd, S.K. Reynolds, U.R. Pfeiffer, T. Zwick, T. Beukema, and B. Gaucher. Sige bipolar transceiver circuits operating at 60 ghz. *Solid-State Circuits, IEEE Journal of*, 40(1):156–167, Jan. 2005.

[69] Byung-Wook Min and G.M. Rebeiz. A low-loss silicon-on-silicon dc-110-ghz resonance-free package. *Microwave Theory and Techniques, IEEE Transactions on*, 54(2):710–716, Feb. 2006.

[70] P. Russer. Si and sige millimeter-wave integrated circuits. *Microwave Theory and Techniques, IEEE Transactions on*, 46(5):590–603, May 1998.

[71] P. Russer. Si and sige millimeterwave integrated circuits for sensor and communications applications. *Microwaves and Radar, 1998. MIKON '98., 12th International Conference on*, 4:330–344 vol.4, May 1998.

[72] Hao Li and H.-M. Rein. Millimeter-wave vcos with wide tuning range and low phase noise, fully integrated in a sige bipolar production technology. *Solid-State Circuits, IEEE Journal of*, 38(2):184–191, Feb 2003.

[73] G.S. Dow, D.C.W. Lo, Y. Guo, E.W. Lin, T.T. Chung, M.D. Biedenbender, O. Miromontes, A. Marashi, L. Yujiri, P.S.C. Lee, M.M. Shoucri, and B.R. Allen. Large scale w-band focal plane array for passive radiometric imaging. *Microwave Symposium Digest, 1996., IEEE MTT-S International*, 1:369–372 vol.1, Jun 1996.

[74] H. Wang, G.S. Dow, B.R. Allen, T.-N. Ton, K.L. Tan, K.W. Chang, T.-h. Chen, J. Berenz, T.S. Lin, P.-H. Liu, D.C. Streit, S.B. Bui, J.J. Raggio, and P.D. Chow. High-performance in w-band monolithic pseudomorphic ingaas hemt lna's and design/analysis methodology. *Microwave Theory and Techniques, IEEE Transactions on*, 40(3):417–428, Mar 1992.

[75] A. K. Fung F. T. Ulaby, R. K. Moore. *Microwave Remote Sensing, Active and Passive.* Addison-Wesley Publishing, 1981.

[76] R. Appleby. Passive millimeter wave imaging and security. *First European Radar Conference*, pages 275–278, 2004.

[77] P. Gray, P. Hurst, S. Lewis, and R. Meyer. *Analysis and design of analog integrated circuits, Fourth Ed.* John Wiley and Sons, 2001.

[78] G. Gonzalez. *Microwave Transistor Amplifiers Analysis and Design.* Prentice-Hall, 1984.

[79] S.T. Nicholson and S.P. Voinigescu. Methodology for simultaneous noise and impedance matching in w-band lnas. *Compound Semiconductor Integrated Circuit Symposium, 2006 IEEE*, pages 279–282, November 2006.

[80] U.R. Pfeiffer, J. Grzyb, Duixian Liu, B. Gaucher, T. Beukema, B.A. Floyd, and S.K. Reynolds. A chip-scale packaging technology for 60-ghz wireless chipsets. *Microwave Theory and Techniques, IEEE Transactions on*, 54(8):3387–3397, Aug. 2006.

[81] J. Powell, H. Kim, and C. G. Sodini. Sige receiver front ends for millimeter-wave passive imaging. *Microwave Theory and Techniques, IEEE Transactions on*, 56(11):2416–2425, Nov. 2008.

[82] J. Powell, H. Kim, and C.G. Sodini. A 77-ghz receiver front end for passive imaging. *Radio Frequency Integrated Circuits (RFIC) Symposium, 2007 IEEE*, pages 145–148, June 2007.

[83] W.Y. Ali-Ahmad and G.M. Rebeiz. 92 ghz dual-polarized integrated horn antennas. *Antennas and Propagation, IEEE Transactions on*, 39(6):820–825, Jun 1991.

[84] G.P. Gauthier, J.-P. Raskin, L.P.B. Katehi, and G.M. Rebeiz. A 94-ghz aperture-coupled micromachined microstrip antenna. *Antennas and Propagation, IEEE Transactions on*, 47(12):1761–1766, December 1999.

[85] S. Montusclat, F. Gianesello, D. Gloria, and S. Tedjini. Silicon integrated antenna developments up to 80 ghz for millimeter wave wireless links. *Wireless Technology, 2005. The European Conference on*, pages 237–240, Oct. 2005.

[86] B. Van der Pol and J. Van der Mark. Frequency demultiplication. *Nature*, (120):363–364, 1927.